FIELD THEORY ANALYSIS OF RECTANGULAR AND CIRCULAR WAVEGUIDE DISCONTINUITIES FOR FILTERS, MULTIPLEXERS AND MATCHING NETWORKS

by

Benoît Varailhon de la Filolie

Maître es science, 1984 (Université de Bordeaux, France)
Diplomé Ingénieur INSA, 1987 (INSA Rennes, France)

A DISSERTATION SUBMITTED IN PARTIAL FULFILLMENT
OF THE REQUIREMENTS FOR THE DEGREE OF
DOCTOR OF PHILOSOPHY
in the Department of
Electrical and Computer Engineering

ACCEPTED
ACULTY OF GRADUATE STUDIES

DEAN

ATE 12 AUG 92

We accept this dissertation as conforming
to the required standard

Dr. R. Vahldieck, Supervisor & Graduate Advisor, Dept. of Elect. & Comp. Eng.

Dr. J. Bornemann, Department Member, Dept. of Elect. & Comp. Eng.

Dr. P. F. Friessen, Department Member, Dept. of Elect. & Comp. Eng.

Dr. R. N. Horspool, Outside Member, Dept. of Computer Science

Dr. B. Tabarrok, Outside Member, Dept. of Mechanical Engineering

Dr. V. K. Tripathi, External Examiner, Oregon State University

UNIVERSITY OF VICTORIA

Supervisor: Dr. R. Vahldieck

ABSTRACT

Progress in integrating microwave circuits depends largely on the development of computationally effective and accurate numerical methods. These methods allow a miniaturization of microwave components and their utilization at higher frequency.

In this thesis, the application of the mode matching method is described as well as their modification to different kinds of structure in rectangular and circular waveguides. The task is to design and optimize filters, multiplexers and impedance matching networks. In its most general form, the mode matching method at waveguide discontinuities requires the matching of four field components. However, to improve computational efficiency, the effect of matching only two field components (versus four field components) is investigated and successfully exploited for selected discontinuities.

To satisfy space requirements, low loss, compact, and lightweight diplexer, triplexer and quadriplexer structures in rectangular waveguide technology are designed and optimized. The analysis is made possible by decomposing the structure into simple discontinuity sections such as discontinuity in width, height or bi- and tri-furcations.

Three different types of discontinuities in coaxial waveguide are investigated: the outer step, the inner step and the gap discontinuities. By cascading such discontinuities, filters or matching networks can be obtained.

Finally, a new type of circular waveguide bandpass filter using printed metal inserts is developed and designed in Ka-band. A comparison between theoretical results and measurements shows excellent agreement.

Examiners:

Dr. R. Vahldieck, Supervisor & Graduate Advisor, Dept. of Elect. & Comp. Eng.

Dr. J. Bornemann, Department Member, Dept. of Elect. & Comp. Eng.

Dr. P. F. Friessen, Department Member, Dept. of Elect. & Comp. Eng.

Dr. R. N. Horspool, Outside Member, Dept. of Computer Science

Dr. B. Tabarrok, Outside Member, Dept. of Mechanical Engineering

Dr. V. K. Tripathi, External Examiner, Oregon State University

Table of Contents

List of Tables

List of Figures

Acknowledgement

I wish to record my gratitude to my supervisor, Dr. R. Vahldieck of the Department of Electrical and Computer Engineering, for his perpetual encouragement, guidance, and advice during the course of this research. His undivided motivation, endeavor, and ability to create a congenial and informal atmosphere for discussion have been the major driving factors in the success of this project.

I thank Dr. J. Bornemann for his valuable comments and for aiding me with text books and technical papers during the progress of this research.

I would like to thank Dr. P. Driessen for his kind assistance and enthusiasm.

Financial assistance received from Dr. R. Vahldieck (through NSERC) is gratefully acknowledged.

A special thank, of course, to the members of the LLiMic group, in particular Dr. K. Wu, for their quotidian charm, and for their endless discussions that made this thesis better.

And finally, a word of gratitude to all my friends, in particular Isabelle, Florence and Emmanuel for their moral support, motivation, and encouragement without which my studies at UVic would not have crystallized.

Un spécial remerciement pour mes parents, pour leur patience infinie, et qui, malgré la distance, m'ont toujours supporté et encouragé. En définitive, cette thèse leur est dédiée.

A mes parents

Ad Majorem Dei Gloriam

Chapter 1

Introduction

Wireless communication is taking place at ever-increasing frequencies. The demand for large bandwidth has led to commercial utilization of millimeter-wave frequencies up to 60 GHz. The term *millimeter wave* generally refers to the frequency range where the wavelength is less than a centimeter, starting at ~ 30 GHz.

Beside the very large bandwidth that can be accommodated at millimeter-wave frequencies, there are other advantages such as:

1. The smaller wavelength allows the reduction in component size, resulting in compact systems with narrow beam-width antennas, which in turn provide greater resolution and precision in target tracking and discrimination.
2. High immunity to jamming and interference.
3. Atmospheric attenuation which is relatively low in the transmission windows (35, 94, 140 and 220 GHz) compared to I.R. and optical frequencies.

As the same time some of the advantages can also be viewed as disadvantages. For example, the smaller component size requires greater precision in manufacturing which makes millimeter-wave components more expensive. Smaller wavelengths introduce high losses for long distance atmospheric attenuation which can reach 0.06 dB/km at 10 GHz, 0.15 dB/km at 35 GHz and 0.82 dB/km at 94 GHz (see [6]).

In microwave and millimeter wave communication systems, devices like filters or multiplexers are important for channel selection and signal separation. In particular for satellite systems, rigorous space requirements (temperature, pressure, radiation, ...) require very low loss, compact and lightweight components.

Besides planar transmission lines, waveguide components are still in use, in particular for high power systems, and will still be in use for many years to come. In a waveguide, the electric and magnetic fields are confined to the space within the guide. Thus, no power is lost through radiation. Therefore, closed waveguides are frequently used as transmission lines; in particular when specialized applications require a large range of temperature stability, de-pressurized environment, high power and low losses. Under these system requirements, it becomes crucial for the overall system performance to design and build integrated waveguide components. These components not only utilize the waveguide as a guiding and non-radiating transmission line, but also as a metallic enclosure surrounding a planar junction or circuit that determines the performance of the device. These planar structures may contain active components to form amplifiers or mixers, or the structure may be entirely passive. In this case, cascading planar junctions forms filters, matching networks, couplers, etc.

In the context of this thesis, only passive structures and of these only filters, diplexers/multiplexers and matching networks are treated. The major part of the following work is concentrated on numerical modelling of waveguide discontinuities to form these filters and matching networks.

The typical layout for a multiplexer/de-multiplexer is shown in figure 1.1.a. It consists of a number of waveguide circulators followed by the channel filters in the individual arms. The response of each channel is simply the algebraic sum of the reflections from the preceding channels plus the loss due to the multiple circulator passes [7]-[11]. Another technique consists of using T-junction manifolds instead of circulators [12]-[14]. Since this arrangement is relatively bulky and does not allow a compact design, the structure in figure 1.1.b is proposed in chapter 2 as an alternative solution. This structure has been extended to a multiplexer configuration by increasing the number of parallel channels.

In the diplexer structure (figure 1.1.b), when the number of channels increases, the height of the last steps of the taper can become quite large allowing the propagation of a certain number of higher order modes (depending on the size). Furthermore, the power division into the different channels is not perfectly equal and the optimization of the multiplexer becomes very difficult since the waveguide channels are not isolated from each other.

A possible solution to this problem is shown in figure 1.1.c. It is an extension of the diplexer concept. Not only are the filters placed on top of each other but also side by side. Thus, a larger number of channels can be fed from one incoming waveguide by opening the waveguide in both direction (x and y). In chapter 3, this solution is utilized to design a quadriplexer.

After characterizing selected discontinuities in rectangular waveguides, this thesis focusses on coaxial transmission lines and transitions in view of designing filters and matching networks. Circular and, in particular, coaxial waveguides are pushed in fre-

a) Typical multiplexer/demultiplexer

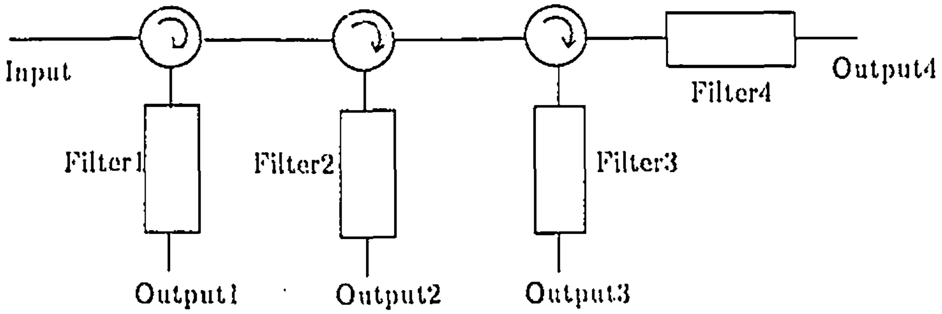

b) Proposed Diplexer

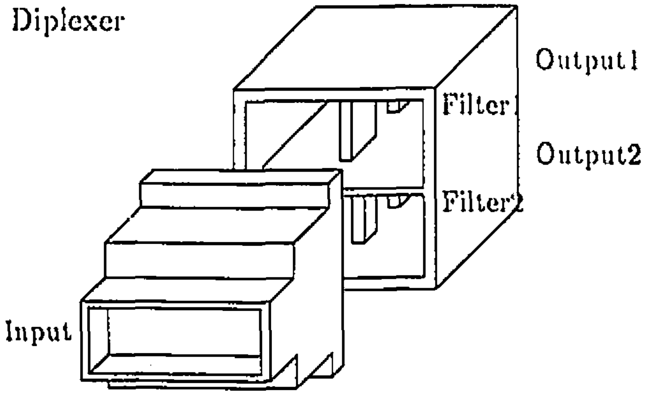

c) Proposed Quadriplexer

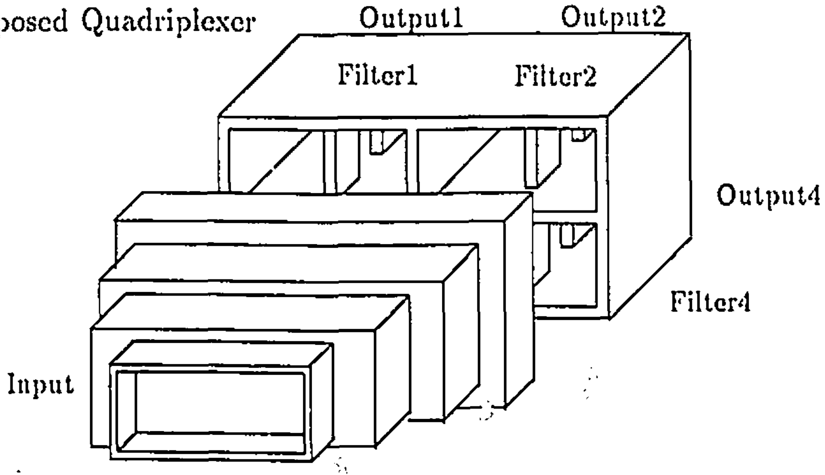

Figure 1.1: Comparison between a) a typical multiplexer/de-multiplexer, b) the proposed new structure and c) its extension to a quadriplexer.

quency to as high as 60 GHz or even 100 GHz. This leads to an extreme miniaturization of connectors, filters, adaptors, detector, etc. Optimizing their performances at these high frequencies requires sophisticated numerical techniques to take into account the effect of higher order mode excitation and inter-action between closely spaced cascaded discontinuities. In chapter 4, the analysis of selected coax transitions is presented as well as a detailed convergence analysis. Finally, filters are designed from these cascaded discontinuities and their performance analysis is given.

Only a few papers have dealt with devices in circular waveguides. In [51], cylindrical mode converters are investigated and, in [53], mode filters. In addition, papers with a more theoretical approach have been published ([54] and [55]). All of them focus on axially symmetric discontinuities. They require expensive machining techniques and are not very useful for mass fabrication. The filters to be introduced in this thesis (Fig. 5.1) are based on the metal-insert filter idea in rectangular waveguides [22]. The only differences are that the rectangular waveguide is replaced by a circular guide and that the ladder-shaped metal insert is approximated by a bow-tie shaped metal sheet instead of a rectangular sheet (Fig. 5.2). As will be shown in Chapter 5, this approximation does not introduce a noticeable error in the measured frequency response but allows a much faster field theory design of the filter. With respect to fabrication, the structure is simply assembled by embedding the ladder-shaped metal septum between the two halves of a circular split block housing (Fig. 5.1). Chapter 5 presents the analysis of such a filter and the comparison between theoretical results and measurements.

1.1 Numerical methods - an overview

Progress in integrating microwave circuits depends largely on the development of computationally effective and accurate design tools which are more and more dependent on sophisticated numerical methods. The electromagnetic fields calculated by any numerical method are derived from Maxwell's equations [2]:

$$\vec{\nabla}.\vec{D} = 0 \tag{1.1}$$

$$\vec{\nabla}.\vec{B} = 0 \tag{1.2}$$

$$\vec{\nabla} \times \vec{E} = -\frac{\partial \vec{B}}{\partial t} \tag{1.3}$$

$$\vec{\nabla} \times \vec{H} = \frac{\partial \vec{D}}{\partial t} \tag{1.4}$$

in the absence of conduction current and free charges, where $\vec{B}$ is the magnetic induction and $\vec{D}$ the electric induction. Solutions to Maxwell's equations can conveniently be derived from a vector potential $\vec{\Psi}$ which must satisfy the Helmholtz equation (in isotropic and homogeneous media):

$$\nabla^2\vec{\Psi} + k^2\vec{\Psi} = 0 \tag{1.5}$$

where $k^2 = k_0^2\epsilon_r$. The relationship between the potential and the field is given by [20]:

$$\vec{E} = \text{grad div}\vec{\Psi} + k^2\vec{\Psi} \tag{1.6}$$

$$\vec{H} = j\omega\varepsilon\vec{\nabla} \times \vec{\Psi} \tag{1.7}$$

Except for simple cases, a direct analytical solution of these equations is not possible. Numerical techniques must be used instead.

Numerical methods can be categorized into methods which discretize the electromagnetic field and those that discretize the wave equation.

For example, the Method of Line (MOL) belongs to the second category. Effectively, the MOL discretizes two of the three dimensions (in a Cartesian coordinate system) of the wave equation and then an analytical solution is sought for the remaining dimension [5].

The Finite Difference Method (FDM) belongs also to the second category since the region of interest is divided into a regular rectangular mesh and the ∇ operator is approximated at each node by evaluating the variation of the function with the neighbouring nodes.

The Finite Element Method (FEM) is similar to the FDM and consequently is also a spatial domain method. A different mesh, generally using triangles, is used. This basic element shape allows modelling of any transmission line contour. The potential is approximated by a polynomial within each triangle. The function is evaluated at each triangle vertex and compared to the neighbourhood triangle vertex values.

The Transmission Line Matrix (TLM) method is a time domain method. Here the electromagnetic field problem is converted to a three-dimensional equivalent network problem based on Huygens's principle of wave propagation [4].

The Moments Method is a good example of the first category. Effectively, the method transforms Maxwell's equations into an integral form by using retarded potential integrals, thus obtaining Green's function. Expressing the vector and scalar potentials as a sum of step functions (the basis functions) and using delta functions as testing functions allows solution of the integral equation [3].

Other methods exist such as the Transverse Resonance Method (TRM) (similar to the Mode Matching Method introduced in the next section), the Integral Equation

Method	Typical Application	Preprocessing	CPU time	Memory Storage
Frequency Domain				
SDA	Quasi-Planar Guide	Large	Short	Small
MMM	Waveguide	Moderate	Moderate	Moderate
TRM	Quasi-Planar Guide	Moderate	Moderate	Moderate
Spatial Domain				
MOL	Quasi-Planar Guide	Large	Moderate	Large
TLM	No Limitation	Small	Long	Large
FEM	No Limitation	Small	Long	Large
FDM	No Limitation	Small	Long	Large
IEM	Quasi-Planar Guide	Moderate	Moderate	Moderate

Table 1.1: Comparison of different numerical methods

Method (IEM) and its equivalent method in the frequency domain, the Spectral Domain Approach (SDA).

Table 1.1 provides a general comparison of these methods. It is interesting to note that methods requiring only a little preprocessing typically require a large amount of memory and considerable CPU time.

A universal method does not exist. However, for each type of problem, the most appropriate method may be found. Since all waveguides analyzed in this thesis have eigenfunctions expressed in classical (standard) mathematical functions, and since this thesis deals with structures involving only abrupt transitions, the Mode Matching Method has been found to be the most appropriate method, with respect to memory usage and CPU-time.

1.2 The Mode Matching Method

In the Mode Matching Method (MMM), the electromagnetic field is approximated by a sum of modal functions. The method was first introduced in 1967 by A. Wexler [9]. Later, the MMM was used by other authors for a large variety of different problems.

In 1972, Wolff, Kompa and Mehran applied the method to analyze some microstrip discontinuities [24] by approximating the eigenfunctions using an equivalent waveguide model. In 1979, Arndt and Paul developed a hybrid-mode based expansion for the S-parameter analysis of shielded microstrip discontinuities [34]. The same year, Mehran presented a CAD software based on the MMM to design microstrip filters [25].

From 1982, Vahldieck and Bornemann adopted the method in the analysis of quasi-planar filters [22], [28] and [30]. The method was extended to fin-line structure in 1984 by Vahldieck [27] and later by Omar and Schunemann [23] and by Vahldieck and Hoefer [26].

The MMM in conjunction with the Generalized Scattering Matrix Technique (GSMT), introduced by Mittra and Pace [32], allows cascading of discontinuities. This technique is an extension of the conventional scattering matrix technique. In addition to keeping track of the first mode of a signal flowing from a junction, it includes the effect of higher order modes. This effect is very important in multi-modal transmission lines or when discontinuities are closely spaced in terms of electric length.

1.2.1 Theoretical foundation of the MMM

To illustrate the principal steps of this method, the general discontinuity problem shown in figure 1.2 is assumed. The waveguides are assumed to have perfectly conducting walls and they are filled with a lossless, isotropic and homogeneous medium. The aim is to characterize the discontinuity in terms of S-parameters:

$$\begin{aligned} B^{(1)} &= S_{11}A^{(1)} + S_{12}B^{(2)} \qquad (1.8) \\ A^{(2)} &= S_{21}A^{(1)} + S_{22}B^{(2)} \qquad (1.9) \end{aligned}$$

where A and B are the vectors containing the amplitudes, (A_n and B_n), of the different modes for the incoming and reflected waves in each subsection (Fig. 1.2.c). This relationship is derived from the definition of the vector potential and the matching of the transverse electromagnetic field at $z = 0$ (Fig. 1.2.c) $\vec{\Psi}$ in subregion (1) and (2) is composed of an infinite sum of orthogonal functions ($\vec{\Psi}_n$):

$$\vec{\Psi}_z = \sum_{n=1}^{\infty}(A_n + B_n)\vec{\Psi}_n \qquad (1.10)$$

These functions ($\vec{\Psi}_n$) must satisfy the Helmholtz equation (1.5) and the boundary condition in each subregion. For computer calculations, the infinite sum in (1.10) is approximated by truncating the series at N. Then, for the transverse (with respect to the z-direction) electric fields the continuity equation at $z = 0$ yields:

$$\begin{aligned} \vec{E}_2^T &= \vec{E}_1^T \qquad \text{over } S_1 \\ \vec{E}_2^T &= 0 \qquad \text{over } S_2 \end{aligned}$$

Since the electrical field is directly derived from the potential, these equations become:

$$\sum_{n=1}^{N}\left(A_n^{(1)} + B_n^{(1)}\right)e_n^{(1)} = \sum_{m=1}^{M}\left(A_m^{(2)} + B_m^{(2)}\right)e_m^{(2)} \qquad (1.11)$$

where (e_n) is a set of functions directly related, in each guide, to (Ψ_n), equations (1.6) and (1.7). (1.11) represents an equation system with $2(N + M)$ unknowns. It can be solved by taking advantage of the orthogonality property of the base which is:

$$\int_{S_1} e_n^{(1)}e_m^{(1)}w(s)dS = \begin{cases} \text{Constant} & \text{if } n = m \\ 0 & \text{if } n \neq m \end{cases}$$

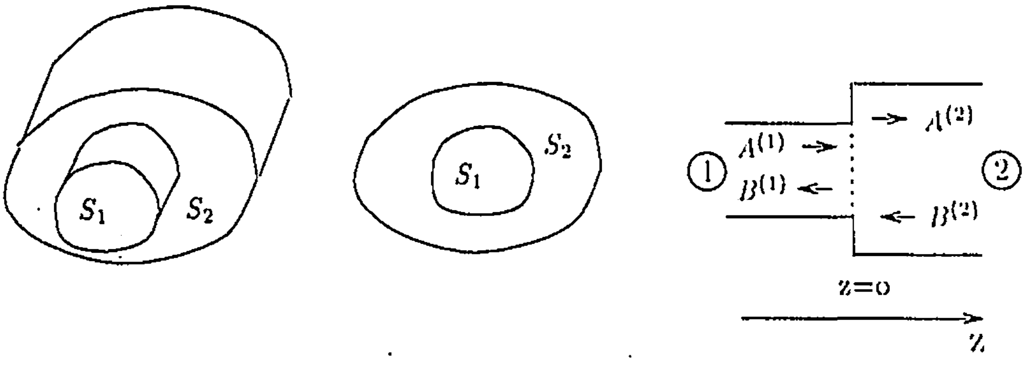

a) Perspective view b) Front View c) Side View

Figure 1.2: Example of an arbitrary shaped discontinuity

Multiplying (1.11) by $e_j^{(2)}$ and by integrating over $S_1 + S_2$, the equation becomes:

$$A_j^{(2)} + B_j^{(2)} = \sum_{n=1}^{N} \left(A_n^{(1)} + B_n^{(1)}\right) \int_{S_1} e_n^{(1)} e_j^{(2)} w(s) ds \tag{1.12}$$

w being the weight function which depends on the coordinate system. Equation (1.12) now represents a set of M equations. However, to find the relationships (1.8) and (1.9) an additional equation is necessary which must be linearly independent from equation (1.12). This equation is provided by the magnetic field continuity equation:

$$\vec{H}_1^T = \vec{H}_2^T \qquad \text{over} \quad S_1 \tag{1.13}$$

Again applying the orthogonal property, equation (1.13) yields:

$$A_j^{(1)} - B_j^{(1)} = \sum_{m=1}^{M} \left(A_m^{(2)} - B_m^{(2)}\right) \int_{S_1} e_m^{(2)} e_j^{(1)} w(s) ds \tag{1.14}$$

Equation (1.14) represents a second set of N equations which is independent from equation (1.12). Both equations can be rewritten in matrix notation:

$$A^{(2)} + B^{(2)} = LH.\left(A^{(1)} + B^{(1)}\right) \tag{1.15}$$

$$A^{(1)} - B^{(1)} = LE.\left(A^{(2)} - B^{(2)}\right) \tag{1.16}$$

In this set of equations, A and B are vectors representing the fundamental mode as well as higher order modes. Their interactions are represented by LH and LE. Rearranging (1.15) and (1.16) results in the scattering equations (1.8) and (1.9) for the single discontinuity. Details of this procedure are given in Appendix A.

In principle, the procedure as outlined above will repeat itself for different discontinuities and with different details of the boundary conditions.

The MMM represents a good trade-off between CPU-time requirements and memory space (see Table 1.1). In particular when only two field components are necessary to satisfy the matching conditions, the MMM is significantly faster and more accurate than other techniques that could be applied to the same problem. Therefore one focus of this thesis is to investigate the effect of matching only two field components, versus matching four field components.

Chapter 2

Parallel-connected diplexer

This chapter describes the analysis and design of an integrated millimeter-wave diplexer. The diplexer can be considered as a variation of the duplexer. The duplexer is a device that allows for example, a single antenna to serve both the transmitter and the receiver at the same frequency (i.e. [15], [16], [17]).

A typical problem in diplexer design is the separation of two different but close frequencies (i.e. separation of up and down links[1] [1]).

A new idea for a very compact design is proposed here (Fig. 2.1). It consists of two parallel-connected E-plane metal insert filters fed by an E-plane bifurcation which in turn is connected to a standard waveguide by a tapered section, which opens up the height of the feeding waveguide to match the bifurcation height. Because of its simplicity, this structure can be easily extended to triplexers or multiplexers.

The diplexer is composed of three types of discontinuities (Fig. 2.2): the E-plane step, the E-plane bifurcation and the H-plane bifurcation. The latter one, which is the basic element of the filter section, has been extensively analyzed [22], [26].

---

[1] for example, 5.93-6.42 GHz and 3.705-4.195 GHz for, respectively, the up link and down link signal, aboard the INTELSAT satellite

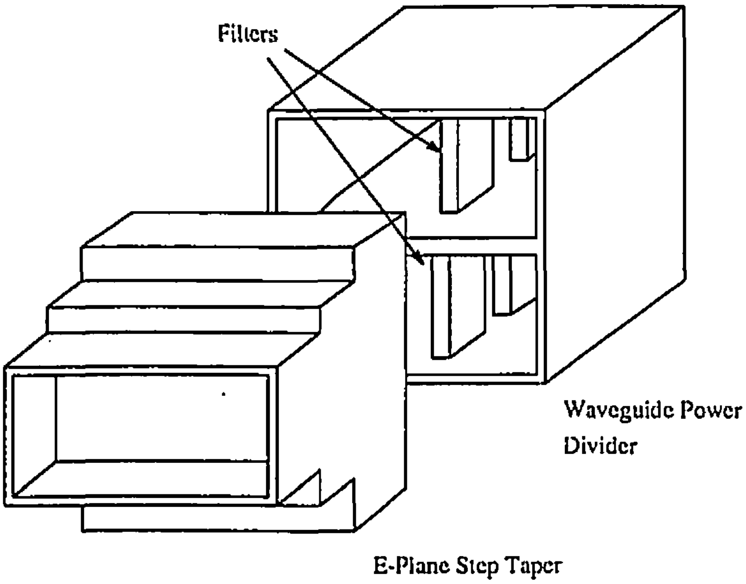

Figure 2.1: Mechanical composition of the diplexer.

The E-plane step and the E-plane bifurcation have been analyzed only recently by Dittloff et al. ([18] and [19]). Their analysis was based on a full-wave approach, using the linear superposition of two vector potentials (TE and TM). This approach leads to six field components from which four of them (transverse to the propagation direction) need to be included in the continuity condition.

However, if a TE_{10} incident mode is assumed, the transverse field is formed by only three field components, because there is no E_x component at any points in the discontinuity.

In general, the use of only one vector potential leads to five field components. If two of them are pointing in the propagation direction (which is the case when the field is calculated from the Ψ_x vector potential), the remaining three are transverse components from which only two are required for the matching condition at the discontinuity. This allows a simple and fast procedure without any loss of accuracy. Results will be

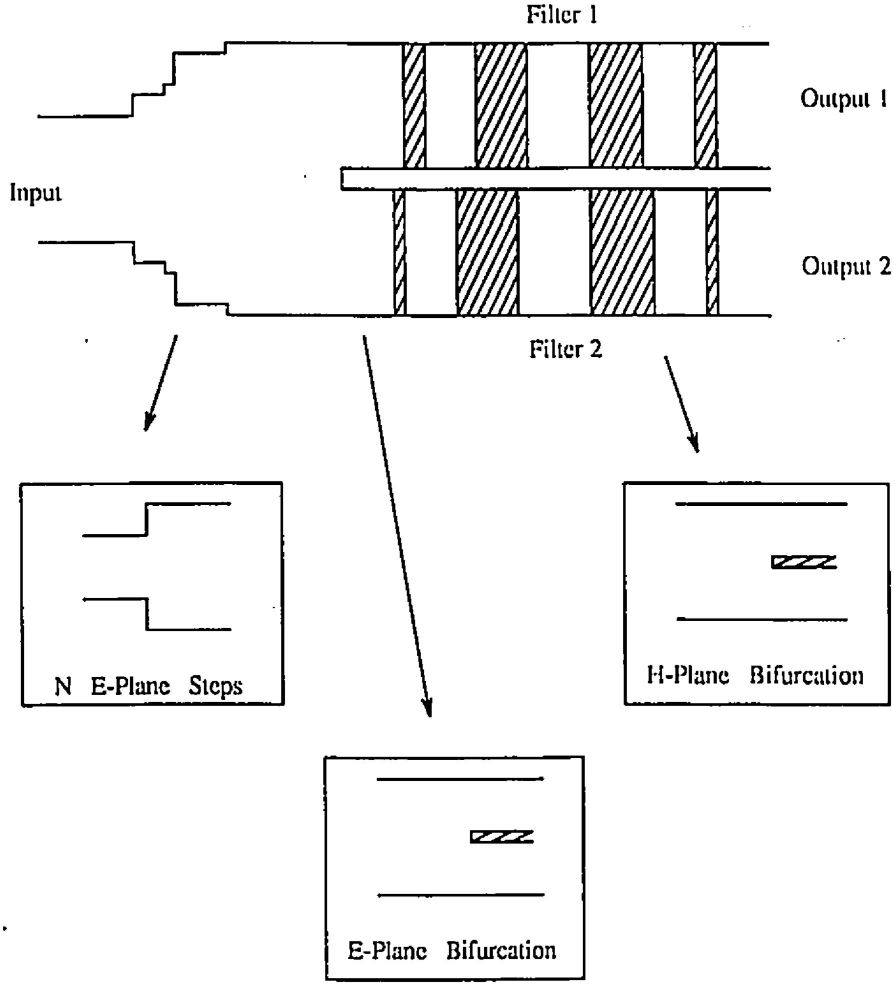

Figure 2.2: Decomposition of the diplexer into simple discontinuity elements: a) E-plane step, b) E-plane bifurcation and c) H-plane bifurcation.

compared with [18].

Both types of discontinuities are based on the same procedure, therefore, this chapter presents details of the E-plane step analysis only, from which the principal steps for the E-plane bifurcation analysis are deducted.

2.1 Vector potential

The discontinuity under investigation is shown in Fig. 2.3. If a TE_{10} incident wave is assumed, there is no E_x component excited at any point of the discontinuity. The x-component of the vector potential $\vec{\Psi}_x^{(h)}$ (known as the Fitzgerald vector) is then sufficient to describe the fields at this discontinuity. Therefore, for a TE^x wave [2] the field is calculated from [20]:

$$\vec{E} = -j\omega\mu_0 \vec{\nabla} \times \vec{\Psi}_x^{(h)} \tag{2.1}$$

$$\vec{H} = \vec{\nabla} \times \vec{\nabla} \times \vec{\Psi}_x^{(h)} \tag{2.2}$$

The vector potential must satisfy the Helmholtz equation and the boundary conditions. Then, in terms of normal modes :

$$\Psi_{x\,m,n}^{(h)} = T_{m,n} sin(k_{x_m} x) cos(k_{y_n} y) \left(A_{m,n} e^{-j\beta_{m,n} z} - B_{m,n} e^{j\beta_{m,n} z} \right) \tag{2.3}$$

with $k_{x_m} = m\pi/a$ and $k_{y_n} = n\pi/b$. The propagation constant is evaluated from:

$$\beta_{m,n}^2 = k_0^2 \varepsilon_r - k_{x_m}^2 - k_{y_n}^2 = k_0^2 \varepsilon_r - (\frac{m\pi}{a})^2 - (\frac{n\pi}{b})^2$$

with the properties:

$$\int_S sin(k_{x_m} x) sin(k_{x_p} x) dx = D_x \delta_{m,p} \tag{2.4}$$

$$\int_S cos(k_{y_m} y) cos(k_{y_p} y) dy = D_y \delta_{m,p} \tag{2.5}$$

---

[2] noted sometimes in the literature : LSM wave (Longitudinal Section Magnetic)

where S is the waveguide cross-section, D_x and D_y are constants depending on the waveguide dimensions, and $\delta_{m,p}$ denotes the Kronecker symbol.

Thus, by inserting equation 2.3 in (2.1) and (2.2), the six field components of the $TE^x_{m,n}$ mode can be expressed as ($m = 1 \longrightarrow \infty, n = 0 \longrightarrow \infty$):

$$\begin{aligned}
E_x &= 0 \\
E_y &= -\omega\mu_0 T_{m,n}\beta_{m,n} sin(k_{x_m}x)cos(k_{y_n}y)\left(A_{m,n}e^{-j\beta_{m,n}z} + B_{m,n}e^{j\beta_{m,n}z}\right) \\
E_z &= j\omega\mu_0 T_{m,n} sin(k_{x_m}x)(-k_{y_n})sin(k_{y_n}y)\left(A_{m,n}e^{-j\beta_{m,n}z} - B_{m,n}e^{j\beta_{m,n}z}\right)
\end{aligned}$$

(2.6)

$$\begin{aligned}
H_x &= (k_0^2\varepsilon_r - k_{x_m}^2)T_{m,n} sin(k_{x_m}x)cos(k_{y_n}y)\left(A_{m,n}e^{-j\beta_{m,n}z} - B_{m,n}e^{j\beta_{m,n}z}\right) \\
H_y &= -T_{m,n}k_{x_m}k_{y_n} cos(k_{x_m}x)sin(k_{y_n}y)\left(A_{m,n}e^{-j\beta_{m,n}z} - B_{m,n}e^{j\beta_{m,n}z}\right) \\
H_z &= -jT_{m,n}k_{x_m}\beta_{m,n} cos(k_{x_m}x)cos(k_{y_n}y)\left(A_{m,n}e^{-j\beta_{m,n}z} + B_{m,n}e^{j\beta_{m,n}z}\right)
\end{aligned}$$

$T_{m,n}$ denotes the normalization factor of the amplitude coefficients, which is $\sqrt{1W}$. $T_{m,n}$ is calculated from:

$$P_{m,n} = \int\int_S (\vec{E} \times \vec{H}).d\vec{S} = 1.0W \tag{2.7}$$

which yields

$$T_{m,n} = \frac{2}{\sqrt{\omega\mu_0\beta_{m,n}\left(\beta_{m,n} + (\frac{n\pi}{b})^2\right)ab}} \tag{2.8}$$

2.2 Matching condition

2.2.1 Matching the electric field

The electromagnetic field has been expressed as an infinite sum of modal vectors. Applying the continuity conditions at the junction ($z = 0$) (see Fig. 2.3):

$$\begin{aligned} E_y^{(2)} &= E_y^{(1)} && y \in [c_y, d_y] \quad \forall x \in [0, a] \\ &= 0 && \text{otherwise,} \end{aligned}$$

and using the property of mode orthogonality, results in the following coupling equation:

$$\begin{aligned} &\int_0^a \int_0^B \sum_{m=1}^{\infty} \sum_{n=o}^{\infty} -\omega\mu_0 T_{m,n}^{(2)} \beta_{m,n}^{(2)} sin(\frac{m\pi}{a} x) cos(\frac{n\pi}{B} y) \\ &\quad \left(A_{m,n}^{(2)} + B_{m,n}^{(2)}\right) sin(\frac{i\pi}{a} x) cos(\frac{k\pi}{B} y) dx dy = \\ &\int_0^a \int_{c_y}^{d_y} \sum_{m=1}^{\infty} \sum_{n=o}^{\infty} -\omega\mu_0 T_{m,n}^{(1)} \beta_{m,n}^{(1)} sin(\frac{m\pi}{a} x) cos(\frac{n\pi}{b} (y - c_y)) \\ &\quad \left(A_{m,n}^{(1)} + B_{m,n}^{(1)}\right) sin(\frac{i\pi}{a} x) cos(\frac{k\pi}{B} y) dx dy \end{aligned} \tag{2.9}$$

On the LHS of the equation, both integrals lead to D_x and D_y (defined in 2.4 and 2.5). On the RHS, only the x-integral leads to a constant. Hence, 2.9 yields:

$$T_{i,k}^{(2)} \frac{a}{2} \frac{B}{2} \beta_{i,k}^{(2)} \left(A_{i,k}^{(2)} + B_{i,k}^{(2)}\right) = \sum_{n=o}^{\infty} T_{i,n}^{(1)} \frac{a}{2} J_{k,n} \beta_{i,n}^{(1)} \left(A_{i,n}^{(1)} + B_{i,n}^{(1)}\right) \tag{2.10}$$

with

$$J_{k,n} = \int_{c_y}^{d_y} cos(\frac{n\pi}{b}(y - c_y)) cos(\frac{k\pi}{B} y) dy$$

Isolating the amplitude coefficient in equation (2.10) leads to:

$$A_{i,k}^{(2)} + B_{i,k}^{(2)} = \sum_{n=o}^{\infty} \frac{2}{B} \frac{T_{i,n}^{(1)}}{T_{i,k}^{(2)}} \frac{\beta_{i,n}^{(1)}}{\beta_{i,k}^{(2)}} J_{k,n} \left(A_{i,n}^{(1)} + B_{i,n}^{(1)}\right) \tag{2.11}$$

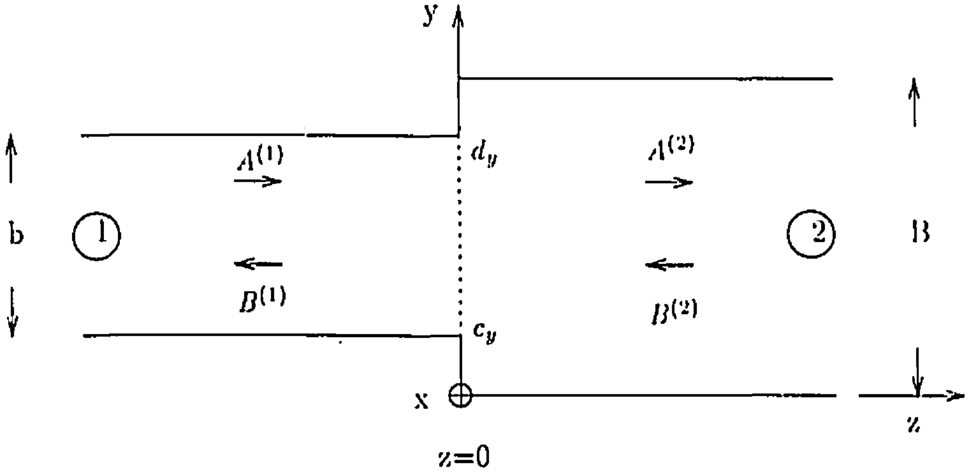

Figure 2.3: Side view of an E-plane step discontinuity.

Or in matrix form:

$$A^{(2)} + B^{(2)} = LH\left(A^{(1)} + B^{(1)}\right) \tag{2.12}$$

i, k and i, n denote the different modes in each subregions ($A^{(1)}_{i,n}$ and $B^{(1)}_{i,n}$ with $n = 0 \rightarrow \infty$ in guide (1) and $A^{(2)}_{i,k}$ and $B^{(2)}_{i,k}$ with $k = 0 \rightarrow \infty$ in guide (2)). For computer simulation, the vector expansion is limited to N in guide (1) and to K in guide (2).

2.2.2 Matching the magnetic field

Matching only the E-field is not sufficient to characterize the discontinuity. A second equation is needed which is independent from (2.12). This equation is provided by the H_x-field ($\forall x \in [0, a]$) :

$$H_x^{(2)} = H_x^{(1)} \qquad y \in [c_y, d_y]$$

Following the same procedure as for the E_y-field leads to:

$$A_{i,k}^{(1)} - B_{i,k}^{(1)} = \sum_{n=o}^{\infty} \frac{2}{b} \frac{k_0^2 \varepsilon_r^{(2)} - (\frac{i\pi}{a})^2}{k_0^2 \varepsilon_r^{(1)} - (\frac{i\pi}{a})^2} \frac{T_{i,n}^{(2)}}{T_{i,k}^{(1)}} J_{n,k} \left(A_{i,n}^{(2)} - B_{i,n}^{(2)} \right) \tag{2.13}$$

$$A^{(1)} - B^{(1)} = LE \left(A^{(2)} - B^{(2)} \right) \tag{2.14}$$

It can been shown that $LE = LH^t$.

Using the $\vec{\Psi}_x^{(h)}$ vector potential, one problem remains : there are three continuity conditions (E_y, H_x and H_y) and only two unknown vector quantities: $B^{(1)}$ and $A^{(2)}$ (the outgoing wave coefficients). The independence of the three continuity conditions (E_y, H_x and H_y) can be verified by writing the third one:

$$H_y^{(2)} = H_y^{(1)} \quad y \in [c_y, d_y] \quad \forall x \in [0, a]$$

Applying the previously described procedure, this equation leads to:

$$A_{i,k}^{(1)} - B_{i,k}^{(1)} = \sum_{n=o}^{\infty} \frac{2}{b} \frac{T_{i,n}^{(2)}}{T_{i,k}^{(1)}} J_{n,k} \left(A_{i,n}^{(2)} - B_{i,n}^{(2)} \right) \tag{2.15}$$

Therefore, equations (2.13) and (2.15) are linearly independent if and only if $\varepsilon_r^{(1)} = \varepsilon_r^{(2)}$.

If a TE_{10}^x mode excitation is assumed, the matrices LE and LH are the coupling matrices connecting the $TE_{1,n}^x$ modes in guide (1) to the $TE_{1,m}^x$ modes the guide (2). Rearranging equations (2.14) and (2.12) leads to the S-matrix of the E-plane step discontinuity.

$$\begin{pmatrix} B^{(1)} \\ A^{(2)} \end{pmatrix} = \begin{pmatrix} S_{11} & S_{12} \\ S_{21} & S_{22} \end{pmatrix} \begin{pmatrix} A^{(1)} \\ B^{(2)} \end{pmatrix} \tag{2.16}$$

Details of this procedure are given in appendix A.

2.2.3 E-plane bifurcation

The procedure to obtain the S-matrix of an E-plane bifurcation is very similar to that of an E-plane step. Therefore, this section will present only the important steps.

The starting point is again the potential vector described in section 2.1 from which the E- and H-field can be expressed as in equation (2.6). Then the continuity condition is applied at the discontinuity plane (see Fig. 2.4):

$$
\begin{aligned}
E_y^{(1)} &= E_y^{(2)} && y \in [0, c_y] \quad \forall x \in [0, a] \\
&= E_y^{(3)} && y \in [d_y, c_y] \quad \forall x \in [0, a] \\
&= 0 && \text{otherwise,}
\end{aligned}
$$

This continuity condition can be rewritten as:

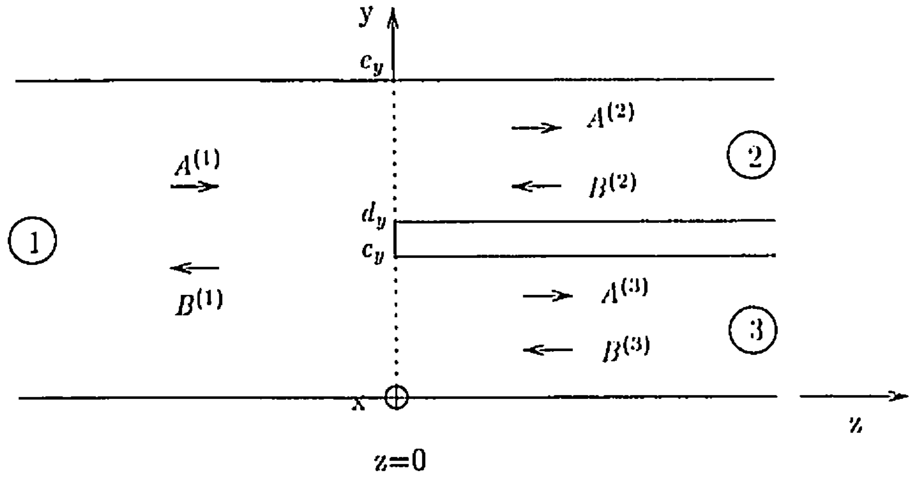

Figure 2.4: Side view of an E-plane bifurcation.

$$E_y^{(1)} = E_y^{(2)} + E_y^{(3)} \tag{2.17}$$

with $E_y^{(2)}$ and $E_y^{(3)}$ zero outside guide (2) and (3), respectively. Following the same procedure defined in section 2.2.1 (e.g. multiplying both sides of 2.17 with eigenfunctions of section (1) and integrating over the cross-section) leads to:

$$A^{(1)} + B^{(1)} = LH^{(2)}\left(A^{(2)} + B^{(2)}\right) + LH^{(3)}\left(A^{(3)} + B^{(3)}\right) \tag{2.18}$$

A second and third equation can be found by applying the H_x-field matching condition:

$$\begin{aligned} H_x^{(1)} &= H_x^{(2)} \qquad y \in [0, c_y] \quad \forall x \in [0, a] \\ &= H_x^{(3)} \qquad y \in [d_y, e_y] \quad \forall x \in [0, a] \end{aligned}$$

which yields:

$$A^{(2)} - B^{(2)} = LE^{(2)} \left(A^{(1)} - B^{(1)} \right) \tag{2.19}$$

$$A^{(3)} - B^{(3)} = LE^{(3)} \left(A^{(1)} - B^{(1)} \right) \tag{2.20}$$

Rearranging all three equations leads to the three-port scattering matrix of the E-plane discontinuity:

$$\begin{pmatrix} B^{(1)} \\ A^{(2)} \\ A^{(3)} \end{pmatrix} = \begin{pmatrix} S_{11} & S_{12} & S_{13} \\ S_{21} & S_{22} & S_{23} \\ S_{31} & S_{32} & S_{33} \end{pmatrix} \begin{pmatrix} A^{(1)} \\ B^{(2)} \\ B^{(3)} \end{pmatrix} \tag{2.21}$$

2.3 Convergence analysis

The convergence behavior depends on the ratio q/p of the number of modes taken into account in each guide. The best convergence behavior is obtained when this ratio is equal to the ratio of the waveguide heights. This is shown in Figure 2.5 and the results confirm those from [36]. Since the step ratio is 2:1, the optimum behavior is obtained for $q = 2p$. Although the choice of q/p can be different, other ratios will lead to slower convergence.

A similar convergence analysis can be performed with the height as a parameter in Ka-band (Fig. 2.6) and in W-band (Fig. 2.7) or with the frequency (Fig. 2.8). These curves, computed with the same number of modes in both guides, show the convergence speed decreases with the size of the step and with frequency. Figure 2.9 presents the convergence analysis for a power divider (the dimension are given in Table 2.1).

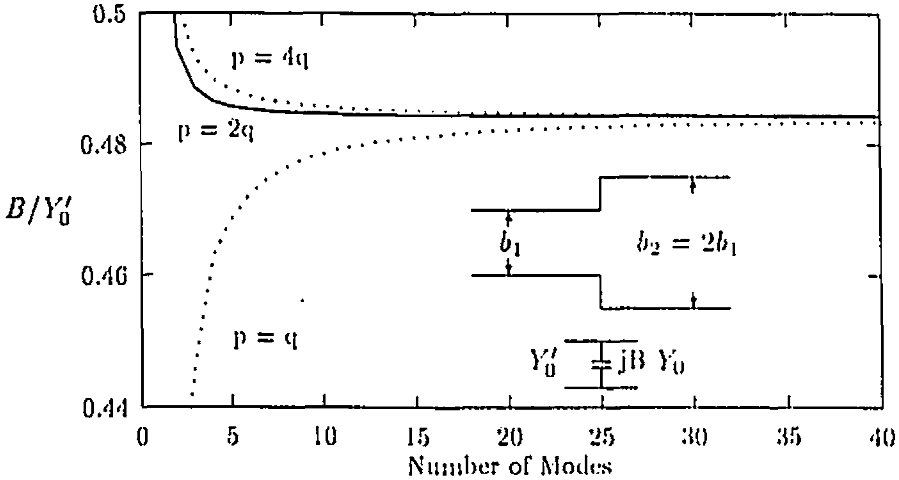

Figure 2.5: Convergence analysis of an E-plane step discontinuity and its equivalent capacitance.

The convergence speed can be improved by taking advantage of the structural symmetry of the step, which means considering only even modes with respect to the y-direction[3].

Only the first 6 or 8 modes are necessary, which is small in comparison with the calculations done for the same kind of structure by Dittloff [19]. The method in [19] uses two potential vectors, $\Psi_z^{(h)}$ and $\Psi_z^{(e)}$, and reaches convergence only with a large number, about fifteen, of TE and TM modes.

---

[3] considering odd modes with respect to the x-direction is not necessary, because the S-matrix links $TE_{1,k}^{(1)}$ to $TE_{1,n}^{(2)}$.

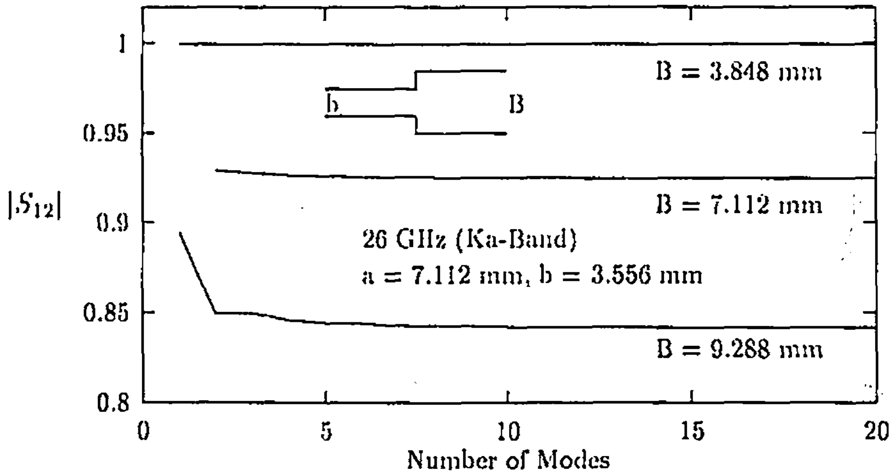

Figure 2.6: Convergence analysis of an E-plane step discontinuity.

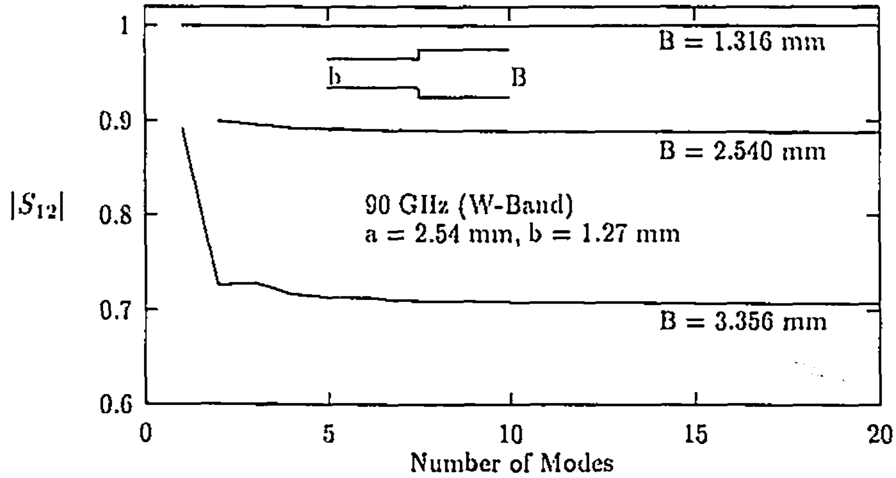

Figure 2.7: Convergence analysis of an E-plane step discontinuity.

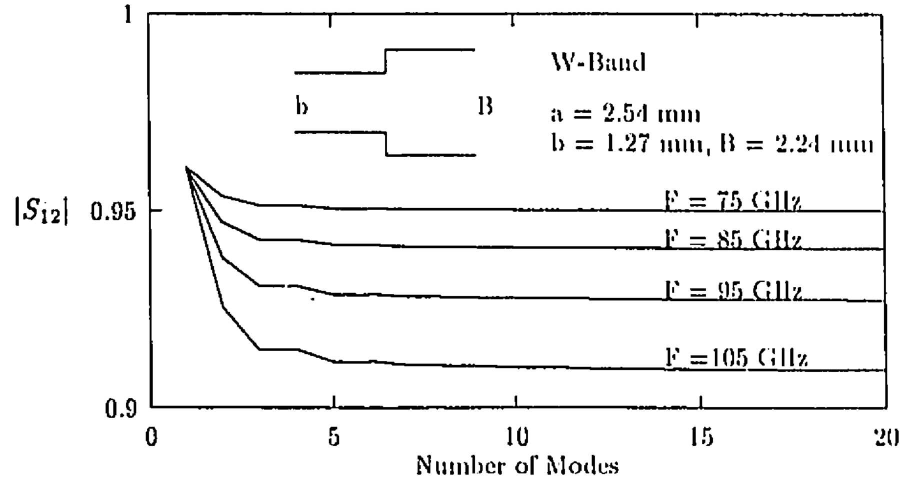

Figure 2.8: Convergence analysis of an E-plane step discontinuity with the frequency as parameter.

2.4 Power divider

In the following, step discontinuities are cascaded to taper the feeding waveguide into the E-plane bifurcation. Figure 2.10 shows an X-band narrow band power divider (design and measurement by [18]). The comparison between measured and computed results is excellent.

Figure 2.11 shows the frequency response of a tapered W-band power divider. The frequency range over which the return loss is greater than 30 *dB*[4], is 20 *GHz*.

Figures 2.12 and 2.13 show an example for a 3-Channel power divider (4.77 *dB*) over a 10 *GHz* bandwidth. It can be observed that the power distribution into the three channels is not equal. The coefficient S_{31} (transmission to the middle channel) is

---

[4] the insertion loss is less than 3.016 *dB* (theoretical value: 3.0103 *dB*) over the same bandwidth

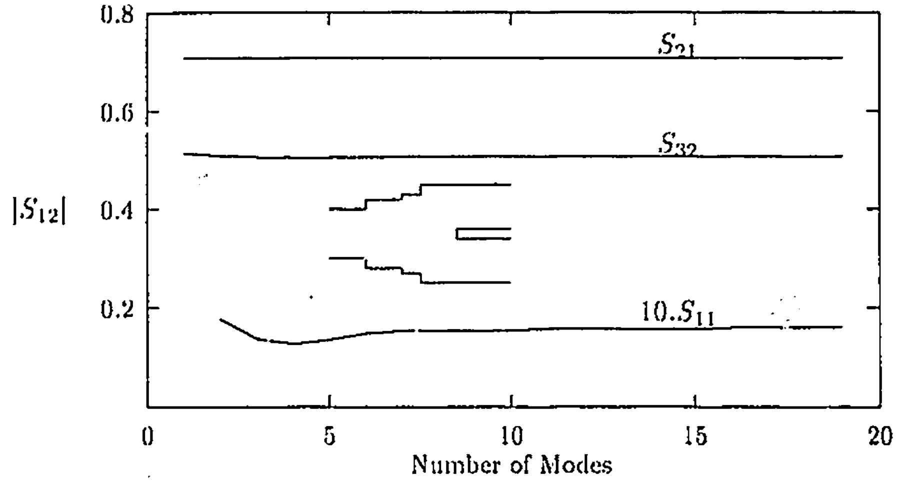

Figure 2.9: Convergence analysis for a W-band power divider (at 90 GHz), fed by a 5-step taper transition (data in Table 2.1)

slightly different from the coefficients S_{21} and S_{41} (transmission to the upper and lower channel) which is due to the different power distribution in y-direction in the last step of the taper. The power distribution reaches a peak in the middle, right in front of channel 2.

2.5 Diplexer-Triplexer

2.5.1 Diplexer

The power divider structure can be combined with filters. Using E-plane metal insert filters leads to a very compact and easy to fabricate diplexer or triplexer device. Both filters can be photolithographically etched from a single metallic sheet and then embedded into the split block housing as shown in Figure 2.14.

The scattering matrix of the filters contains only $TE^x_{n,0}$ modes. However, the power

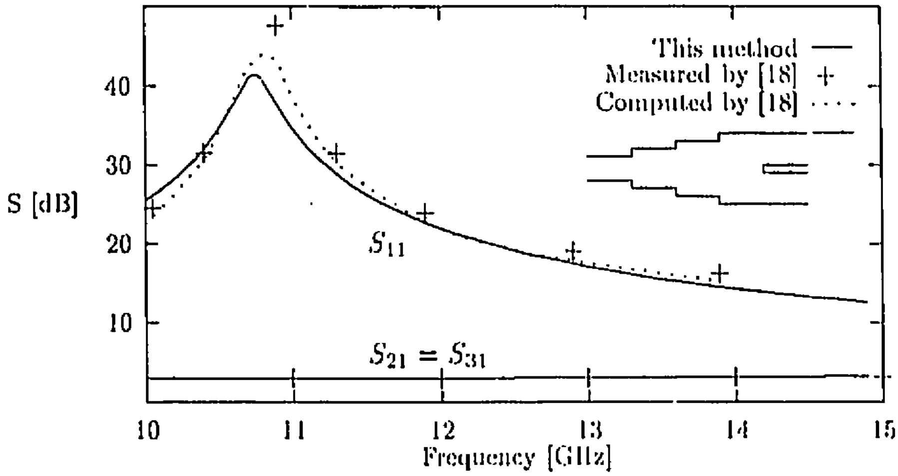

Figure 2.10: Frequency response of an optimized tapered X-band power divider.

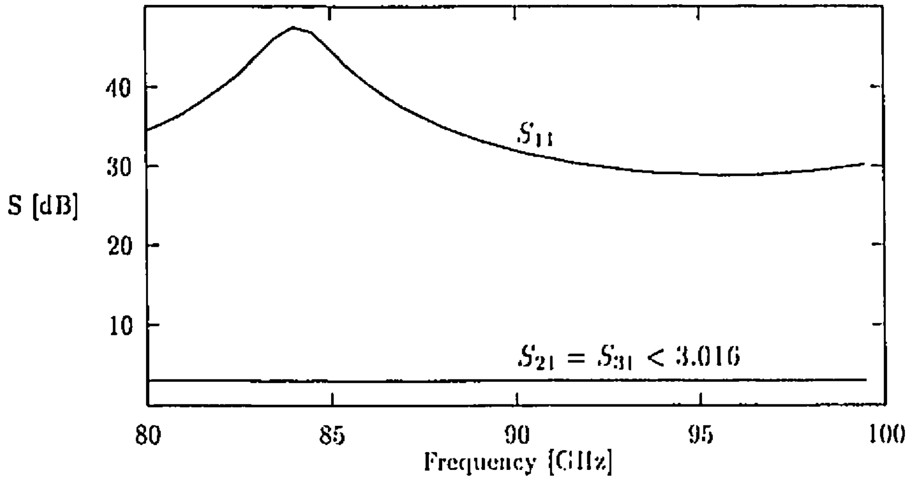

Figure 2.11: Frequency response of an optimized tapered W-band power divider.

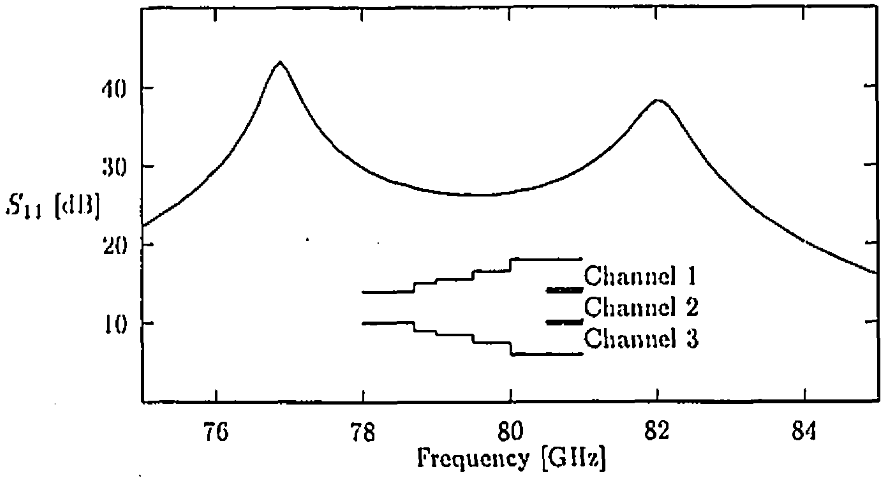

Figure 2.12: Return loss versus frequency for an optimized W-band 3-channel power divider.

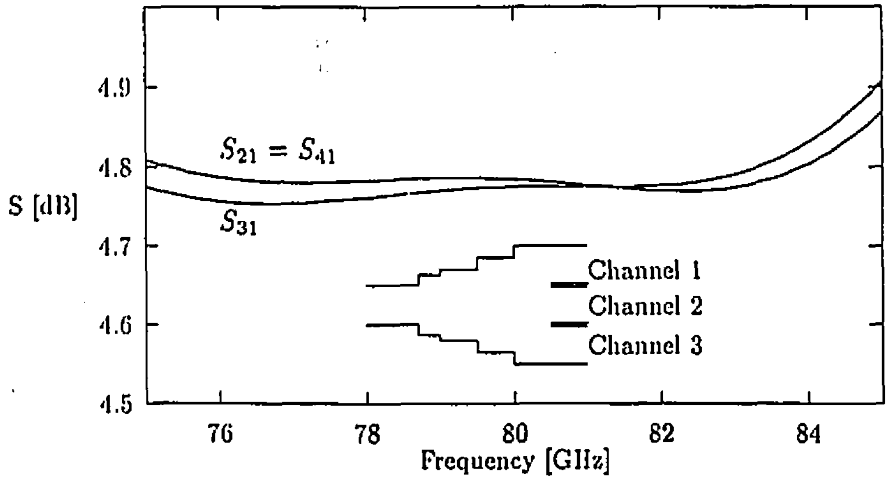

Figure 2.13: Insertion loss versus frequency of the different channels of an optimized W-Band 3-channel power divider.

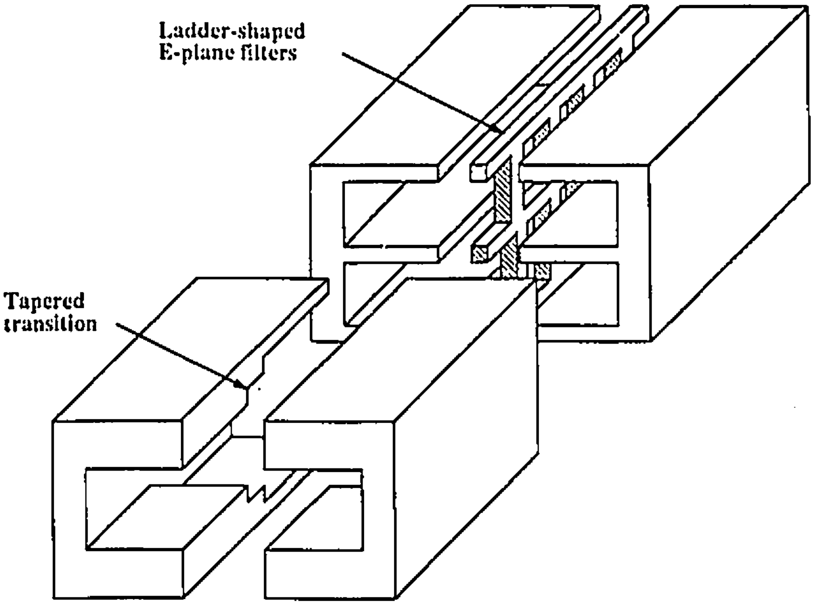

Figure 2.14: Perspective view of the diplexer arrangement with ladder-shaped metal insert E-plane filters.

divider S-matrix connects $TE^x_{i,n}$ modes with i constant. If d_1 and d_2, the respective length in front of each channel (see Table 2.1), are "long enough", the $TE^x_{i,n}$ modes with $i > 1$ and $n > 0$ vanish rapidly and their effects on the filters become almost non-existent. Therefore, to interconnect the tapered bifurcation with the filters, only the part of the S-matrices that contains $TE^x_{i,0}$ modes is considered. That requires calculation of the S-matrix of the tapered bifurcation with different $TE^x_{i,0}$ excitation several times and to store only the $TE^x_{i,0}$-to-$TE^x_{i,0}$ elements.

The first example is a Ka-band diplexer designed at 28.2 GHz and 32.7 GHz (see Fig. 2.15). The second example is a W-band diplexer designed at 93.5 GHz and 96.0 GHz (see Fig. 2.16). The corresponding data is given in Tables 2.1 and 2.2. In the W-band example, a theoretical return loss better than 20 dB ($S_{21} < 0.05$ dB) has been achieved in both channels. Such good performance could not be obtained with the Ka-band diplexer because both channels are closer to the cut-off frequency[5]. This means the dispersion effect is more pronounced and, therefore, the taper is not as good over the wide frequency range it was designed for.

2.5.2 Double band-pass filter

Combining the output of the diplexer by the same power combiner as the one at the input leads to a double bandpass filter, which can be useful for different applications. One application may be for high power signals where the power is too high for a single filter to handle. In this case, the power is split into two channels with both filters working at the same center frequency. Another application may be to design an extreme broadband filter where the passband of one filter starts at the end of the other passband.

A double band-pass filter has been designed with a 2.0 GHz guard band and more than 25.0 dB rejection between both passbands. The theoretical insertion loss is less than 0.5 dB in both passbands (Fig. 2.17).

2.5.3 Triplexer

Expanding the bifurcation to a trifurcation leads to a triplexer for which the performance is given in Figure 2.18. A good optimized triplexer was difficult to obtain. One reason is that the power distribution into the different channels is not perfectly equal. Another reason has to do with the propagation of the first higher order mode in the last section of the taper. Thus, part of the energy of the fundamental mode is transferred into this second mode and it is difficult to control it. The dimension of this last section is 2.54 mm × 4.01 mm. Calculating the first three propagation constants

---

[5] WR-28 waveguide: 21.081 GHz

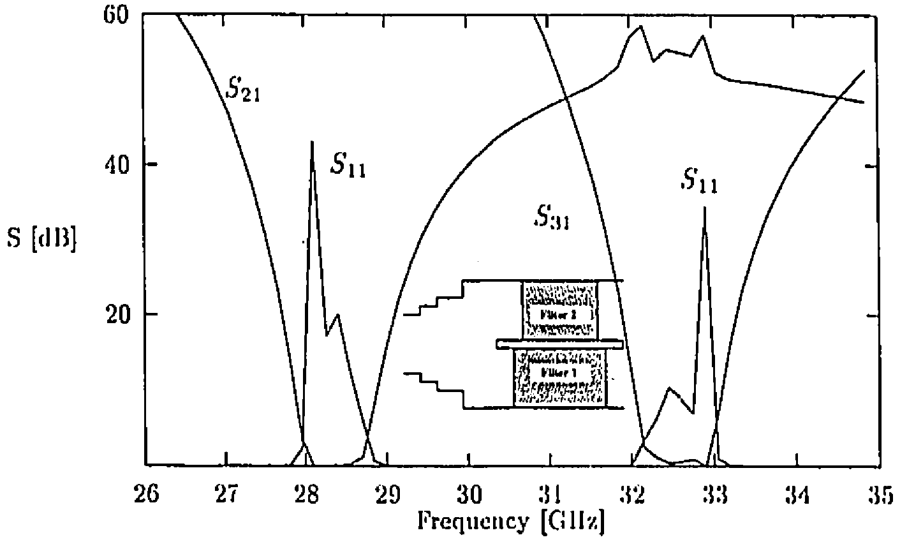

Figure 2.15: Frequency response of the optimized Ka-band diplexer.

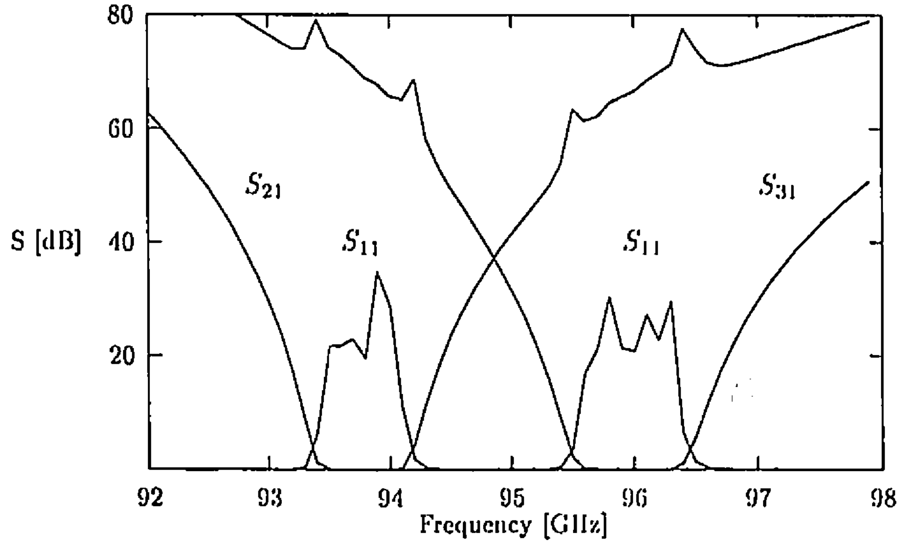

Figure 2.16: Frequency response of the optimized W-band diplexer.

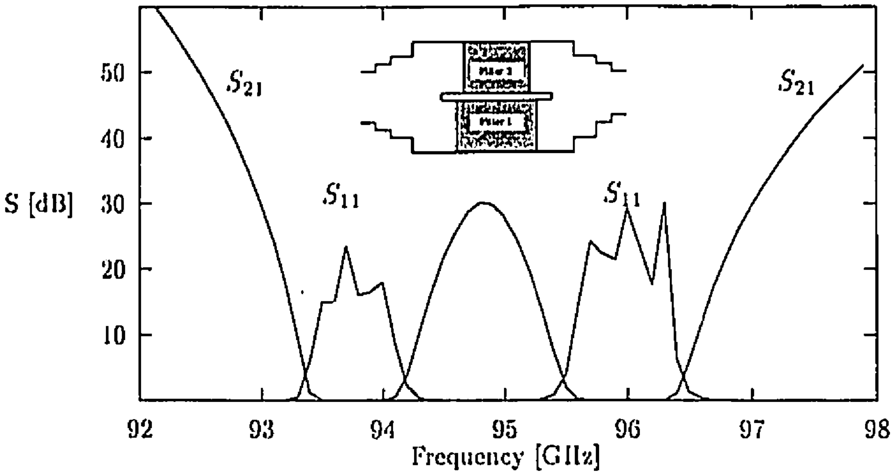

Figure 2.17: Frequency response of an optimized double-band filter.

at 90 GHz gives the following values:

$$TE_{10} \; : \; \beta = 1424.14m^{-1}$$

$$TE_{11} \; : \; \beta = 1189.29m^{-1}$$

$$TE_{12} \; : \; \beta = -j653.40m^{-1}$$

Therefore, in the last section of the tapered feeder, the TE_{11} mode can propagate once excited.

In case of a parallel-connected multiplexer with a number of output channels larger than three, both problems (power distribution and propagation of higher order modes) are detrimental to good device performance.

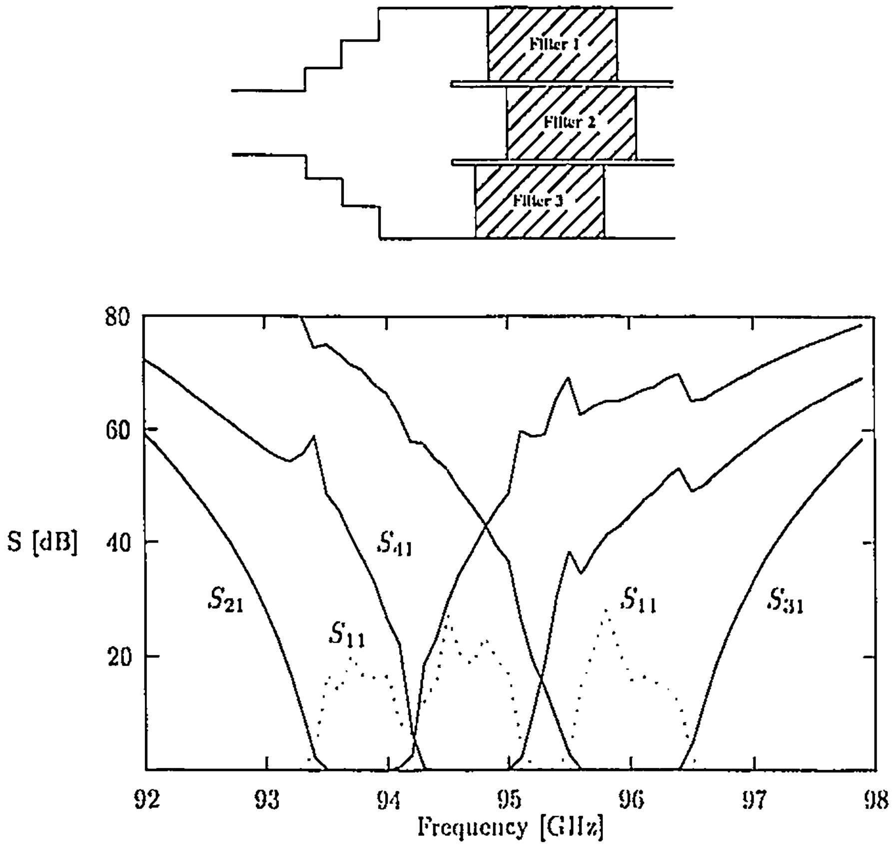

Figure 2.18: Frequency response of the optimized W-band triplexer.

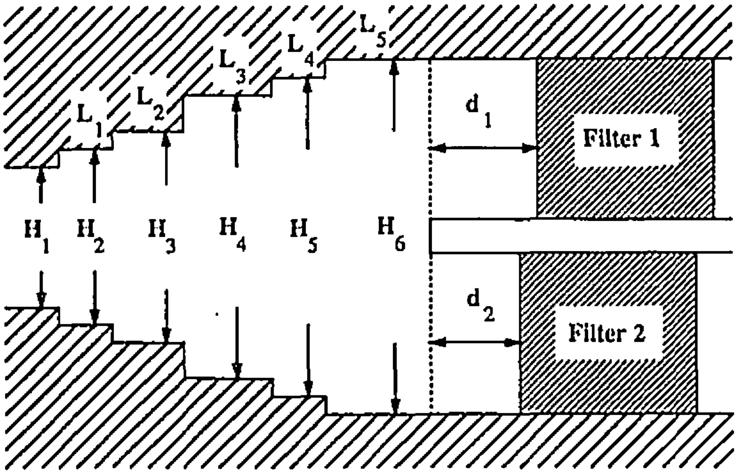

	Two Channels				Three Channels	
	Power Divider		Diplexer		Power Div.	Triplexer
	X-Band	W-Band	Ka-Band	W-Band	W-Band	W-Band
a	19.05	2.54	7.112	2.540	2.54	2.54
L_1	6.75	1.080	8.95	1.95	1.55	2.60
L_2	6.25	1.125	8.25	1.62	2.19	2.60
L_3	3.78	1.055	8.55	0.19	1.99	0.36
L_4	6.74	1.077	8.45	1.46	1.77	2.10
L_5	6.80	1.563	8.30	0.60	2.30	0.17
H_1	9.525	1.27	3.556	1.270	1.270	1.270
H_2	9.74	1.316	3.684	1.309	1.772	1.279
H_3	10.55	1.489	4.169	1.489	2.340	1.388
H_4	13.12	1.847	5.216	1.847	2.938	2.436
H_5	15.12	2.347	6.632	2.347	3.482	3.152
H_6	19.07	2.64	7.612	2.640	4.010	4.010
d_1			6.05	1.65		1.90
d_2			5.95	1.74		1.35
d_3						1.52

Table 2.1: Mechanical dimensions of the X-Band power divider, W-Band power divider, Ka-band and W-band filters (all dimensions in millimeters).

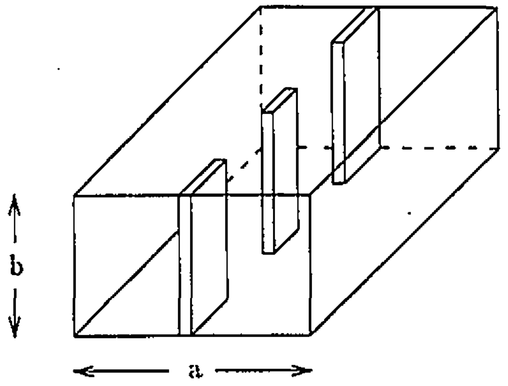

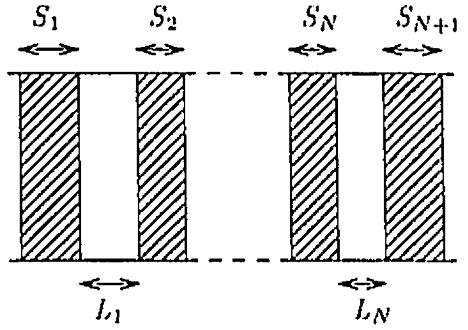

	Ka-band		W-band		
	Filter #1	Filter #2	Filter #1	Filter #2	Filter #3
a [mm]	7.112	7.112	2.54	2.54	2.54
b [mm]	3.556	3.556	1.27	1.27	1.27
f_0 [GHz]	28.35	32.59	93.77	95.97	94.67
N	3	4	4	4	4
S_1 & S_{N+1} [mm]	0.525	0.647	0.591	0.586	0.586
S_2 & S_N [mm]	2.539	3.446	1.829	1.829	1.829
S_3 [mm]		4.056	1.980	1.980	1.980
L_1 & L_N [mm]	6.311	4.372	1.555	1.471	1.520
L_2 & L_{N-1} [mm]	6.397	4.400	1.557	1.473	1.522

Table 2.2: Mechanical dimensions of the Ka- and W-band metal insert filters.

Chapter 3

Double-step discontinuities

This chapter focuses on the analysis and design of a parallel-connected four-channel multiplexer. In the context of this chapter, some other structures (like iris filters or waveguide transformer) will be analyzed as well and compared with measured results available in the literature in order to verify the accuracy of the approach taken.

The disadvantage of the diplexer/multiplexer described in the previous chapter is the height of the last steps of the taper if the number of channels exceeds three. To reduce the size of the transition waveguide, the channels are parallel connected in two directions instead of one (Fig. 3.1). This is possible by utilizing a grid divider fed by a double step tapered transition to gradually match the transition plane between the feeding channel ($a \times b$) and the grid divider ($Na \times Mb$). Two new types of discontinuities are introduced in this chapter: the double-step discontinuity and the grid divider (Fig. 3.1). Since both discontinuities require an equivalent analysis, the emphasis on the following procedure is on the double-step discontinuity.

Three different approaches to analyze the discontinuity numerically are investigated. The first approach assumes five field components derived from $\vec{\Psi}_x^{(h)}$. The second approach considers the general case of six field components derived from a superposition

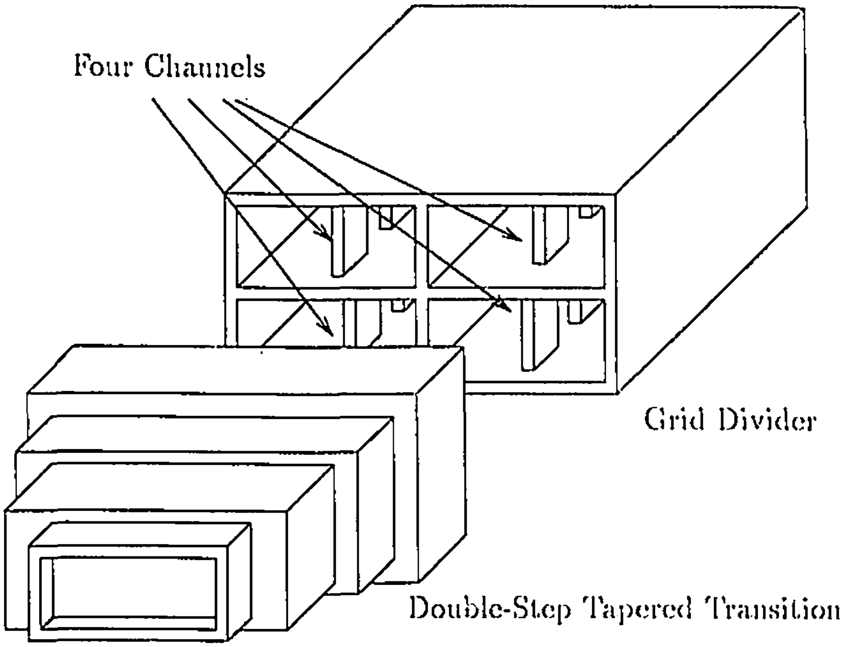

Figure 3.1: Mechanical composition of the quadriplexer.

of $\vec{\Psi}_x^{(h)}$ and $\vec{\Psi}_x^{(e)}$ vector potentials. The third approach uses a variation of the first one by using H_x and/or H_y field components to be matched at the discontinuity.

3.1 TE^x approach

In the case of the discontinuity described in figure 3.2, it is first assumed that the E_x component is still zero at any point of the discontinuity. Therefore, $\vec{\Psi}_x^{(h)}$, already defined in the previous chapter, is again sufficient to describe the electromagnetic field. The E_y continuity condition at $z = 0$ (Fig. 3.2) yields:

$$\begin{aligned} E_y^{(2)} &= E_y^{(1)} \qquad x \in [c_x, d_x] \quad y \in [c_y, d_y] \\ &= 0 \qquad\quad \text{otherwise,} \end{aligned}$$

Multiplying both sides of the equation by the normal functions of region 2, integrat-

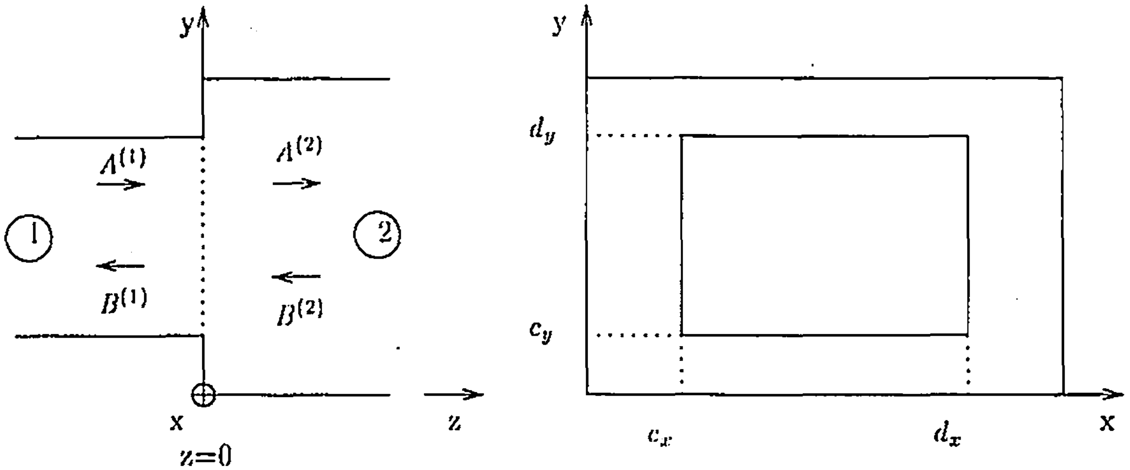

Figure 3.2: Detail of the double step discontinuity.

ing within the boundaries and finally using the property of mode orthogonality, the continuity equation becomes:

$$
\begin{aligned}
A^{(2)}_{i,j} + B^{(2)}_{i,j} &= \sum_{m=1}^{\infty}\sum_{n=o}^{\infty} \frac{4}{AB}\frac{T^{(1)}_{m,n}}{T^{(2)}_{i,j}}\frac{\beta^{(1)}_{m,n}}{\beta^{(2)}_{i,j}}\left(A^{(1)}_{m,n}+B^{(1)}_{m,n}\right) I_{i,m}\frac{J_{j,n}}{\sqrt{1+\delta_{0,n}}\sqrt{1+\delta_{0,j}}} &(3.1)\\
A^{(2)}+B^{(2)} &= LH\left(A^{(1)}+B^{(1)}\right) &(3.2)
\end{aligned}
$$

where $I_{i,m}$ and $J_{j,n}$ are the coupling integrals defined by:

$$
\begin{aligned}
I_{i,m} &= \int_{c_x}^{d_x} \sin\left(\frac{m\pi}{a}(x-c_x)\right)\sin\left(\frac{i\pi}{A}x\right)dx &(3.3)\\
J_{j,n} &= \int_{c_y}^{d_y} \cos\left(\frac{n\pi}{b}(y-c_y)\right)\cos\left(\frac{j\pi}{B}y\right)dy &(3.4)
\end{aligned}
$$

where a × b and A × B are the cross-section dimensions of the smaller and bigger waveguide, respectively.

A second equation is necessary to solve the problem mathematically and to ensure the field continuity for all fields. This equation is obtained by using the H_x-continuity condition at the discontinuity (Fig. 3.2):

$$H_x^{(2)} = H_x^{(1)} \qquad x \in [c_x, d_x] \quad y \in [c_y, d_y] \tag{3.5}$$

The same procedure applied to the E-field leads to the following equations:

$$A_{i,j}^{(1)} - B_{i,j}^{(1)} = \sum_{m=1}^{\infty} \sum_{n=o}^{\infty} \frac{4}{ab} \frac{k_0^2 \varepsilon_r^{(2)} - (\frac{m\pi}{A})^2}{k_0^2 \varepsilon_r^{(1)} - (\frac{i\pi}{a})^2} \frac{T_{m,n}^{(2)}}{T_{i,j}^{(1)}} I_{m,i} \frac{J_{n,j}}{\sqrt{1+\delta_{0,n}}\sqrt{1+\delta_{0,j}}} \left(A_{m,n}^{(2)} - B_{m,n}^{(2)}\right) \tag{3.6}$$

which can be written in matrix notation as:

$$A^{(1)} - B^{(1)} = LE\left(A^{(2)} - B^{(2)}\right) \tag{3.7}$$

Furthermore, $LE^t = LH$ since:

$$\frac{4}{ab} \frac{k_0^2 \varepsilon_r^{(2)} - (\frac{m\pi}{A})^2}{k_0^2 \varepsilon_r^{(1)} - (\frac{i\pi}{a})^2} \frac{T_{m,n}^{(2)}}{T_{i,j}^{(1)}} = \frac{4}{AB} \frac{\beta_{i,j}^{(1)}}{\beta_{m,n}^{(2)}} \frac{T_{i,j}^{(1)}}{T_{m,n}^{(2)}}$$

If a $TE_{1,0}^x$ mode excitation is assumed, the matrix LE and LH are the coupling matrices connecting the $TE_{i,j}^x$ modes in guide (1) to the $TE_{m,n}^x$ modes in guide (2). Since two indices for each mode in matrix notation are not appropriate, new indices k_I and k_{II} are defined and their sequences are based on the respective values of the propagation constant. Then the matrices LE and LH are connecting the $TE_{k_I}^x$ modes to the $TE_{k_{II}}^x$ modes.

Rearranging equations 3.2 and 3.7 yields the S-matrix of the discontinuity. Details of this procedure are given in Appendix A.

Instead of H_x, also H_y could be used for the second continuity equation (see figure 3.2):

$$H_y^{(2)} = H_y^{(1)} \qquad x \in [c_x, d_x] \quad y \in [c_y, d_y] \tag{3.8}$$

This equation leads to

$$A_{i,j}^{(1)} - B_{i,j}^{(1)} = \sum_{m=1}^{\infty} \sum_{n=o}^{\infty} \frac{4}{ab} \frac{(\frac{m\pi}{A})^2}{(\frac{i\pi}{a})^2} \frac{T_{m,n}^{(2)}}{T_{i,j}^{(1)}} I_{m,i} \frac{J_{n,j}}{\sqrt{1+\delta_{0,n}}\sqrt{1+\delta_{0,j}}} \left(A_{m,n}^{(2)} - B_{m,n}^{(2)}\right) \qquad (3.9)$$

which is linearly independent of equations 3.1 and 3.6. It is obvious that the system of equations (3.2, 3.7 and 3.9) has only two unknowns (namely $B^{(1)}$ and $A^{(2)}$). This overdeterminated system is due to the fact that the hypothesis is not correct: the component E_x is not zero. However, it has been shown in [28] that, if resonant effects do not occur within the discontinuity plane, the first higher mode containing an E_x component is strongly evanescent and its influence on the field matching is small or negligible. Therefore, it appears to be sufficient to analyze both types of discontinuities with a five-component field and by neglecting the H_y-matching equation.

To evaluate the error made by this approximation, a comparison of this method with a full wave analysis is presented in the next section.

3.2 Full wave analysis

The full wave approach is based on the superposition of two potential vectors $\Psi_x^{(h)}$ and $\Psi_x^{(e)}$ describing six field components according to:

$$\vec{E} = -j\omega\mu_0 \vec{\nabla} \times \vec{\Psi}_x^{(h)} + \vec{\nabla} \times \vec{\nabla} \times \vec{\Psi}_x^{(e)} \qquad (3.10)$$

$$\vec{H} = \vec{\nabla} \times \vec{\nabla} \times \vec{\Psi}_x^{(h)} + j\omega\varepsilon_0 \vec{\nabla} \times \vec{\Psi}_x^{(e)} \qquad (3.11)$$

Both potential vectors individually must satisfy the Helmholtz equation and the boundary conditions. The potential vectors are defined as an infinite sum of normal modes:

$$\Psi_{x\,m,n}^{(h)} = \sum_{m=1}^{\infty} \sum_{n=0}^{\infty} F_{m,n}^{(h)}(x,y) \left(A_{m,n} e^{-j\beta_{m,n} z} + B_{m,n} e^{j\beta_{m,n} z}\right) \qquad (3.12)$$

$$\Psi^{(e)}_{x\,p,q} = \sum_{p=0}^{\infty}\sum_{q=1}^{\infty} F^{(e)}_{p,q}(x,y)\left(C_{p,q}e^{-j\beta_{p,q}z} - D_{p,q}e^{j\beta_{p,q}z}\right) \tag{3.13}$$

where

$$F^{(h)}_{m,n}(x,y) = T^{(h)}_{m,n}\sin(k_{x_m}x)\cos(k_{y_n}y) \tag{3.14}$$

$$F^{(e)}_{p,q}(x,y) = T^{(e)}_{p,q}\cos(k_{x_p}x)\sin(k_{y_q}y) \tag{3.15}$$

with $k_{x_i} = i\pi/a$ and $k_{y_j} = j\pi/b$. The propagation constant is evaluated as:

$$\beta^2_{i,j} = k_0^2\varepsilon_r - k^2_{x_i} - k^2_{y_j} = k_0^2\varepsilon_r - (\frac{i\pi}{a})^2 - (\frac{j\pi}{b})^2$$

The expression for the fields derived from $\Psi^{(h)}_x$ has been given already in equations 2.6. The fields derived from the electric vector potential $\Psi^{(e)}_x$ are given as follows ($p = 0 \rightarrow \infty, q = 1 \rightarrow \infty$):

$$\begin{aligned}
E^{(e)}_x &= (k^2 - k^2_{x_p})T^{(e)}_{p,q}\cos(k_{x_p}x)\sin(k_{y_q}y)\left(C_{p,q}e^{-j\beta_{p,q}z} + D_{p,q}e^{j\beta_{p,q}z}\right)\\
E^{(e)}_y &= -T^{(e)}_{p,q}k_{x_p}k_{y_q}\sin(k_{x_p}x)\cos(k_{y_q}y)\left(C_{p,q}e^{-j\beta_{p,q}z} + D_{p,q}e^{j\beta_{p,q}z}\right)\\
E^{(e)}_z &= jT^{(e)}_{p,q}k_{x_p}\beta_{p,q}\sin(k_{x_p}x)\sin(k_{y_q}y)\left(C_{p,q}e^{-j\beta_{p,q}z} - D_{p,q}e^{j\beta_{p,q}z}\right)
\end{aligned} \tag{3.16}$$

$$\begin{aligned}
H^{(e)}_x &= 0\\
H^{(e)}_y &= \omega\varepsilon T^{(e)}_{p,q}\beta_{p,q}\cos(k_{x_p}x)\sin(k_{y_q}y)\left(C_{p,q}e^{-j\beta_{p,q}z} - D_{p,q}e^{j\beta_{p,q}z}\right)\\
H^{(e)}_z &= -j\omega\varepsilon T^{(e)}_{p,q}k_{y_q}\cos(k_{x_p}x)\cos(k_{y_q}y)\left(C_{p,q}e^{-j\beta_{p,q}z} + D_{p,q}e^{j\beta_{p,q}z}\right)
\end{aligned}$$

$T^{(e)}_{p,q}$ denotes the normalization factor of the amplitude coefficients which is calculated from equation 2.7:

$$T^{(e)}_{p,q} = \frac{2}{\sqrt{\omega\varepsilon\beta_{p,q}\left(k_0^2\varepsilon_r - (\frac{q\pi}{a})^2\right)ab}} \tag{3.17}$$

3.2.1 Matching equation

The electromagnetic field is given as an infinite sum of modal vectors. Applying the continuity conditions at the junction ($z = 0$) (see Fig. 3.2):

$$\begin{aligned} \vec{E}_T^{(2)} &= \vec{E}_T^{(1)} && x \in [c_x, d_x] \quad y \in [c_y, d_y] \\ &= 0 && \text{otherwise,} \end{aligned}$$

and using the property of mode orthogonality twice:

$$\int_{A_2} \vec{E}_T^{(2)}.(\vec{e}_z \times \vec{\nabla}_{xy} F_{i,j}^{(h2)}) dS = \int_{A_2} \vec{E}_T^{(1)}.(\vec{e}_z \times \vec{\nabla}_{xy} F_{i,j}^{(h2)}) dS \qquad (3.18)$$

$$\int_{A_1} \vec{E}_T^{(2)}.(\vec{e}_z \times \vec{\nabla}_{xy} F_{i,j}^{(e2)}) dS = \int_{A_1} \vec{E}_T^{(1)}.(\vec{e}_z \times \vec{\nabla}_{xy} F_{i,j}^{(e2)}) dS \qquad (3.19)$$

leads to two different coupling equations for the E-field. The second equation (3.19) which can be rewritten as

$$\int_0^A \int_0^B E_x^{(e2)} \frac{\partial F^{(e2)}}{\partial y} dS = \int_{c_x}^{d_x} \int_{c_y}^{d_y} E_x^{(e1)} \frac{\partial F^{(e2)}}{\partial y} dS \qquad (3.20)$$

yields the coupling equation between TM^x modes.

$$C^{(2)} + D^{(2)} = LH^{(3)} \left(C^{(1)} + D^{(1)} \right) \qquad (3.21)$$

where $LH^{(3)}$ is expressed as:

$$LH_{i,j}^{(3)} = \sum_{p=0}^{\infty} \sum_{q=1}^{\infty} \frac{\beta^{(1)\,2} + (q\pi/b)^2}{\beta^{(2)\,2} + (j\pi/B)^2} \frac{T_{p,q}^{(e1)}}{T_{i,j}^{(e2)}} \frac{4}{AB} \frac{I_{i,p}}{\sqrt{1 + \delta_{0,p}} \sqrt{1 + \delta_{0,i}}} J_{j,q} \qquad (3.22)$$

Equation 3.18 is more complex because it includes the coupling between the different TE^x modes but also the coupling between TE^x and TM^x modes. Rewriting (3.18) as:

$$\int_0^A \int_0^B \left(E_x^{(e2)} \frac{\partial F^{(h2)}}{\partial y} - E_y^{(e2)} \frac{\partial F^{(h2)}}{\partial x} \right) - E_y^{(h2)} \frac{\partial F^{(h2)}}{\partial x} dS =$$

$$\int_{c_x}^{d_x} \int_{c_y}^{d_y} \left(E_x^{(e1)} \frac{\partial F^{(h2)}}{\partial y} - E_y^{(e1)} \frac{\partial F^{(h2)}}{\partial x} \right) - E_y^{(h1)} \frac{\partial F^{(h2)}}{\partial x} dS \qquad (3.23)$$

and using again the orthogonality between modes, leaves on the LHS of (3.23) a diagonal matrix containing the amplitude coefficients and on the RHS, two coupling matrices $LH^{(1)}$ and $LH^{(2)}$. $LH^{(1)}$ was already defined in the TE^x approach because it represents the coupling between TE^x modes. $LH^{(2)}$ corresponds to the coupling between TE^x and TM^x modes at the discontinuity. Therefore, equation 3.23 can be written as:

$$A^{(2)} + B^{(2)} = LH^{(1)}\left(A^{(1)} + B^{(1)}\right) + LH^{(2)}\left(C^{(1)} + D^{(1)}\right) \tag{3.24}$$

where the $(i,j)^{th}$ element of $LH^{(2)}$ has the following form:

$$\begin{aligned} LH^{(2)}_{i,j} &= \sum_{p=0}^{\infty}\sum_{q=1}^{\infty} -\frac{\beta^{(1)\,2}_{q,p} + (\frac{q\pi}{b})^2}{\beta^{(2)\,2}_{i,j} + (\frac{j\pi}{B})^2}\frac{T^{(e1)}_{p,q}}{T^{(h2)}_{i,j}}\frac{4\frac{i\pi}{A}\frac{j\pi}{B}}{\omega\mu_0 AB\beta^{(2)}_{i,j}}\frac{I_{i,p}}{\sqrt{1+\delta_{0,p}}}\frac{J_{j,q}}{\sqrt{1+\delta_{0,j}}} \\ &\quad + \frac{T^{(e1)}_{p,q}}{T^{(h2)}_{i,j}}\frac{4\frac{p\pi}{a}\frac{q\pi}{b}}{\omega\mu_0 AB\beta^{(2)}_{i,j}}\frac{I_{i,p}}{\sqrt{1+\delta_{0,p}}}\frac{J_{j,q}}{\sqrt{1+\delta_{0,j}}} \end{aligned} \tag{3.25}$$

With (3.21) and (3.24), a set of two equations has been obtained. By matching the H-field, a second set of equations is obtained involving three coupling matrices $LE^{(1)}$, $LE^{(2)}$ and $LE^{(3)}$ which are the transposed of $LH^{(1)}$, $LH^{(2)}$ and $LH^{(3)}$.

$$A^{(1)} - B^{(1)} = LE^{(1)}\left(A^{(2)} - B^{(2)}\right) \tag{3.26}$$

$$C^{(1)} - D^{(1)} = LE^{(2)}\left(A^{(2)} - B^{(2)}\right) + LE^{(3)}\left(C^{(2)} - D^{(2)}\right) \tag{3.27}$$

Equations (3.21), (3.24), (3.26) and (3.27) lead to the following matrix equation (where 0 denotes the null matrix and U the unit matrix) :

$$\underbrace{\begin{pmatrix} U & 0 & LE^{(1)} & 0 \\ 0 & U & LE^{(2)} & LE^{(3)} \\ -LH^{(1)} & -LH^{(2)} & U & 0 \\ 0 & -LH^{(3)} & 0 & U \end{pmatrix}}_{K_1}\begin{pmatrix} B^{(1)} \\ D^{(1)} \\ A^{(2)} \\ C^{(2)} \end{pmatrix} =$$

$$\underbrace{\begin{pmatrix} U & 0 & LE^{(1)} & 0 \\ 0 & U & LE^{(2)} & LE^{(3)} \\ LH^{(1)} & LH^{(2)} & -U & 0 \\ 0 & LH^{(3)} & 0 & -U \end{pmatrix}}_{K_2} \begin{pmatrix} A^{(1)} \\ C^{(1)} \\ B^{(2)} \\ D^{(2)} \end{pmatrix} \tag{3.28}$$

The scattering matrix of the step discontinuity is then given by:

$$S = \begin{pmatrix} S_{11} & S_{12} \\ S_{21} & S_{22} \end{pmatrix} = K_1^{-1}.K_2 \tag{3.29}$$

3.2.2 Comparison of both approaches

In many applications, using a five-component field and neglecting the H_y-matching condition does not lead to wrong results. In other cases, this approximation is not valid and the discrepancy with the full wave approach becomes significant.

To illustrate this situation, the following cases are considered. The first case is a Ku-to-X-band transformer. The linear double taper is approximated by 24 steps of equal length. Both approaches lead to identical results (Fig. 3.3) and a comparison with measurements [33] shows excellent agreement. However, the TE^x-approach has a computational advantage because it requires only 30 percent of the CPU time needed for the full wave approach.

The second case to be analyzed is a Ku-band waveguide iris filter where the irises act as coupling elements between cavities. The transmission behavior is shown in figure 3.4. Both approaches investigated yield identical results. In the same graph, a convergence analysis of the filter is presented. It shows that a minimum of 40 TE^x modes are necessary to reach a satisfactory convergence.

In the case where the iris filter utilizes the resonance of the iris itself rather than the resonant effect due to the waveguide section between irises, some important discrepan-

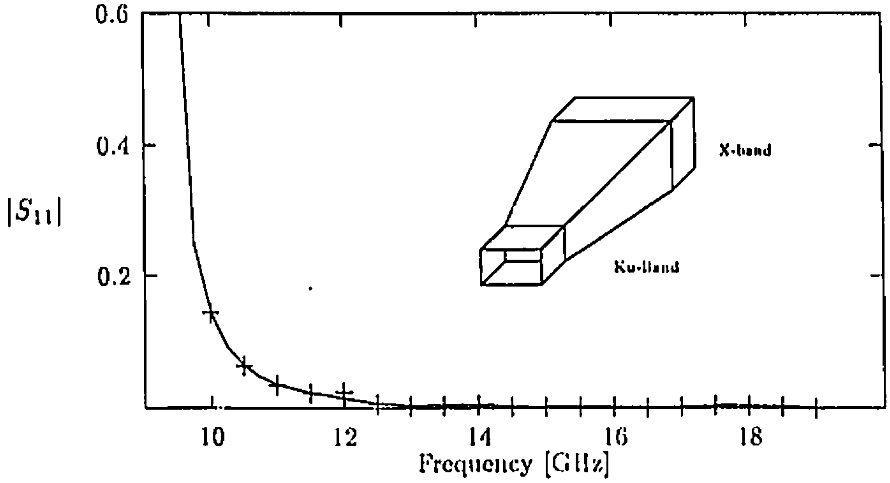

Figure 3.3: Magnitude of the reflection coefficient of a linear Ku-to-X-band transformer (approximated by 24 steps), +++ measured [33].

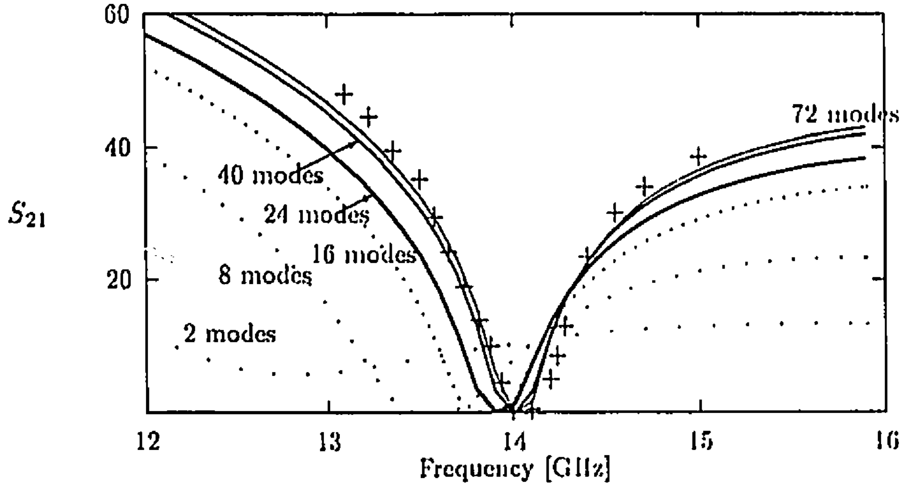

Figure 3.4: Insertion loss of a three-resonator iris-coupled Ku-band waveguide filter, +++ measured [29].

cies may occur, in particular at frequency close to the iris resonance. For example, the iris shown in figure 3.6, has a cutoff frequency at 37.5 GHz. Exactly at this frequency, the TE^x approach reveals some instabilities due to the lack of the H_y field matching. The peak at 42.2 GHz corresponds-to the zero of the LE-denominator (equation 3.6) because the factor $T_{i,j}^{(1)}$ which is proportional to:

$$\frac{1}{\beta_{i,j}^{(1)} + \left(\frac{j\pi}{b}\right)^2}$$

becomes infinite at this frequency for $i = 2$. That explains the large discrepancies with the full-wave analysis for frequencies within the band [37.5 GHz, 42.2 GHz]. This discrepancy vanishes when the frequency gets further away from this band. Figure 3.6 is a different view of the performance of the same iris but as a function of the frequency. Again, the figure shows an important discrepancy around the cutoff frequency (37.5 GHz) and, wrong results are obtained by using only a TE^x approach.

3.3 Alternative approach

An interesting solution was proposed in [28]. In this approach, the method based on five field components alternates between the H_x- and H_y-field matching at the discontinuity. The S-matrix is obtained from two coupling matrices LH and LE. LH is derived from the E_y-matching equation and its expression can be found using equation 3.1. The H_x- and H_y-matching conditions, equations (3.5) and (3.8), lead to two different coupling matrices LE_x and LE_y. A new matrix LE is formed by copying elements from either LE_x or LE_y into LE where:

$$\begin{array}{lcll} (LE)_{k_I k_{II}} & = & (LE_x)_{k_I k_{II}} & \text{if mode } k_I \text{ or mode } k_{II} \text{ is a } TE^x_{m0} \text{ type} \\ (LE)_{k_I k_{II}} & = & (LE_y)_{k_I k_{II}} & \text{if neither mode } k_I \text{ nor mode } k_{II} \text{ are a } TE^x_{m0} \text{ type} \end{array} \qquad (3.30)$$

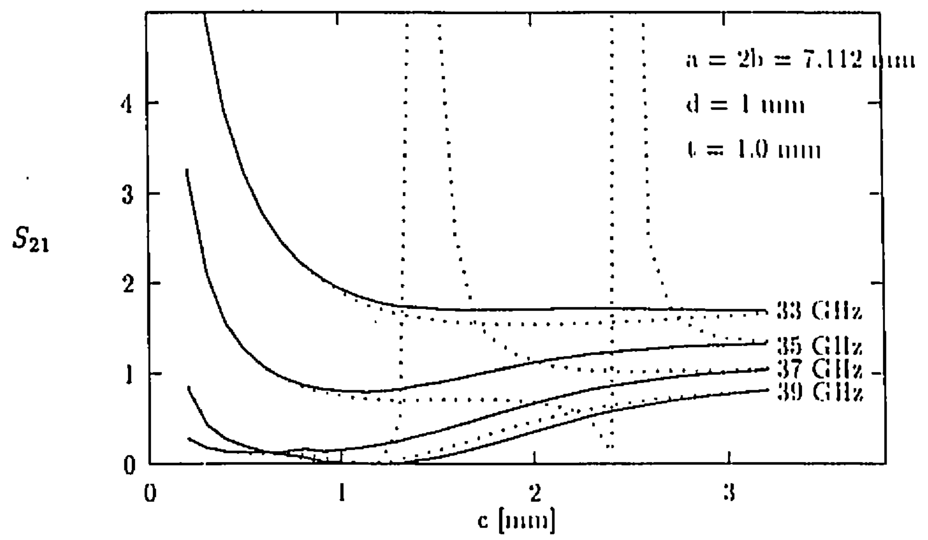

Figure 3.5: Insertion loss of a single resonant iris in a Ka-band waveguide.

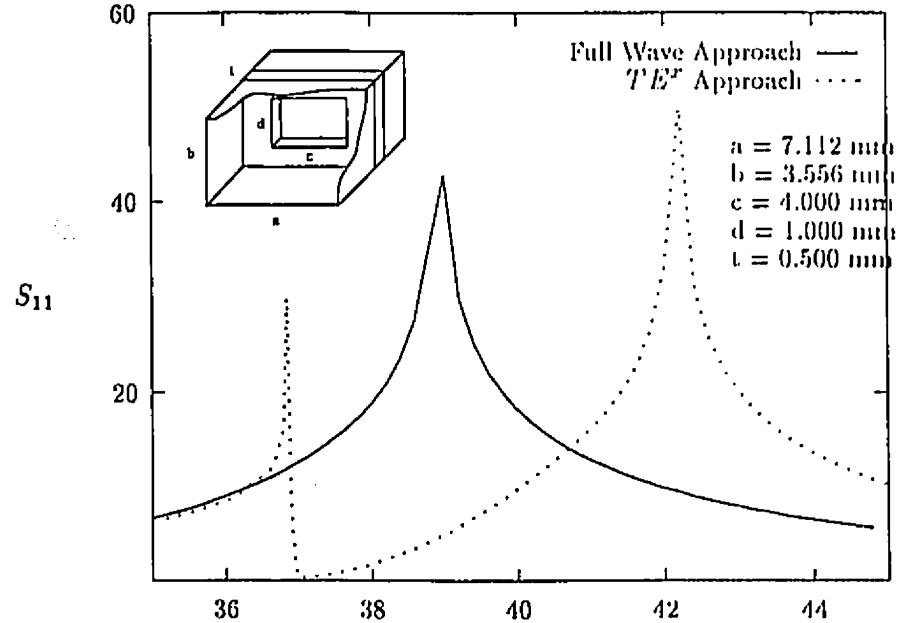

Figure 3.6: Return loss of a resonant iris in a Ka-band waveguide.

Therefore, LE contains data which is derived from the matching conditions of either H_x or H_y. Using the procedure in Appendix A leads to the S-matrix of the discontinuity.

This method requires the same CPU time as the TE^x approach and, according to [28], leads to very satisfactory results in particular in the case of a resonant iris.

3.4 Application to power divider and quadriplexer

The design of an 6-dB power divider can be done by cascading step discontinuities and a 2x2 grid-divider. The overall five-port scattering matrix is calculated by using the generalized scattering matrix techniques [31]. Fig. 3.7 shows the frequency response over 10 GHz bandwidth of an optimized W-band 6-dB power divider. The data for the power divider is given in Table 3.1. It should be noticed that the lengths of each transformer section are close to $\lambda_g/4$ (at 90 GHz) and decrease from 2.58mm in the first section to 1.92 mm in the last section of the taper. However, the 4^{th} length does not approximate $\lambda_g/4$ because it is located just between the two biggest steps of the taper, 3.84 → 5.18 mm in x-direction and 1.81 → 2.31 mm in y-direction. Therefore, higher order modes are more excited between both steps and the length L_4 must be longer to reduce their parasitic effect.

The insertion loss remains virtually constant at 6.023 dB[1]. Furthermore, different S_{11}-responses according to the number of modes are displayed in the same figure as well. They indicate that, for example, 30 modes are "almost" sufficient to obtain good behavior of the return loss coefficient.

The quadriplexer (figure 3.1) is a 6-dB power divider parallel connected to four E-plane metal insert filters. To match the field at the power divider output and the filter

---

[1] The return loss is greater than 30 dB over the same range

Power divider (all dimensions in millimeters)				
	a_i	b_i	L_i	$\lambda_g/4$ at 90 GHz
Input waveguide	2.54	1.27		2.209
1^{st} section	2.67	1.33	2.58	2.133
2^{nd} section	2.74	1.48	2.52	2.100
3^{rd} section	3.50	1.81	2.32	1.895
4^{th} section	3.84	2.31	3.10	1.850
5^{th} section	5.18	2.64	1.92	1.760

Quadriplexer (all dimensions in millimeters)					
	a_i	b_i	L_i	d_i	
Input waveguide	2.540	1.270		d_1	1.89
1^{st} section	4.921	1.408	1.35	d_2	2.07
2^{nd} section	5.283	1.601	0.80	d_3	1.84
3^{rd} section	3.001	0.828	1.00	d_4	1.83
4^{th} section	4.435	2.589	2.10		
5^{th} section	5.180	2.640	1.10		

Table 3.1: Mechanical dimensions of the W-band 4-way power divider and quadriplexer.

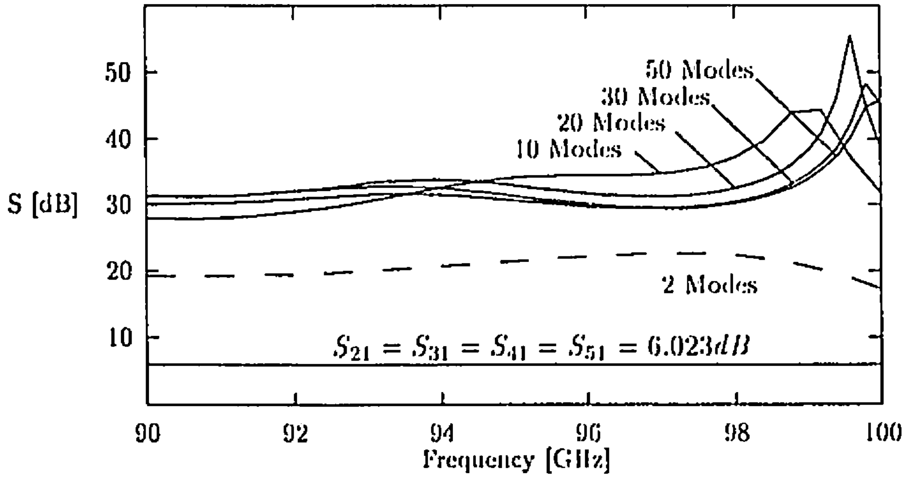

Figure 3.7: Frequency response of an optimized 4-channel power divider.

inputs, the technique used in section 2.6.1 which consists of sorting the $TE^x_{n,m}$ modes in order to keep only those which match the filter $TE^x_{i,0}$ modes, is applied.

Fig. 3.8 illustrates an optimized quadriplexer in the W-band. Note that the third step in the taper is negative creating an inductive effect. This means also that the taper is not an approximation of a smooth tapered transition.

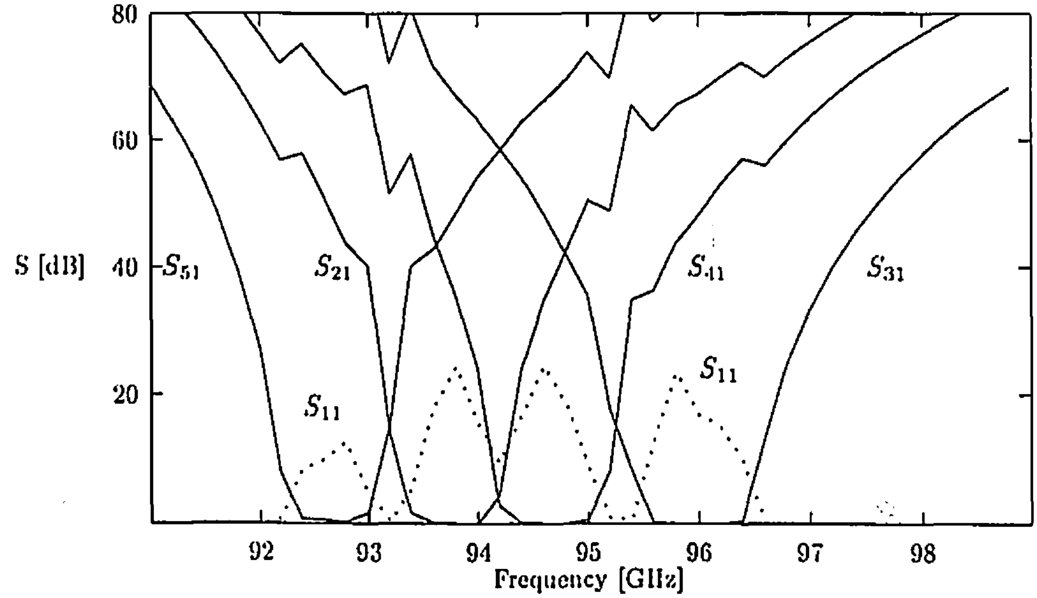

Figure 3.8: Frequency response of an optimized quadriplexer.

Chapter 4

Coaxial circular waveguide

Although attenuation of coaxial lines increases significantly with frequency [35] and can reach 2 dB per foot at 60 GHz, coaxial systems are now used up to this frequency and are planned to go as high as 100 GHz. For this purpose, 1mm connectors are being developed. Accurate design of miniaturized coax components is not possible anymore by considering only the TEM mode, in particular in view of the fact that for fabrication purposes, some sections of the coaxial device may have large dimensions in which TE_{11} or even other higher modes can propagate. In this chapter, the MMM is applied to analyze discontinuities such as the coaxial inner or outer step (including a change in supporting dielectric) and abruptly ended rods (see Figure 4.1).

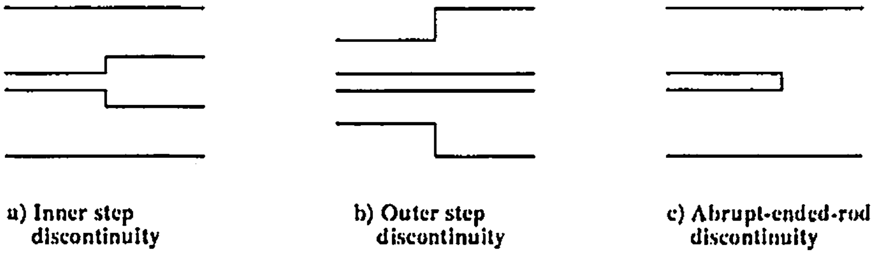

Figure 4.1: Types of coaxial discontinuities.

4.1 Vector potential

The general analysis of coaxial circular waveguide includes TE, TM and TEM modes. It starts from the following equations (equivalent to equations 3.10 and 3.11):

$$\vec{E} = -\vec{\nabla} \times \vec{\Psi}^{(h)} + \frac{1}{j\omega\varepsilon} \vec{\nabla} \times \vec{\nabla} \times \vec{\Psi}^{(e)} \qquad (4.1)$$

$$\vec{H} = \vec{\nabla} \times \vec{\Psi}^{(e)} + \frac{1}{j\omega\mu} \vec{\nabla} \times \vec{\nabla} \times \vec{\Psi}^{(h)} \qquad (4.2)$$

where $\vec{\Psi}^{(e)}$ is the TE vector potential and $\vec{\Psi}^{(h)}$ is the TM vector potential. The TEM mode is only a special case of the TM mode. These equations lead to an expression for the six field components, with $E_z = 0$ for the TE mode, $H_z = 0$ for the TM mode and both being zero for the TEM mode. See Appendix C for a complete description of the field components.

The following analysis is based on two assumptions: First, none of the structures analyzed in this chapter contains a discontinuity in θ-direction and secondly the incident wave is TEM. Therefore, as shown in Figure 4.2, three field components (E_ρ, H_θ and E_z) are sufficient to describe the field at any points of the discontinuities and, thereby, only TEM and TM modes are excited at the discontinuity.

For the TM mode, in a cylindrical coordinate system, the Helmholtz equation can be written as:

$$\frac{1}{\rho}\frac{\partial}{\partial\rho}\left(\rho\frac{\partial\Psi^{(h)}}{\partial\rho}\right) + \frac{1}{\rho^2}\frac{\partial^2\Psi^{(h)}}{\partial\theta^2} + \frac{\partial^2\Psi^{(h)}}{\partial z^2} + k^2\Psi^{(h)} = 0 \qquad (4.3)$$

where $k^2 = k_0^2\varepsilon_r$.

Using the method of separation of variables, e.g. writing $\Psi^{(h)}$ as $\Psi^{(h)}(\rho,\theta,z) = R(\rho).\Phi(\theta).Z(z)$, yields three equations:

$$\frac{d^2Z(z)}{dz^2} + k_z^2 Z(z) = 0 \qquad (4.4)$$

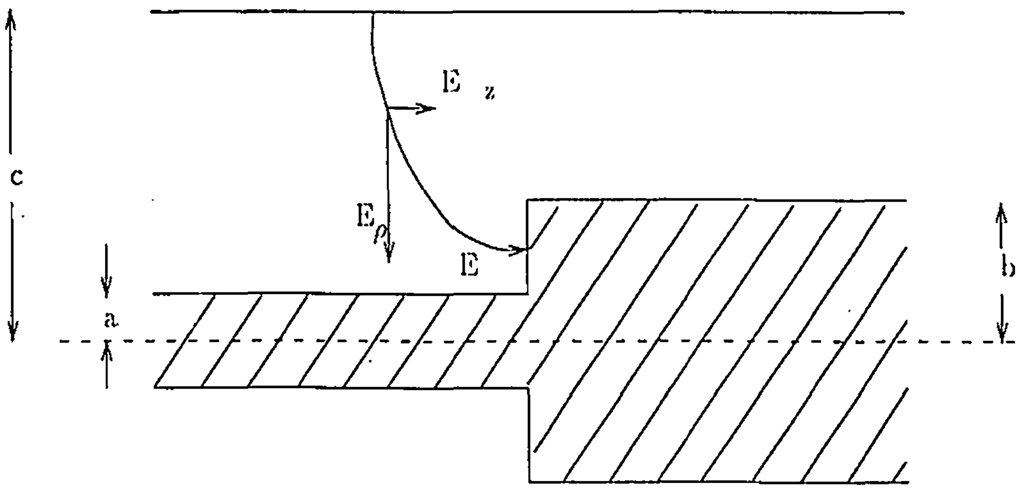

Figure 4.2: E-field decomposition of an inner step discontinuity.

$$\frac{d^2\Phi(\theta)}{d\theta^2} + n^2\Phi(\theta) = 0 \qquad (4.5)$$

$$\rho^2\frac{d^2R(\rho)}{d\rho^2} + \rho\frac{dR(\rho)}{d\rho} + \left((k_\rho\rho)^2 - n^2\right)R(\rho) = 0 \qquad (4.6)$$

with $k_\rho^2 + k_z^2 = k^2$. Assuming wave propagation in z-direction, equation 4.4 yields:

$$Z(z) = e^{jk_z z} \qquad (4.7)$$

where k_z (or β) is the propagation constant.

Equation (4.6) is a Bessel differential equation of order n. R is determined by considering the boundary conditions. For a coaxial line, these conditions are (Fig. 4.3):

$$E_z = 0 \quad \text{at} \quad \rho = a \quad \text{and} \quad \rho = b \qquad (4.8)$$

Since the E_z component is proportional to Ψ, the potential vector satisfies also those conditions and, therefore, the function R. Both conditions can not be satisfied with a

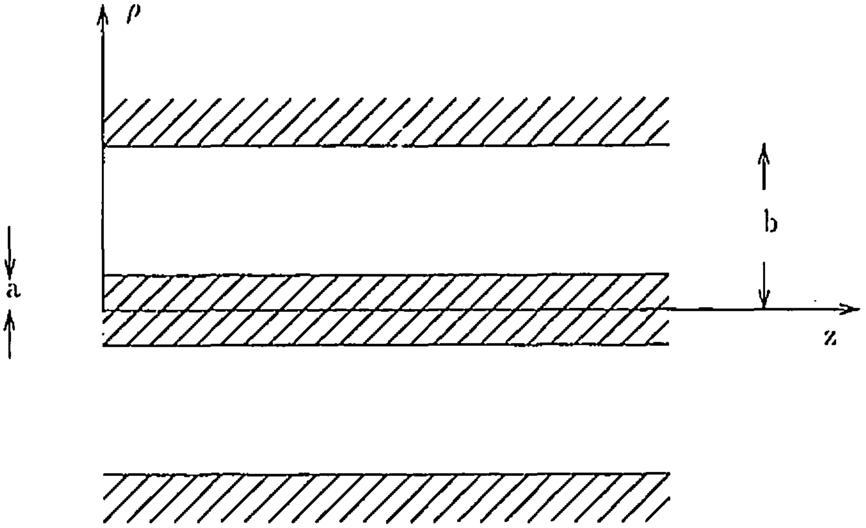

Figure 4.3: Side view of a coax cable.

single function like in an empty circular waveguide where J_n (Bessel function of the first kind) is sufficient. A general form consisting of a sum of independent solutions (J_n and N_n, Bessel functions of the first and second kind, respectively) is necessary.

$$R(\rho) = B_n(k_\rho \rho) = A N_n(k_\rho \rho) + C J_n(k_\rho \rho) \tag{4.9}$$

The boundary conditions are transformed into:

$$N_n(k_\rho b) J_n(k_\rho a) - N_n(k_\rho a) J_n(k_\rho b) = 0 \tag{4.10}$$

The propagation constant of the $TM_{n,m}$ mode is calculated from the m^{th} root of the n^{th} boundary equation. As an example, Figure 4.4 displays the function $B_0(k_{\rho_{0,m}}\rho)$ for different values of m. All these different functions have a zero at $\rho = a = 4\ mm$ and at $\rho = b = 14\ mm$.

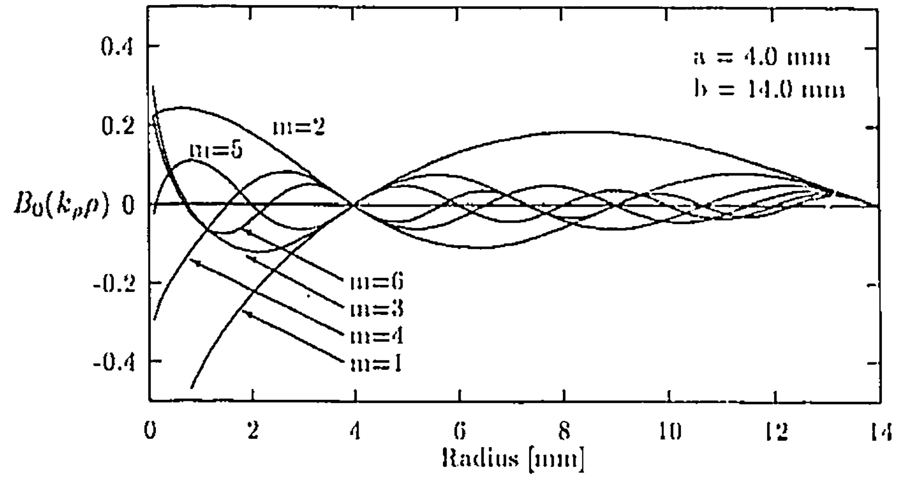

Figure 4.4: Bessel function $B_0(k_{\rho 0,m}\rho)$.

Finally, since $\Phi(\theta)$ is 2π-periodical, the following relation must hold:

$$\Phi(\theta) = \Phi(\theta + 2\pi) \tag{4.11}$$

In other words, Φ has to be periodic in θ which requires that n be an integer. Then $\Phi(\theta) = \sin(n\theta)$ or $\cos(n\theta)$. However, the complete absence of E_θ and H_ρ implies that n must be zero. Therefore, only TEM and $TM_{0,m}$ modes will be present at the discontinuity. Hence, the potential can be rewritten as:

$$\Psi^{(h)}(\rho,\theta,z) = B_0(k_{\rho 0,m}\rho).e^{jk_z z}$$

with two possible and equivalent ρ-functions:

$$B_0(k_{\rho 0,m}\rho) = N_0(k_\rho a)J_0(k_\rho\rho) - J_0(k_\rho a)N_0(k_\rho\rho) \tag{4.12}$$

or

$$B_0(k_{\rho 0,m}\rho) = N_0(k_\rho b)J_0(k_\rho \rho) - J_0(k_\rho b)N_0(k_\rho \rho) \tag{4.13}$$

The choice of B_0 will depend on the type of discontinuity under analysis.

The TEM mode expression is obtained by setting $k_\rho = 0$ (e.g. $m = 0$) in equation 4.6. A solution to this equation satisfying the boundary condition exists only if $n = 0$. Therefore:

$$R(\rho) = A\ln(\rho) \tag{4.14}$$

The electric field can be written as the sum of modes:

$$\begin{aligned} E_\rho &= -\frac{1}{\omega\varepsilon}\alpha_0\frac{\beta_0 T_0}{\rho}\left(A_0 e^{-j\beta_0 z} + B_0 e^{j\beta_0 z}\right) \\ &- \frac{1}{\omega\varepsilon}\sum_{m=1}^{\infty}\alpha_m\beta_m T_m B_0'(k_m\rho)\left(A_m e^{-j\beta_m z} + B_m e^{j\beta_m z}\right) \end{aligned} \tag{4.15}$$

where B_0' is the derivative of B_0 defined in equations 4.12 and 4.13. It can been shown, using integral properties of Bessel functions [37], that all modes are orthogonal. The normalization has been obtained by multiplying each mode by α. α is computed by solving the following integral:

$$\int_a^b e_m^2(\rho)w(\rho)d\rho = Ct \qquad \forall m \tag{4.16}$$

where $w(\rho)$ is the weighting function ($w(\rho) = \rho$ in cylindrical coordinates system), the e_m are the eigenfunctions. The arbitrary constant Ct is set to 1. This yields:

$$\alpha_m = \frac{\sqrt{2}}{k_{\rho 0,m}}\cdot\left[b^2 B_1^2(k_{\rho 0,m}b) - a^2 B_1^2(k_{\rho 0,m}a)\right]^{-1/2} \quad \forall m \geq 1 \tag{4.17}$$

$$\alpha_0 = \frac{1}{\sqrt{\ln(b/a)}} \tag{4.18}$$

4.2 Inner step

For the theoretical analysis, an outer step is exactly equivalent to that of an inner step, therefore this section deals only with the last one. In the following, a TEM excitation is assumed generating only TM modes, as it was shown in section 4.1. The continuity conditions at the junction (at $z = 0$) (Fig. 4.2) yields for the E-field :

$$\begin{aligned} E_\rho^{(1)} &= E_\rho^{(2)} \quad \rho \in [b, c] \\ &= 0 \quad \rho \in [a, b] \end{aligned}$$

and for the H-field

$$H_\theta^{(1)} = H_\theta^{(2)} \quad \rho \in [b, c]$$

Separating the TEM and TM modes by using the property of mode orthogonality defined in the preceding section (including the multiplication by the weighting functions) and integrating within the appropriate boundaries, leads to the following equations:

1) for the TM mode (e.g. $i > 0$):

$$\begin{aligned} A_i^{(1)} + B_i^{(1)} &= -\frac{\varepsilon_r^{(1)}}{\varepsilon_r^{(2)}} \alpha_0^{(2)} \alpha_i^{(1)} B_0(k_i^{(1)}\rho) \frac{\beta_0^{(2)} T_0^{(2)}}{\beta_i^{(1)} T_i^{(1)}} \left(A_0^{(2)} + B_0^{(2)} \right) \\ &+ \sum_{q=1}^{\infty} \frac{\varepsilon_r^{(1)}}{\varepsilon_r^{(2)}} \frac{\beta_q^{(2)} T_q^{(2)}}{\beta_i^{(1)} T_i^{(1)}} b k_q^{(2)} k_i^{(1)2} \alpha_q^{(2)} \alpha_i^{(1)} \left(\frac{B_1(k_q^{(2)} b) B_0(k_i^{(1)} b)}{k_i^{(1)2} - k_q^{(2)2}} \right) \left(A_q^{(2)} + B_q^{(2)} \right) \end{aligned} \tag{4.19}$$

2) for the TEM mode:

$$A_0^{(1)} + B_0^{(1)} = \frac{\varepsilon_r^{(1)} \alpha_0^{(1)} T_0^{(2)} \beta_0^{(2)}}{\varepsilon_r^{(2)} \alpha_0^{(2)} T_0^{(1)} \beta_0^{(1)}} \left(A_0^{(2)} + B_0^{(2)} \right) \tag{4.20}$$

Equations (4.19) and (4.20) can be rewritten in matrix form:

$$A^{(1)} + B^{(1)} = LH \left(A^{(2)} + B^{(2)} \right) \tag{4.21}$$

For the H_θ matching condition, the final equation can be deduced by simply transposing the matrix LH ($LE = LH^t$). Then using the same procedure defined in Appendix A yields the scattering matrix of the discontinuity.

4.3 Results

4.3.1 Convergence analysis

The first investigation concerns the convergence rate with the radius as parameter which is shown in Figure 4.5. When the largest outer diameter increases, the number of modes needed to obtain good convergence behavior increases. Figure 4.6 illustrates the return loss as a function of the number of modes with the frequency as parameter. The starting point for all curves is the same because the TEM mode alone is independent of the frequency. A large number of modes (for example 15 modes at 50 GHz) is necessary at high frequencies to obtain good convergence behavior. This effect is expected because the higher the frequency, the more modes can propagate or approach their cutoff frequency.

4.3.2 Step discontinuities

One of the first papers dealing with step discontinuities was published by Somlo [45] in 1967 based on research carried out in 1944 ([41], [42]). He found that the equivalent capacitance of a step discontinuity can be expressed as:

$$C_d = \frac{\varepsilon}{100\pi}\left(\frac{\alpha^2+1}{\alpha}\ln\frac{\alpha^+}{\alpha^-} - 2\ln\frac{4\alpha}{\alpha^-\alpha^+}\right) + 1.11\ 10^{-15}(\alpha^-)(\tau-1) \tag{4.22}$$

for the inner step discontinuity and as

$$C_d = \frac{\varepsilon}{100\pi}\left(\frac{\alpha^2+1}{\alpha}\ln\frac{\alpha^+}{\alpha^-} - 2\ln\frac{4\alpha}{\alpha^-\alpha^+}\right) + 4.12\ 10^{-15}(0.8-\alpha)(\tau-1.4) \tag{4.23}$$

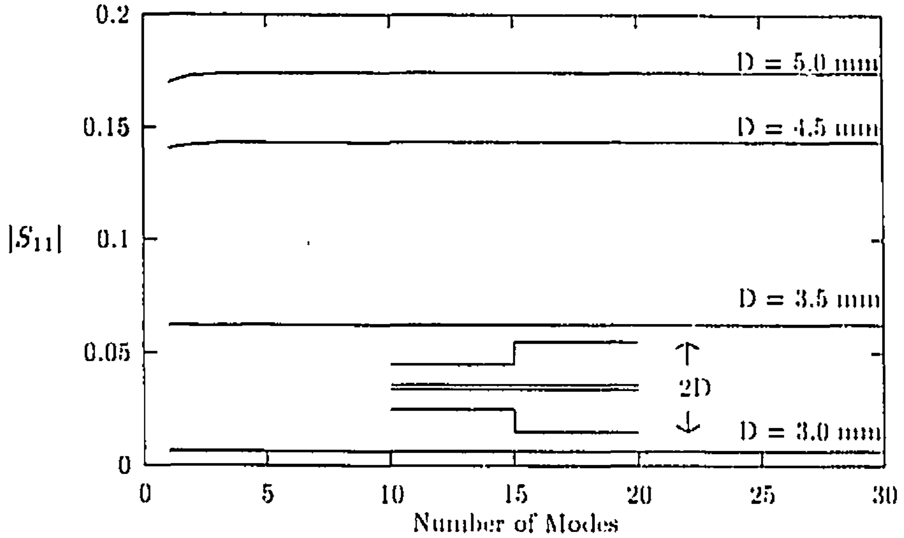

Figure 4.5: Convergence analysis

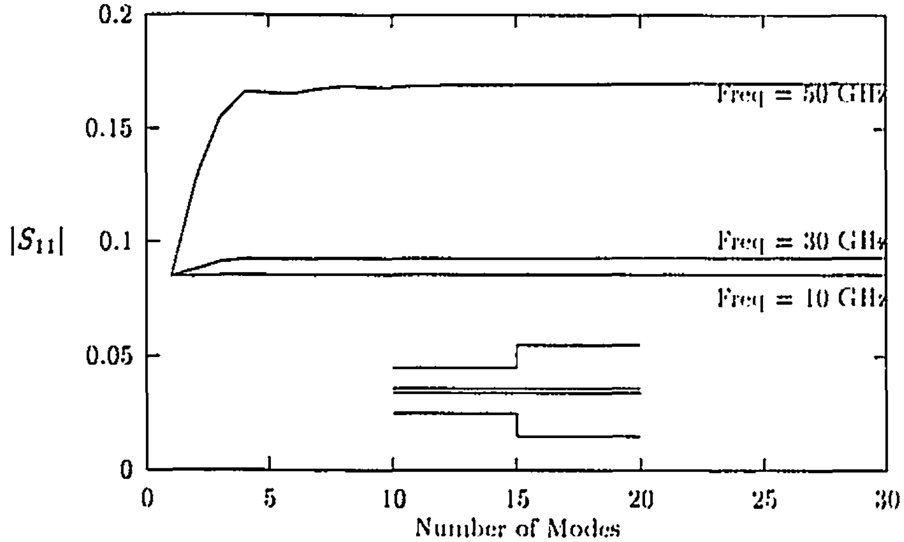

Figure 4.6: Convergence analysis

for the outer step discontinuity with $\alpha = (c-b)/(c-a)$, $\alpha^+ = 1+\alpha$, $\alpha^- = 1-\alpha$ and $\tau = c/a$. Somlo presented also a graph for a frequency correction factor. Figure 4.7 compares results computed from equation (4.23) with those based on the MMM. The figure includes the correction factor which has been found to be equal to 1.02 at 10 GHz, 1.56 at 30 GHz and impossible to determine at 50 GHz. As Figure 4.7 demonstrates, for frequencies higher than 30 GHz, Somlo's approach does not provide accurate results.

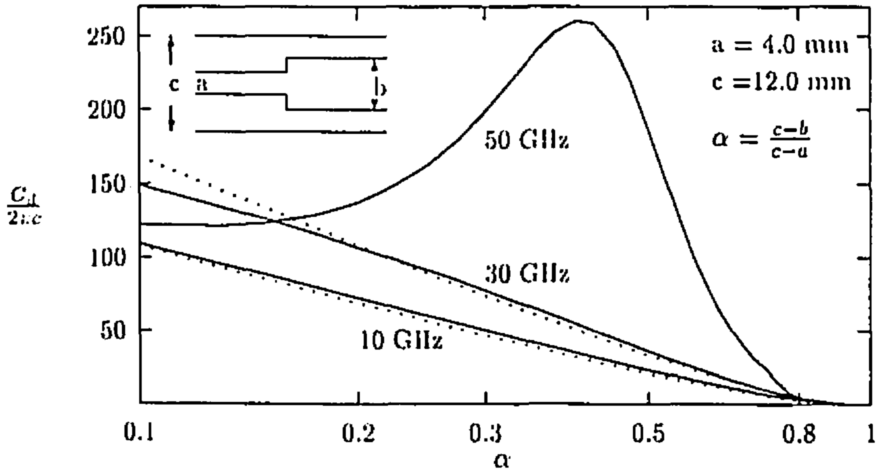

Figure 4.7: Coaxial line step capacitance (in fF/cm), for a step in the inner conductor. Dotted line from [45] (including the corrective factor).

More recently, other papers have dealt with coaxial discontinuities (Gwarek [43] and [44]). Gwarek presents the analysis of axially symmetric coaxial discontinuities using the Finite Difference Time Domain (FDTD) method. A comparison was made only for the 7 mm, 50 Ω, dielectric supported APC7-N adapter. Figure 4.8 shows the return loss of such adapter computed with the MMM and the FDTD. The agreement is better at low frequencies which could be an indication that the mesh size in the FDTD is too coarse at high frequencies.

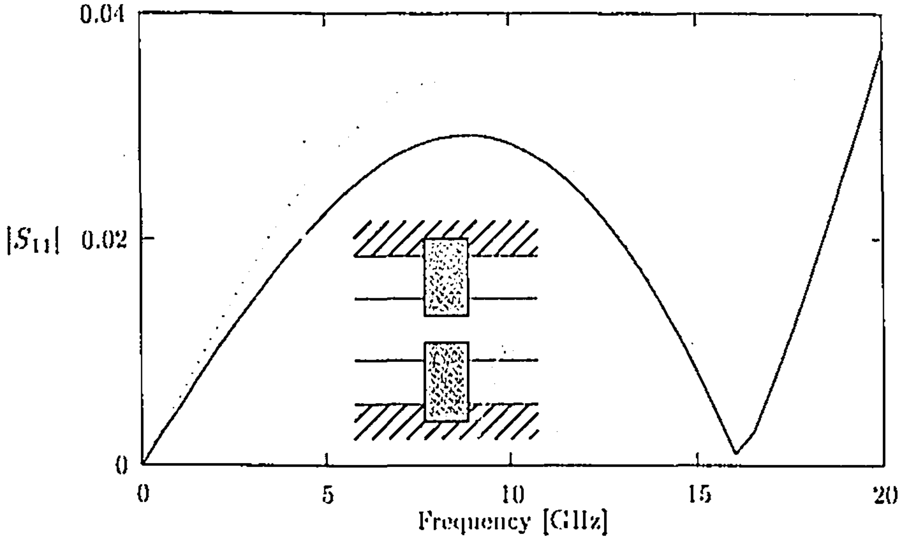

Figure 4.8: Absolute value of the reflection coefficient versus frequency for a line with a dielectrically supported (polysteren) center conductor. Dotted line from [43]

4.3.3 Very low-return-loss adapter

The design and optimization of a very low return loss taper from V- to K-cable using the MMM will be shown next. Using an optimization routine[1], the step discontinuities have been alternated in order to maintain the impedance as close as possible to the input impedance (50 Ω). The optimized adapter is shown in Figure 4.9. For comparison, an optimized adapter without alternating steps is presented as well.

---

[1] A multi dimensional search method or univariate search method [61]

section	1	2	3	4	5
Length [mm]	0.2325	0.8350	0.4825	0.6725	0.2575
Outer radius [mm]	0.8865	0.8865	1.0361	1.0361	1.1996
Inner radius [mm]	0.2540	0.3113	0.3113	0.3657	0.3657
Impedance [Ω]	57.7	48.3	55.5	48.1	54.9

Table 4.1: Data for an optimized low-return-loss adapter.

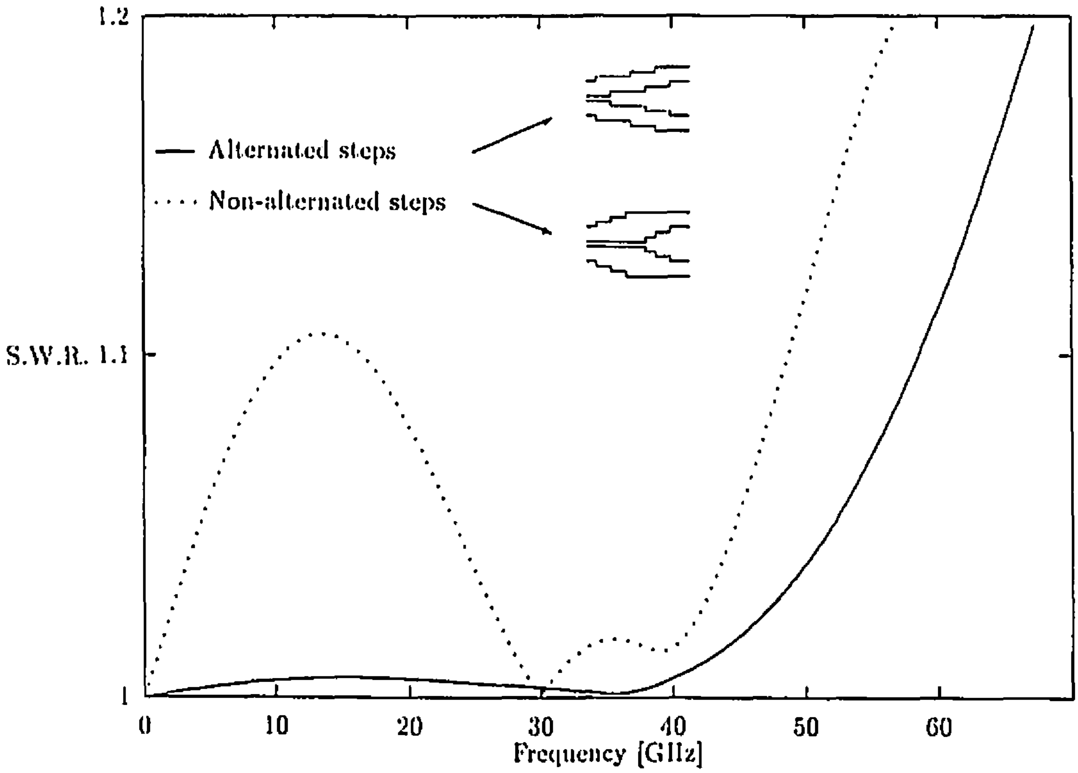

Figure 4.9: SWR of an optimized V- to K-cable taper. Dimensions in Table 4.1. Maximum SWR: 1.0058 at 15.5 *GHz* (dotted line: optimized non-alternated taper)

4.3.4 Coaxial filters

Coaxial filters are important components in coaxial systems. A low-pass filter is computed, cascading several discontinuities of high and low impedance sections (10Ω and 150Ω) with a dielectric ring to support the structure mechanically. The filter was originally designed on the basis of equivalent network theory [38]. A comparison between the measured filter response and the simulation with the MMM, using 10 modes, shows perfect agreement (see Figures 4.10 and 4.11).

A 700 MHz low-pass filter and a 3 GHz 23-section low-pass filter have been analyzed as well. The simulated V.S.W.R response of the first filter has been compared with [48] and the second one with [47]. In both cases, the good agreement is illustrated in Figures 4.12 and 4.13.

Finally, the last filter to be analyzed is a three-cavity bandpass filter operating in Ka-band at 37-38 GHz (see Table 4.2 for dimensions). The structure is initially designed from an equivalent circuit prototype based on a Tschebyscheff analysis and then optimized taking the effect of higher order modes into account (Fig. 4.14). The filter shows the following properties: insertion loss in the passband is less than 0.4 dB, the lower stopband is more than 20 GHz and an upper guard band more than 30 GHz (Fig. 4.15). However, a low frequency passband (0-10GHz) can not be suppressed for this kind of filter structure since it is a perfect D.C. transmission line. Since this may cause problems in certain applications, the next section presents a bandpass filter structure which eliminates this lower passband.

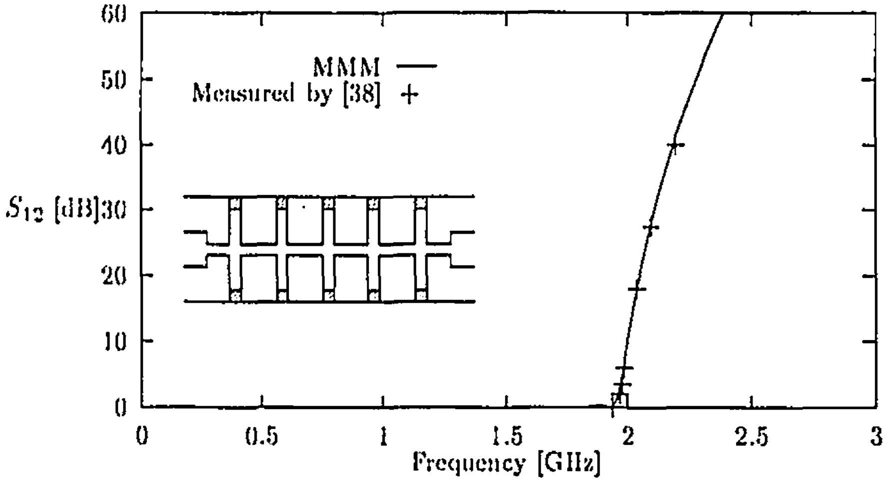

Figure 4.10: Comparison of a 2 GHz low-pass coaxial filter.

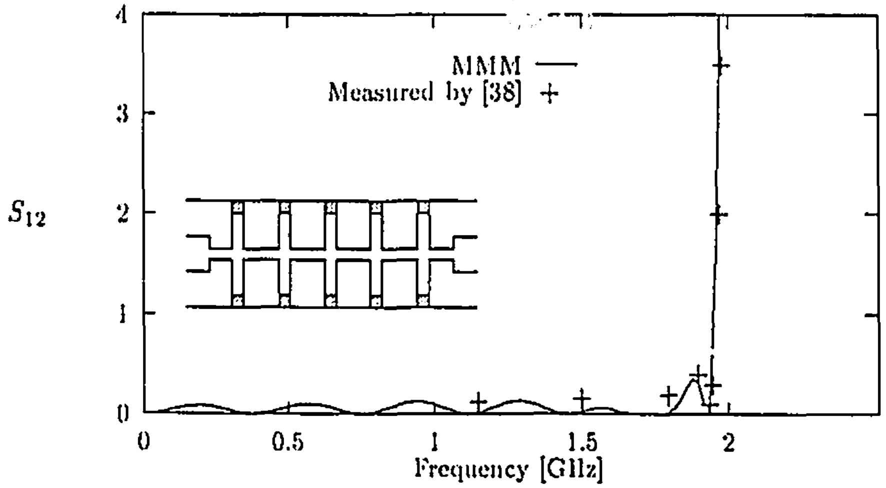

Figure 4.11: Expanded view of the 2 GHz low-pass coaxial filter.

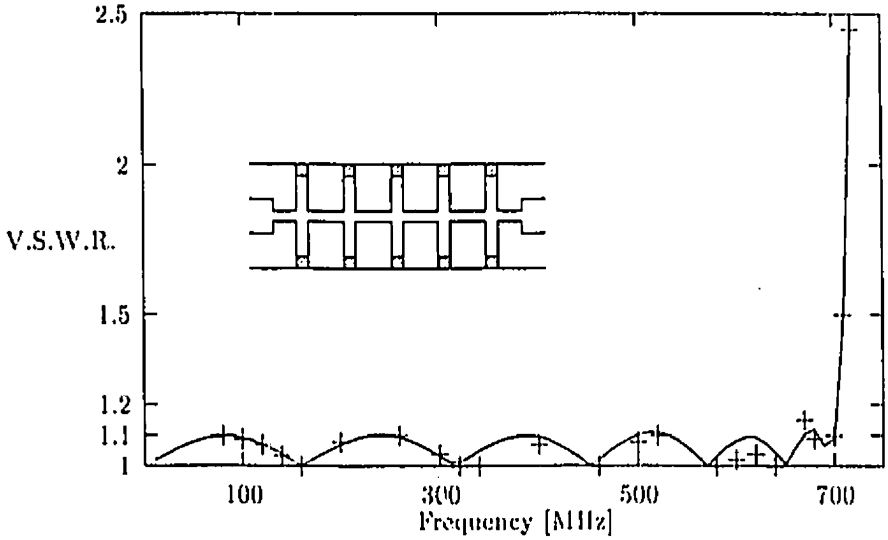

Figure 4.12: Comparison of a 700 MHz low-pass coaxial filter, +++ measured by [48].

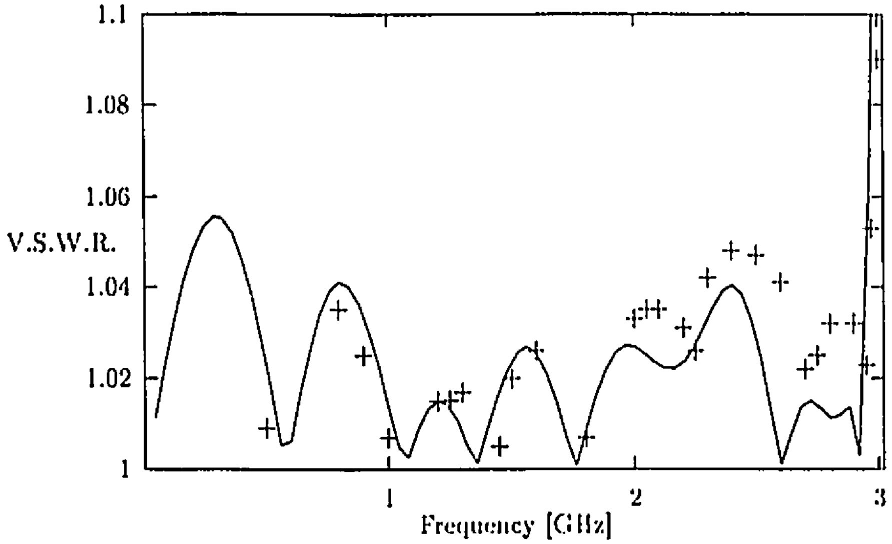

Figure 4.13: Comparison of a 3 GHz low-pass coaxial filter, +++ measured by [47].

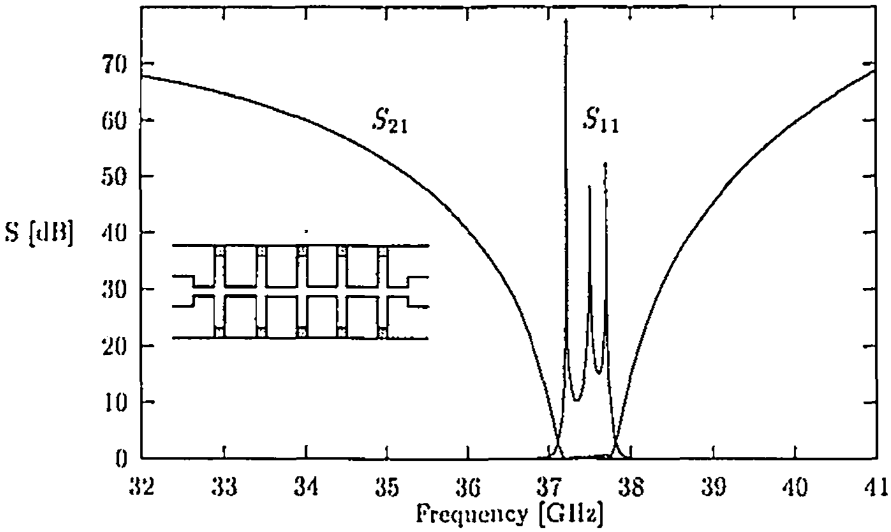

Figure 4.14: Ka-band bandpass coax filter.

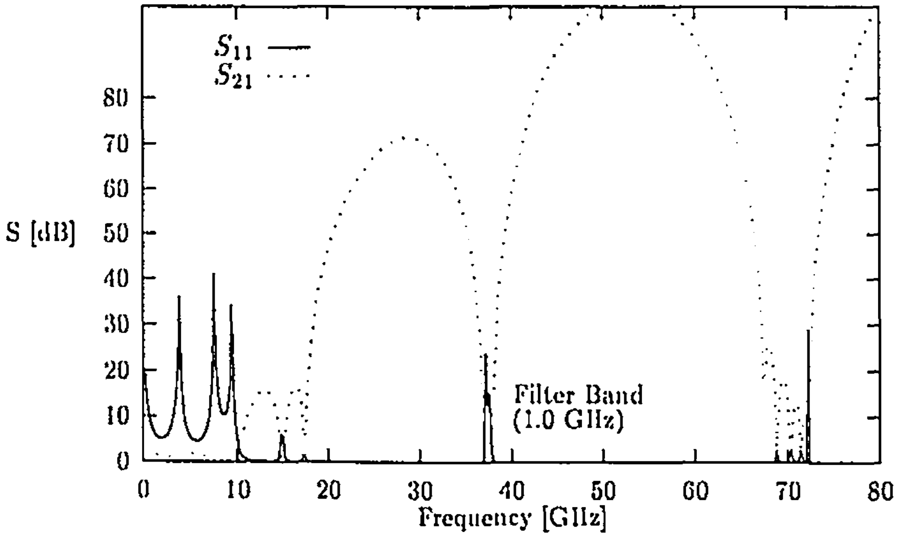

Figure 4.15: Broad band view of the Ka-band bandpass coax filter.

section	1 & 5	2 & 4	3
Resonator Length [mm]	4.30	2.24	4.40
Iris	1 & 6	2 & 5	3 & 4
Iris thickness [mm]	0.760	0.520	0.352
Iris radius [mm]	1.337	1.368	1.375
Outer radius [mm]	1.46		
Rod radius [mm]	0.625		
Ring permittivity	2.540		

Table 4.2: Data of the Ka-band bandpass coax filter (all dimensions in millimeters).

4.4 Filters with gap

Since the coaxial waveguide has an inner conductor, the D.C. current and very low frequency signals cannot be filtered out by using step discontinuities which only alter the inner and outer diameter. In order to get a true passband filter with no such lowpass property, the implementation of a series of gaps in the center conductor is necessary.

4.4.1 Analysis of the coaxial gap discontinuity

As for the inner (or outer) coaxial step discontinuity, the following assumptions are made: First, the structure is θ-symmetrical and, secondly, the incident wave is TEM. Therefore, three field components (E_ρ, H_θ and E_z) are sufficient to describe the field at any points of the discontinuity (Fig. 4.16) and, thereby, only TM modes are excited in the empty waveguide.

In the case of an empty circular waveguide of radius b, the boundary conditions are reduced to $E_z = 0$ at $\rho = b$. The Bessel function of first kind, J_n, satisfies the Helmholtz equation (4.6) and the boundary condition. Thus, R can be rewritten as:

$$R(\rho) = J_n(k_\rho \rho) \qquad (4.24)$$

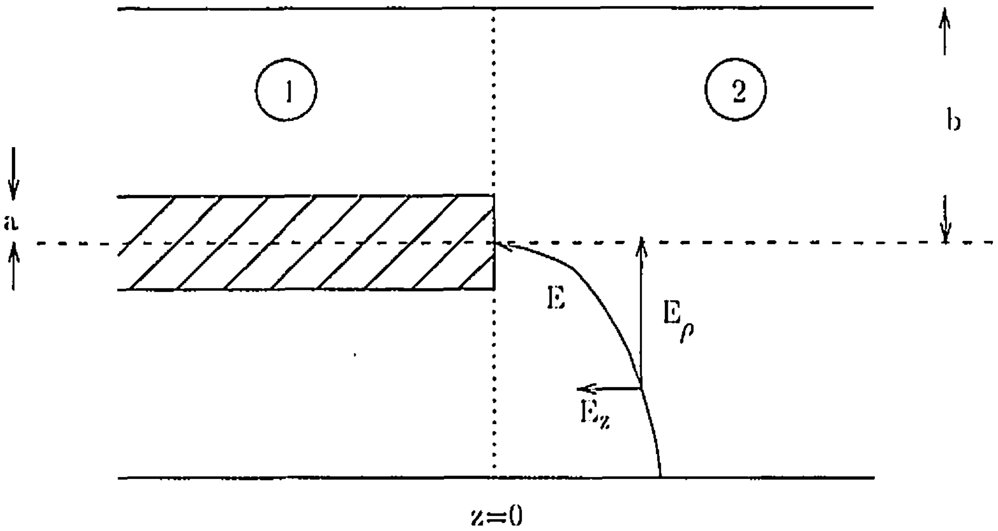

Figure 4.16: E-Field decomposition at a coaxial gap discontinuity.

with the boundary condition: $J_n(k_\rho b) = 0$. The periodicity of $\Phi(\theta)$ indicates that n must be an integer. Furthermore, the complete absence of E_θ and H_ρ allows a choice of $n = 0$ (only $TM_{0,m}$ modes).

The electric and magnetic fields tangential to the discontinuity plane are obtained as:

$$E_\rho = -\frac{1}{\omega\varepsilon}\sum_{m=1}^{\infty} \alpha_m \beta_m T_m J_0'(k_m\rho)\left(A_m e^{-j\beta_m z} + B_m e^{j\beta_m z}\right) \tag{4.25}$$

$$H_\theta = -\sum_{m=1}^{\infty} \alpha_m \beta_m T_m J_0'(k_m\rho)\left(A_m e^{-j\beta_m z} - B_m e^{j\beta_m z}\right) \tag{4.26}$$

where α_m is the ortho-normalized factor:

$$\alpha_m = \frac{\sqrt{2}}{k_{\rho 0,m} b J_1(k_{\rho 0,m} b)} \tag{4.27}$$

After the field expressions are known, it is now possible to apply the mode matching procedure at the gap discontinuity (at $z = 0$) (Fig. 4.16) :

$$\begin{aligned} E_\rho^{(2)} &= E_\rho^{(1)} \quad \rho \in [a,b] \\ &= 0 \quad \rho \in [0,a] \end{aligned}$$

and

$$H_\theta^{(2)} = H_\theta^{(1)} \quad \rho \in [a,b].$$

Using again the property of mode orthogonality, e.g. each continuity equation multiplied by the weighted orthonormal functions and integrated within the appropriate boundaries, leads to the following equation (including the TEM mode) for the E_ρ-field:

$$\begin{aligned} A_i^{(2)} + B_i^{(2)} &= \frac{\beta_0^{(1)} T_0^{(1)} \alpha_0^{(1)} \varepsilon^{(2)}}{\beta_i^{(2)} T_i^{(2)} \varepsilon^{(1)}} CI_{i,0}^{(2)} \left(A_0^{(1)} + B_0^{(1)} \right) + \\ &\quad \sum_{q=1}^{\infty} \frac{\beta_q^{(1)} T_q^{(1)} \varepsilon^{(2)}}{\beta_i^{(2)} T_i^{(2)} \varepsilon^{(1)}} CI_{i,q}^{(2)} \left(A_q^{(1)} + B_q^{(1)} \right) \qquad (4.28) \\ A^{(2)} + B^{(2)} &= LH \left(A^{(1)} + B^{(1)} \right) \qquad (4.29) \end{aligned}$$

where $CI_{i,q}^{(2)}$ are the coupling integrals:

$$\begin{aligned} CI_{i,q}^{(2)} &= \alpha_q^{(1)} \alpha_i^{(2)} \int_a^b \rho B_0'(k_q^{(1)}\rho) J_0'(k_i^{(2)}\rho) d\rho \\ &= \alpha_q^{(1)} \alpha_i^{(2)} k_q^{(1)} k_i^{(2)} \frac{a k_i^{(2)} B_1(k_q^{(1)} a) J_0(k_i^{(2)} a)}{k_i^{(2)\,2} - k_q^{(1)\,2}} \\ CI_{i,0}^{(2)} &= \alpha_i^{(2)} \int_a^b J_0'(k_i^{(2)}\rho) d\rho = -\alpha_i^{(2)} J_0(k_i^{(2)} a) \end{aligned}$$

For the H_θ matching condition, the final equation is obtained by simply transposing the matrix LH ($LE = LH^t$) yielding:

$$A^{(1)} - B^{(1)} = LE \left(A^{(2)} - B^{(2)} \right) \qquad (4.30)$$

Finally, using the procedure defined in Appendix A yields the scattering matrix of the discontinuity.

4.4.2 Results

- Convergence analysis

The first investigation concerns the convergence rate for the calculation of the equivalent capacitance of a coaxial guide terminated by a circular waveguide (frequency as parameters). The coax cable is 3/4 inch in radius (Fig. 4.17). A comparison (dotted line) is given with results from [52] where the Rayleigh-Ritz variational technique is utilized to obtain the equivalent capacitance from the coupling matrices. In Figure 4.17, the upper dotted line (at 220.18 fF) has been calculated at 1 GHz and the lower one (at 219.49 fF) at 1 kHz. Therefore, at low frequencies (1kHz and 1 GHz), 20 modes are sufficient to calculate the capacitance, whereas 30 modes are necessary at higher frequencies.

Table 4.3 compares results from different methods used to analyze this type of discontinuity. Results from the MMM have been obtained using 24 modes which are sufficient to achieve a 0.1% accuracy.

Radius	Freq	Result from [52]	Result from [45]	Result from [46]	Result from [49]	This Method
7 mm	1 kHz	80.66	79.70	79.7	79.88	79.63
	1 GHz	80.70		79.7	79.917	79.67
14 mm	1 kHz	164.56	159.40	159.4	159.76	159.27
	1 GHz	164.85			160.039	159.53
3/4 in.	1 kHz	219.49	216.89	217.0	217.40	216.50
	1 GHz	220.18		217.7	218.07	217.17

Table 4.3: Values (fF) for the discontinuity capacitance of a 50 Ω-coaxial guide terminated in a circular waveguide. [52]: Rayleigh-Ritz variational technique, [45]: Approximation of the eigenfunctions using Hahn series, [46]: Interpolation of Somlo's data, [49]: Least-square boundary residual method.

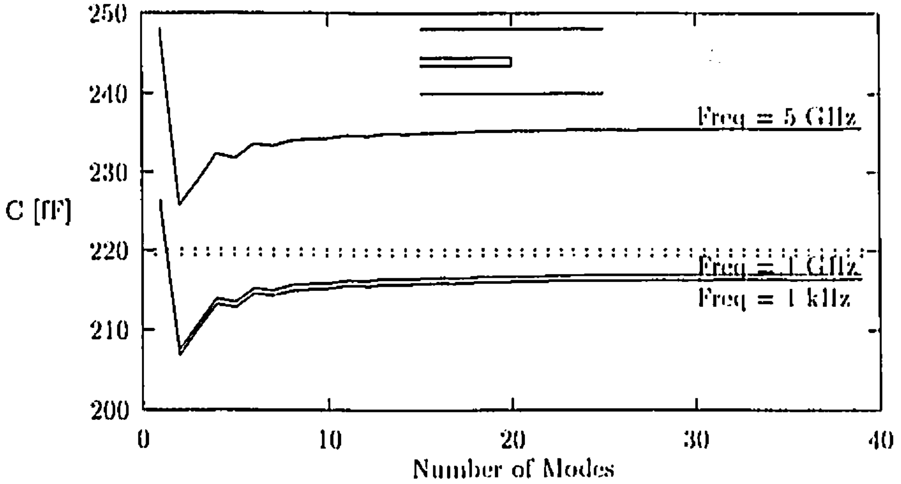

Figure 4.17: Convergence analysis for the equivalent capacitance of a coaxial guide terminated by a circular waveguide for different frequencies, dotted line calculated from [52], upper line at 1 GHz (220.18 fF) and lower line at 1 kHz (219.49 fF).

- Short-ended coaxial cable

A short-ended coaxial cable is also analyzed and compared with results from [35, pp. 178-179]. At low frequencies, a perfect match between both methods is observed (Fig 4.18). However, since the formula used in [35] is independent of the frequencies, the discrepancy increases with frequency.

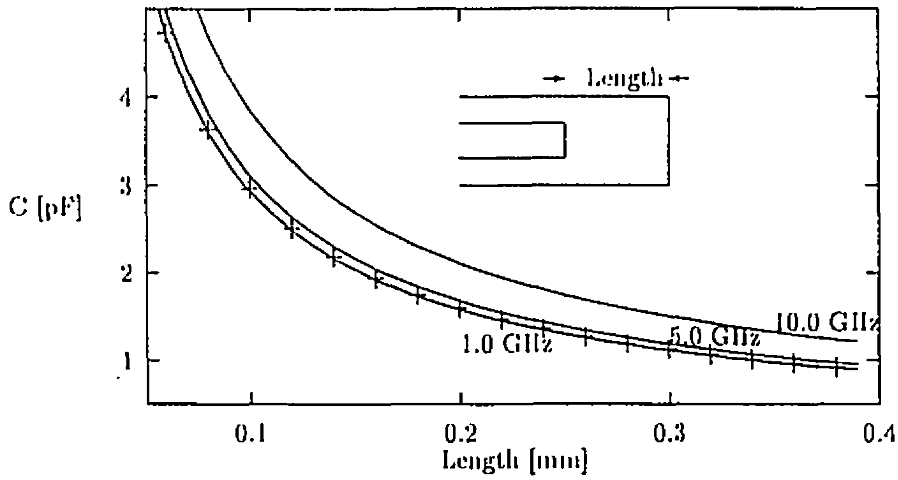

Figure 4.18: Equivalent capacitance of a short-ended coaxial guide.+++ computed by [35]

- Gapped coaxial filters

On the basis of the previous analysis a gapped coaxial filter has been analyzed. The structure uses half wavelength resonator sections separated by quarter wavelength coupling section ([38], pp. 477-481). Each coupling section works as K-inverter[2]. A 21

---

[2] Which is an impedance transformer, from Z_a at one end to $Z_b = K^2/Z_a$ at the other end.

GHz bandpass filter in a (K118 Wiltron) semi-rigid coaxial cable has been designed and optimized (see Table 4.4 for the dimensions). A qualitative corrected electrical length

Outer Radius [mm]	1.205
Inner Radius [mm]	0.041
$\lambda/2$ Sect. 1 & 7 [mm]	4.252 (6.016)
$\lambda/4$ Sect. 2 & 6 [mm]	1.400 (3.164)
$\lambda/2$ Sect. 3 & 5 [mm]	4.296 (6.060)
$\lambda/4$ Sect. 4 [mm]	1.510 (3.274)
Gap 1 & 8 [mm]	0.020
Gap 2 & 7 [mm]	0.072
Gap 3 & 6 [mm]	0.031
Gap 4 & 5 [mm]	0.110

Table 4.4: Data for the optimized gapped 3-section coaxial filter, corrected electrical lengths in parentheses.

(defined in [38], pp. 479) has been added in the Table 4.4 in order to obtain a better simulation of the K-inverter circuit. The corrective value has been estimated to 1.764 *mm* (at 20 *GHz*). Figures 4.19 and 4.20 shows the response of the optimized filter. The next passband is at 39 *GHz* which allows a stopband of 18 GHz between the two passbands (Fig. 4.20). This stopband may be improved by cascading a 30 *GHz* lowpass filter (structure defined in section 4.3.4).

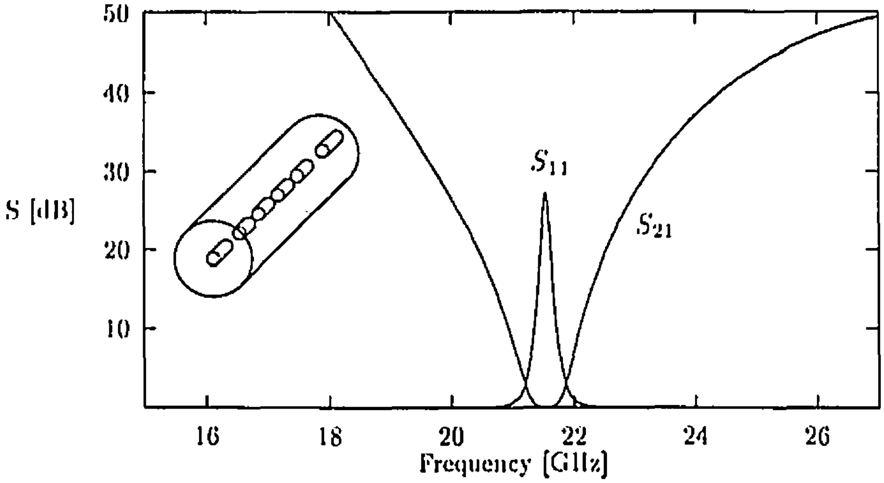

Figure 4.19: S-parameters of a gapped coaxial filter.

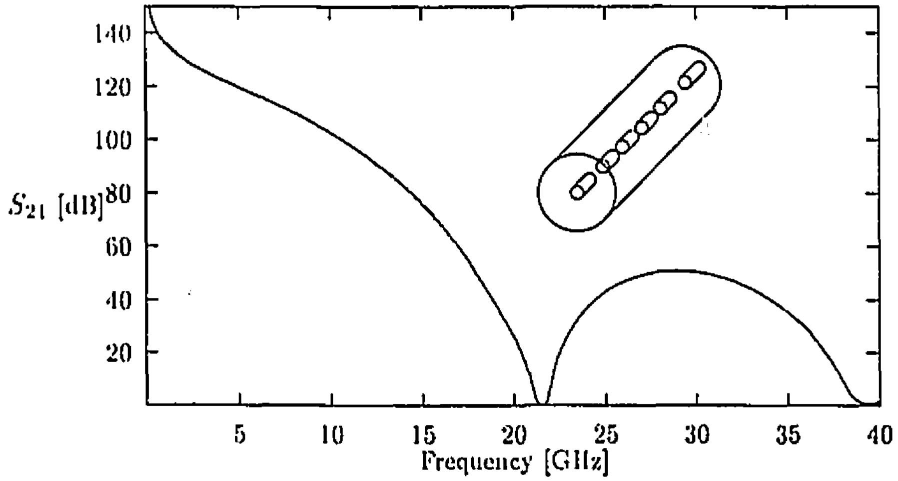

Figure 4.20: Broad band view of the gapped coaxial bandpass filter insertion loss.

Chapter 5

Metal-insert circular waveguide filter

The circular waveguide is an important transmission medium for antenna feeding systems due to its direct compatibility with the fields in horn antennas and because two orthogonal polarized waves can propagate simultaneously inside the guide. Moreover, the circular guide has the advantages over the rectangular waveguide of greater power-handling capacity and lower attenuation for a given cutoff wavelength.

In analogy with the metal-insert filter in rectangular waveguide [22], in this chapter, a metal septum loaded circular waveguide bandpass filter is presented and analyzed (Fig. 5.1).

The quasi-rectangular discontinuity of the metal insert is approximated by a bow-tie shaped discontinuity (Fig. 5.2) to avoid dealing with θ-dependent boundary conditions. This is computationally more efficient since the resulting eigenfunctions are mathematically easier to handle. This kind of discontinuity has not been treated in the literature[1] before and provides the basis for the field-theory designs of metal insert filters in circular waveguides.

---

[1] the electromagnetic field in the sector waveguide has been only sketched in [56]

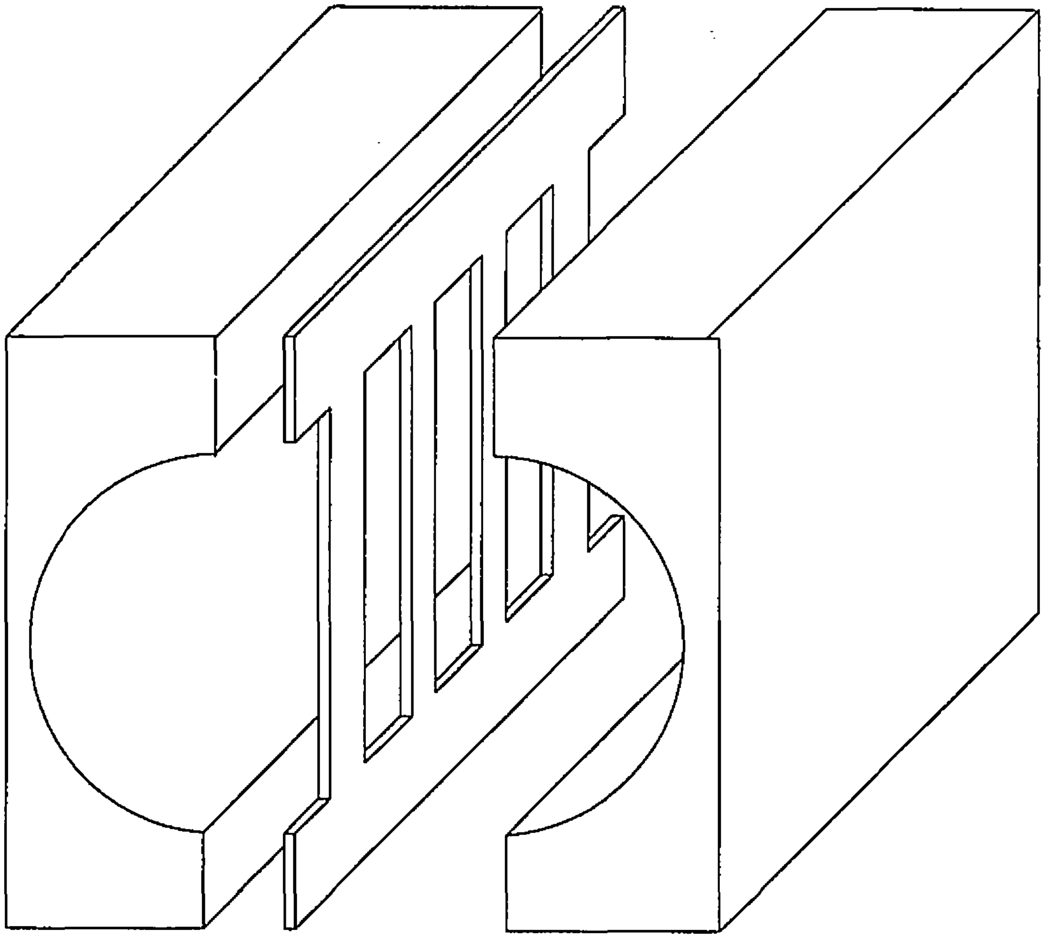

Figure 5.1: Structure of the metal insert loaded circular waveguide filter.

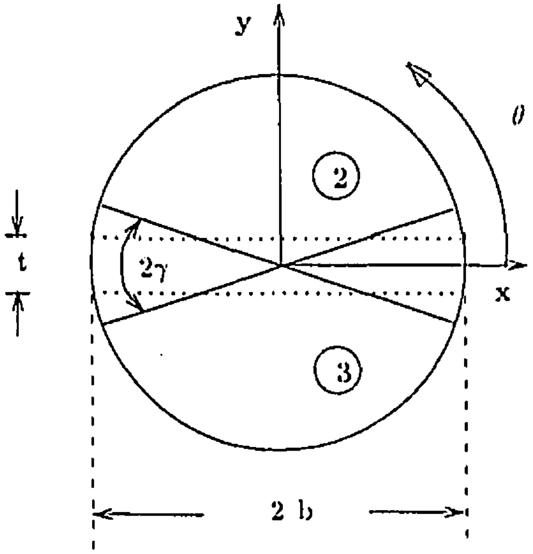

Figure 5.2: Bow-tie shaped discontinuity

5.1 Potential equations

Let $\bar{\Psi}$ be the vector potential appropriate to describe the structure under investigation. Assuming wave propagation in the z-direction:

$$\bar{\Psi}^{(e,h)} = \psi^{(e,h)}\,\hat{z}$$

With a TE_{11} mode incident, all field components are present at the discontinuity and the analysis must include TE and TM modes. Starting from the general field expression:

$$E_\rho = \frac{1}{j\omega\varepsilon}\frac{\partial^2\psi^{(e)}}{\partial\rho\partial z} - \frac{1}{\rho}\frac{\partial\psi^{(h)}}{\partial\theta} \tag{5.1}$$

$$E_\theta = \frac{1}{j\omega\varepsilon\rho}\frac{\partial^2\psi^{(e)}}{\partial\theta\partial z} + \frac{\partial\psi^{(h)}}{\partial\rho} \tag{5.2}$$

$$E_z = \frac{1}{j\omega\varepsilon}\left(\frac{\partial^2}{\partial z^2} + k^2\right)\psi^{(e)} \tag{5.3}$$

$$H_\rho = \frac{1}{\rho}\frac{\partial \Psi^{(e)}}{\partial \theta} + \frac{1}{j\omega\mu}\frac{\partial^2 \Psi^{(h)}}{\partial \rho \partial z} \tag{5.4}$$

$$H_\theta = -\frac{\partial \Psi^{(e)}}{\partial \rho} + \frac{1}{j\omega\mu\rho}\frac{\partial^2 \Psi^{(h)}}{\partial \theta \partial z} \tag{5.5}$$

$$H_z = \frac{1}{j\omega\mu}\left(\frac{\partial^2}{\partial z^2} + k^2\right)\Psi^{(h)} \tag{5.6}$$

TE or TM modes can be obtained by letting $\bar{\Psi}^{(h)} = 0$ for TM mode fields and $\bar{\Psi}^{(e)} = 0$ for TE mode fields. The electromagnetic field in each subregion of the filter is a linear superposition of both TE and TM fields. The Helmholtz equation:

$$\frac{1}{\rho}\frac{\partial}{\partial \rho}\left(\rho\frac{\partial \Psi^{(e,h)}}{\partial \rho}\right) + \frac{1}{\rho^2}\frac{\partial^2 \Psi^{(e,h)}}{\partial \theta^2} + \frac{\partial^2 \Psi^{(e,h)}}{\partial z^2} + k^2\Psi^{(e,h)} = 0 \tag{5.7}$$

(with $k^2 = k_0^2\varepsilon_r$) is solved by using the method of separation of variables, e.g. one can write the potential $\Psi^{(e,h)}$ as:

$$\Psi^{(e,h)}(\rho, \theta, z) = R(\rho).\Phi(\theta).Z(z) \tag{5.8}$$

This yields three independent equations[2]:

5.1.1 θ-equation

The first refers to the θ-equation and can be written as follows:

$$\frac{d\Phi^{(e,h)}(\theta)}{d\theta} + k_\theta^{(e,h)2}\Phi^{(e,h)}(\theta) = 0$$

A solution for $\Phi^{(e,h)}$ is:

$$\Phi^{(e,h)}(\theta) = A\sin(k_\theta^{(e,h)}\theta) + B\cos(k_\theta^{(e,h)}\theta)$$

where the constants A and B are determined by applying the boundary conditions:

---

[2] Only two equations will be discussed since the z-equation has the obvious solution $Z(z) = e^{-j\beta z}$

$$\left.\begin{array}{ll}\text{at} & \theta = \gamma \\ \text{at} & \theta = \pi - \gamma\end{array}\right\} E_\rho = E_z = 0 \quad \text{and} \quad H_\theta = 0$$

Although the boundary condition are only slightly different for TM and TE modes, they lead in fact to two very different solutions.

1) For the TM modes, according to equation 5.3, $E_z = \frac{k^2-\beta^2}{j\omega\varepsilon}\psi^{(e)}$ and $\psi^{(e)}$ is proportional to $\Phi^{(e)}(\theta)$. Therefore the θ-boundary condition in the upper guide (section (2), Fig. 5.2) can be rewritten as:

$$\begin{aligned} A\sin(k_0^{(e)}\gamma) \qquad + B\cos(k_0^{(e)}\gamma) \qquad &= 0 \\ A\sin(k_0^{(e)}(\pi-\gamma)) + B\cos(k_0^{(e)}(\pi-\gamma)) &= 0 \end{aligned}$$

for which the solution is:

$$\Phi^{(e)}(\theta) = \sin\left(k_0^{(e)}(\theta-\gamma)\right)$$

with $k_0^{(e)} = n\pi/(\pi - 2\gamma)$. For the lower guide (section (3), Fig. 5.2), the solution is:

$$\Phi^{(e)}(\theta) = \sin\left(k_0^{(e)}(\theta-\gamma-\pi)\right)$$

2) In the case of TE modes, $E_\rho = -\frac{\partial\psi^{(h)}}{\rho\partial\theta}$ and $\psi^{(h)} \propto \Phi^{(h)}(\theta)$. The boundary condition becomes:

$$\left.\begin{array}{l} k_0^{(h)}A\cos(k_0^{(h)}\gamma) - \qquad k_0^{(h)}B\sin(k_0^{(h)}\gamma) = 0 \\ k_0^{(h)}A\cos(k_0^{(h)}(\pi-\gamma)) - k_0^{(h)}B\sin(k_0^{(h)}(\pi-\gamma)) = 0 \end{array}\right\} \Rightarrow \left\{ \begin{array}{l} A = B\tan(k_0^{(h)}\gamma) \\ k_0^{(h)} = \frac{n\pi}{\pi-2\gamma} \end{array}\right.$$

yielding

$$\begin{aligned} \Phi^{(h)}(\theta) &= \cos\left(k_0^{(h)}(\theta-\gamma)\right) && \text{in the upper guide} \\ \Phi^{(h)}(\theta) &= \cos\left(k_0^{(h)}(\theta-\gamma-\pi)\right) && \text{in the lower guide} \end{aligned}$$

In the following, $\nu = k_0^{(e,h)}$.

5.1.2 ρ-equation

The second equation is the ρ-equation:

$$\rho^2 \frac{d^2 R^{(c,h)}(\rho)}{d\rho^2} + \rho \frac{dR^{(c,h)}(\rho)}{d\rho} + \left[(k^2 - \beta^2)\rho^2 - \nu^2 \right] R^{(c,h)}(\rho) = 0 \tag{5.9}$$

where $k_\rho^{(c,h)2} = k^{(c,h)2} - \beta^{(c,h)2}$. In the upper or lower waveguide, by imposing the boundary conditions, the solution is a sum of Bessel functions of both the first and second kinds. However, Bessel functions of the second kind have an infinite value at $\rho = 0$ which is physically impossible for this structure (Fig. 5.2. Therefore:

$$R^{(c,h)}(\rho) = J_\nu(k_\rho^{(c,h)}\rho) \text{ with } \begin{cases} \text{TM Mode } J_\nu(k_{\rho_{n,m}}^{(c)} b) = 0 \\ \text{TE Mode } J'_\nu(k_{\rho_{n,m}}^{(h)} b) = 0 \end{cases}$$

The potential function in the upper guide (an equivalent expression is obtained in the lower guide) is expressed as:

$$\begin{aligned} \Psi^{(e)}(\rho, \theta, z) &= J_\nu(k_\rho^{(c)}\rho).\sin(\nu(\theta - \gamma)).e^{-j\beta z} \\ \Psi^{(h)}(\rho, \theta, z) &= J_\nu(k_\rho^{(h)}\rho).\cos(\nu(\theta - \gamma)).e^{-j\beta z} \end{aligned}$$

with

$$\beta_{n,m}^{(c,h)2} = k^2 - k_\rho^{(c,h)2} = k_0^2 \varepsilon_r - k_\rho^{(c,h)2}$$

5.2 Field expressions

The tangential electric field can be written as follows:

$$\begin{aligned} \vec{E}_T &= -\frac{1}{\omega\varepsilon} \sum_{n=s}^{\infty} \sum_{m=1}^{\infty} \beta_{n,m}^{(c)} T_{n,m}^{(e)} \left(A_{n,m} + B_{n,m} \right) \vec{e}_{n,m}^{(c)} \\ &\quad - \sum_{p=0}^{\infty} \sum_{q=1}^{\infty} T_{p,q}^{(h)} \left(C_{p,q} + D_{p,q} \right) \vec{e}_{p,q}^{(h)} \end{aligned} \tag{5.10}$$

The superscript (e) indicates TM modes and the superscript (h) TE modes. The parameter s is equal to 0 in the case of a circular empty waveguide and 1 in the case of a half circular waveguide, to take into account the fact that the $TM_{0,m}$ mode does not exist in the latter one. Furthermore, the eigenfunctions $\vec{e}$ satisfy the orthogonality property, i.e.:

$$\int_S \vec{e}^{\,(e)}_{n,m}.\vec{e}^{\,(e)}_{n',m'}dS = \int_S \vec{e}^{\,(h)}_{n,m}.\vec{e}^{\,(h)}_{n',m'}dS = \delta_{n,n'}\delta_{m,m'} \tag{5.11}$$

The definition of the vectors $\vec{e}^{\,(e)}_{n,m}$ and $\vec{e}^{\,(h)}_{p,q}$ are given in appendix D as well as the $1W$-normalization factor $T^{(e)}_{n,m}$ and $T^{(h)}_{p,q}$ for each subregion of the filter.

In the empty circular waveguide, any wave can be decomposed into two orthogonal waves. One type of mode is marked with the superscript "s" and denotes the mode with the E-field perpendicular to the septum. The second one is marked with the superscript "c" and denotes the modes with the E-field parallel to the septum. However, the TM_{0m} modes exist only as "c"-modes and the TE_{0q} only as "s"-modes.

The tangential magnetic field is written as:

$$\begin{aligned}\vec{H}_T \quad = \quad & \sum_{n=s}^{\infty}\sum_{m=1}^{\infty} T^{(e)}_{n,m}\left(A_{n,m} - B_{n,m}\right)\vec{h}^{(e)}_{m,n} \\ & + \frac{1}{\omega\mu}\sum_{p=0}^{\infty}\sum_{q=1}^{\infty} \beta^{(h)}_{p,q} T^{(h)}_{p,q}\left(C_{p,q} - D_{p,q}\right)\vec{h}^{(h)}_{p,q}\end{aligned}$$

The definition of $\vec{h}^{(e)}_{m,n}$ and $\vec{h}^{(h)}_{p,q}$ are given as well in Appendix D.

5.3 Matching equations

In order to obtain the S-Matrix of the 3-port discontinuity, the tangential electric field is matched at the discontinuity, e.g. $z = 0$ (Fig. 5.2):

$$\left.\begin{array}{lll} \vec{E}_T^{(1)} = & \vec{E}_T^{(2)} & \theta \in [\gamma, \pi - \gamma] \\ = & \vec{E}_T^{(3)} & \theta \in [\pi + \gamma, 2\pi - \gamma] \\ = & 0 & \theta \in [0, \gamma], [\pi - \gamma, \pi + \gamma] \text{ and } [2\pi - \gamma, 2\pi] \end{array}\right\} \forall \rho \in [0, b] \tag{5.12}$$

where the different fields $\vec{E}_T$ are defined in equation 5.10. Since the tangential electric field in the empty circular waveguide is expressed as the sum of four independent and orthogonal sets of eigenfunctions, $\vec{e}_{i,j}^{(c1s)}$, $\vec{e}_{i,j}^{(c1c)}$, $\vec{e}_{i,j}^{(h1s)}$ and $\vec{e}_{i,j}^{(h1c)}$, respectively, the mode matching procedure is made possible by successively multiplying equation (5.12) by each eigenfunction and then integrating over the circular waveguide cross-section.

5.3.1 First coupling equation

The first coupling equation, e.g. equation (5.12) multiplied by $\vec{e}_{i,j}^{(c1s)}$ and integrated over S_1 leads to:

$$\int_{S_1} \vec{E}_T^{(1)}.\vec{e}_{i,j}^{(c1s)} w(\rho,\theta) dS = \int_{S_2} \vec{E}_T^{(2)}.\vec{e}_{i,j}^{(c1s)} w(\rho,\theta) dS + \int_{S_3} \vec{E}_T^{(3)}.\vec{e}_{i,j}^{(c1s)} w(\rho,\theta) dS$$

By introducing the expressions for the different $\vec{E}_T$, this equation can be rewritten as:

$$\begin{aligned} &\int_{S_1} \left[-\frac{1}{\omega\varepsilon_1} \sum_{n=1}^{\infty} \sum_{m=1}^{\infty} E_{nm}^{(c1s)} \vec{e}_{nm}^{(c1s)} - \frac{1}{\omega\varepsilon_1} \sum_{n=0}^{\infty} \sum_{m=1}^{\infty} E_{nm}^{(c1c)} \vec{e}_{nm}^{(c1c)} \right. \\ &\qquad \left. - \sum_{p=0}^{\infty} \sum_{q=1}^{\infty} E_{pq}^{(h1s)} \vec{e}_{pq}^{(h1s)} - \sum_{p=0}^{\infty} \sum_{q=1}^{\infty} E_{pq}^{(h1c)} \vec{e}_{pq}^{(h1c)} \right] .\vec{e}_{ij}^{(c1s)} \rho d\rho d\theta \\ &= \int_{S_2} \left[-\frac{1}{\omega\varepsilon_2} \sum_{n=1}^{\infty} \sum_{m=1}^{\infty} E_{nm}^{(c2)} \vec{e}_{nm}^{(c2)} - \sum_{p=0}^{\infty} \sum_{q=1}^{\infty} E_{pq}^{(h2)} \vec{e}_{pq}^{(h2)} \right] .\vec{e}_{ij}^{(c1s)} \rho d\rho d\theta \\ &+ \int_{S_3} \left[-\frac{1}{\omega\varepsilon_3} \sum_{n=1}^{\infty} \sum_{m=1}^{\infty} E_{nm}^{(c3)} \vec{e}_{nm}^{(c3)} - \sum_{p=0}^{\infty} \sum_{q=1}^{\infty} E_{pq}^{(h3)} \vec{e}_{pq}^{(h3)} \right] .\vec{e}_{ij}^{(c1s)} \rho d\rho d\theta \end{aligned} \tag{5.13}$$

where

$$E^{(c1s)}_{mn} = \beta^{(c1s)}_{nm} T^{(c1s)}_{nm} \left(A^{(1s)}_{nm} + B^{(1s)}_{nm} \right) \tag{5.14}$$

$$E^{(c1c)}_{mn} = \beta^{(c1c)}_{nm} T^{(c1c)}_{nm} \left(A^{(1c)}_{nm} + B^{(1c)}_{nm} \right) \tag{5.15}$$

$$E^{(h1s)}_{pq} = T^{(h1s)}_{pq} \left(C^{(1s)}_{pq} + D^{(1s)}_{pq} \right) \tag{5.16}$$

$$E^{(h1c)}_{pq} = T^{(h1c)}_{pq} \left(C^{(1c)}_{pq} + D^{(1c)}_{pq} \right) \tag{5.17}$$

and

$$E^{(c2)}_{mn} = \beta^{(c2)}_{nm} T^{(c2)}_{nm} \left(A^{(2)}_{nm} + B^{(2)}_{nm} \right) \tag{5.18}$$

$$E^{(h2)}_{pq} = T^{(h2)}_{pq} \left(C^{(2)}_{pq} + D^{(2)}_{pq} \right) \tag{5.19}$$

Similar relations are obtained for the lower guide (superscript (3) instead of (2)). The LHS of equation (5.13) is simplified by using the orthogonality property of the eigenfunctions, i.e. equation (5.11):

$$\begin{aligned}
&\frac{1}{\omega\varepsilon_1}\beta^{(c1)}_{i,j} T^{(c1)}_{i,j} \left(A^{(1s)}_{i,j} + B^{(1s)}_{i,j} \right) = \\
&\quad \frac{1}{\omega\varepsilon_2} \sum_{n=1}^{\infty} \sum_{m=1}^{\infty} \beta^{(c2)}_{n,m} T^{(c2)}_{n,m} \left(A^{(2)}_{n,m} + B^{(2)}_{n,m} \right) \int_{\gamma}^{\pi-\gamma} \int_0^b \vec{e}^{\,(c2)}_{n,m} . \vec{e}^{\,(c1s)}_{i,j} \rho d\rho d\theta \\
&\qquad + \sum_{p=0}^{\infty} \sum_{q=1}^{\infty} T^{(h2)}_{p,q} \left(C^{(2)}_{p,q} + D^{(2)}_{p,q} \right) \int_{\gamma}^{\pi-\gamma} \int_0^b \vec{e}^{\,(h2)}_{p,q} . \vec{e}^{\,(c1s)}_{i,j} \rho d\rho d\theta \\
&+ \frac{1}{\omega\varepsilon_3} \sum_{n=1}^{\infty} \sum_{m=1}^{\infty} \beta^{(c3)}_{n,m} T^{(c3)}_{n,m} \left(A^{(3)}_{n,m} + B^{(3)}_{n,m} \right) \int_{\pi+\gamma}^{2\pi-\gamma} \int_0^b \vec{e}^{\,(c3)}_{n,m} . \vec{e}^{\,(c1s)}_{i,j} \rho d\rho d\theta \\
&\qquad + \sum_{p=0}^{\infty} \sum_{q=1}^{\infty} T^{(h3)}_{p,q} \left(C^{(3)}_{p,q} + D^{(3)}_{p,q} \right) \int_{\pi+\gamma}^{2\pi-\gamma} \int_0^b \vec{e}^{\,(h3)}_{p,q} . \vec{e}^{\,(c1s)}_{i,j} \rho d\rho d\theta
\end{aligned} \tag{5.20}$$

Finally, the coefficients $A^{(1s)}_{i,j}$ and $B^{(1s)}_{i,j}$ have been isolated on the LHS of (5.20) and are a function of all eigenmodes in the upper or lower half guide. The next step is the calculation of the coupling integrals:

1^{st} Coupling integral

The first coupling integral corresponds to the coupling between the TM modes in the upper half guide and the TM^s modes in the circular waveguide. With $n: 1 \rightarrow \infty$ and $i: 1 \rightarrow \infty$:

$$CI_1^s = \int_{\gamma}^{\pi-\gamma} \int_0^b \vec{e}_{n,m}^{(c2)} . \vec{e}_{i,j}^{(c1s)} \rho d\rho d\theta$$

This coupling integral is zero if $n - i$ is odd. For $n - i$ even:

$$CI_1^s = \alpha_{n,m}^{(c2)} \alpha_{i,j}^{(c1s)} \frac{2\sin(i\gamma)}{\nu^2 - i^2} \int_0^b \frac{dJ_\nu(k_{pn,m}^{(c2)}\rho)}{d\rho} \frac{dJ_i(k_{pi,j}^{(c1s)}\rho)}{d\rho} + \frac{i^2}{\rho^2} J_\nu(k_{pn,m}^{(c2)}\rho) J_i(k_{pi,j}^{(c1s)}\rho) d\rho$$

2^{nd} Coupling integral

This coupling integral corresponds to the coupling between the TE modes in the upper half guide and the TM^s modes in the circular waveguide. With $p: 0 \rightarrow \infty$ and $i: 1 \rightarrow \infty$:

$$CI_2^s = \int_{\gamma}^{\pi-\gamma} \int_0^b \vec{e}_{p,q}^{(h2)} . \vec{e}_{i,j}^{(c1s)} \rho d\rho d\theta$$

This coupling integral is zero if $p - i$ is odd. For $p - i$ even:

$$\begin{aligned} CI_2^s = & -\alpha_{p,q}^{(h2)} \alpha_{i,j}^{(c1s)} \frac{2\sin(i\gamma)}{\nu^2 - i^2} \\ & \int_0^b \nu^2 J_\nu(k_{pp,q}^{(h2)}\rho) \frac{dJ_i(k_{pi,j}^{(c1s)}\rho)}{d\rho} + i^2 \frac{dJ_\nu(k_{pp,q}^{(h2)}\rho)}{d\rho} J_i(k_{pi,j}^{(c1s)}\rho) d\rho \end{aligned}$$

The third and fourth coupling integrals are computed from the coupling integrals CI_1^s and CI_2^s. The ρ-coupling integrals do not change, contrary to the θ-integrals which are modified when $n - i$ is even and $n * i$ odd. In this case, the sign of the integral is inverted.

Equation 5.20 can now be rewritten in terms of matrices:

$$\begin{aligned} A^{(1s)} + B^{(1s)} &= LH^{(c1s)}\left(A^{(2)} + B^{(2)}\right) + LH^{(c2s)}\left(C^{(2)} + D^{(2)}\right) + \\ &\quad LH^{(c3s)}\left(A^{(3)} + B^{(3)}\right) + LH^{(c4s)}\left(C^{(3)} + D^{(3)}\right) \end{aligned} \tag{5.21}$$

In the case of $\gamma = 0$ (infinitely thin septum), the matrix equations can be simplified since the respective coupling integrals are equal to zero ($LH^{(c2s)} = 0$ and $LH^{(c4s)} = 0$). Furthermore, the remaining matrices are diagonal and their $(k,k)^{th}$ element can be evaluated as:

$$LH^{(c1s)}(k.k) = \frac{\varepsilon_1}{\varepsilon_2}\frac{\beta_{i,j}^{(c2)}}{\beta_{i,j}^{(c1)}}\frac{T_{i,j}^{(c2)}}{T_{i,j}^{(c1)}}\frac{\sqrt{2}}{2} \quad \text{and} \quad LH^{(c3s)}(k,k) = \frac{\varepsilon_1}{\varepsilon_3}\frac{\beta_{i,j}^{(c3)}}{\beta_{i,j}^{(c1)}}\frac{T_{i,j}^{(c3)}}{T_{i,j}^{(c1)}}\frac{\sqrt{2}}{2}$$

where the k corresponds to the order of the propagation constants of the $TM_{i,j}$ or $TE_{i,j}$ modes arranged in decreasing order, respectively. Both elements equal $\sqrt{2}/2$ in the case $\varepsilon_1 = \varepsilon_2$ and $\varepsilon_1 = \varepsilon_3$. The infinitely thin septum looks like a perfect power divider for this kind of mode. Therefore the output power on each channel is exactly 1/2.

5.3.2 Remaining coupling equations

The solutions for the second, third and fourth coupling equations are given in detail in Appendix D. Only the principal results are given here.

The three remaining coupling equations are:

$$\begin{aligned} \int_{S_1} \vec{E}_T^{(1)}.\vec{e}_{i,j}^{(c1c)} w(\rho,\theta) dS &= \int_{S_2} \vec{E}_T^{(2)}.\vec{e}_{i,j}^{(c1c)} w(\rho,\theta) dS + \int_{S_3} \vec{E}_T^{(3)}.\vec{e}_{i,j}^{(c1c)} w(\rho,\theta) dS \\ \int_{S_1} \vec{E}_T^{(1)}.\vec{e}_{i,j}^{(h1s)} w(\rho,\theta) dS &= \int_{S_2} \vec{E}_T^{(2)}.\vec{e}_{i,j}^{(h1s)} w(\rho,\theta) dS + \int_{S_3} \vec{E}_T^{(3)}.\vec{e}_{i,j}^{(h1s)} w(\rho,\theta) dS \\ \int_{S_1} \vec{E}_T^{(1)}.\vec{e}_{i,j}^{(h1c)} w(\rho,\theta) dS &= \int_{S_2} \vec{E}_T^{(2)}.\vec{e}_{i,j}^{(h1c)} w(\rho,\theta) dS + \int_{S_3} \vec{E}_T^{(3)}.\vec{e}_{i,j}^{(h1c)} w(\rho,\theta) dS \end{aligned}$$

Using the same procedure as in the previous section leads to three matrix equation (from Eqns. D.1, D.4 and D.5):

$$
\begin{aligned}
\mathbf{E}: \quad A^{(1c)} + B^{(1c)} &= LH^{(e1c)}\left(A^{(2)} + B^{(2)}\right) + LH^{(e2c)}\left(C^{(2)} + D^{(2)}\right) + & (5.22)\\
&\quad LH^{(e3c)}\left(A^{(3)} + B^{(3)}\right) + LH^{(e4c)}\left(C^{(3)} + D^{(3)}\right) & \\
\mathbf{H}: \quad C^{(1s)} + D^{(1s)} &= LH^{(h2s)}\left(C^{(2)} + D^{(2)}\right) + LH^{(h4s)}\left(C^{(3)} + D^{(3)}\right) & (5.23)\\
\mathbf{H}: \quad C^{(1c)} + D^{(1c)} &= LH^{(h2c)}\left(C^{(2)} + D^{(2)}\right) + +LH^{(h4c)}\left(C^{(3)} + D^{(3)}\right) & (5.24)
\end{aligned}
$$

The matrices $LH^{(h1s)}$, $LH^{(h3s)}$, $LH^{(h1c)}$ and $LH^{(h3c)}$ are zero (see Appendix D).

5.4 Scattering Matrix of the discontinuity

Four matrix equations have been obtained 5.21, 5.22, 5.23 and 5.24, one for each type of polarization: TE^s, TE^c, TM^s and TM^c, respectively. A similar derivation can be made for the H-field. It can be shown that the H-field coupling matrices are the transposed of the equivalent E-field coupling matrices, e.g. $LE^{(X)} = LH^{(X)t}$ for any superscript X.

$$
\begin{aligned}
A^{(2)} - B^{(2)} &= LE^{(e1s)}\left(A^{(1s)} - B^{(1s)}\right) + LE^{(e1c)}\left(A^{(1c)} - B^{(1c)}\right)\\
C^{(2)} - D^{(2)} &= LE^{(e2s)}\left(A^{(1s)} - B^{(1s)}\right) + LE^{(h2s)}\left(C^{(1s)} - D^{(1s)}\right) +\\
&\quad LE^{(h2c)}\left(C^{(1c)} - D^{(1c)}\right) + LE^{(e2c)}\left(A^{(1c)} - B^{(1c)}\right)\\
A^{(3)} - B^{(3)} &= LE^{(e3s)}\left(A^{(1s)} - B^{(1s)}\right) + LE^{(e3c)}\left(A^{(1c)} - B^{(1c)}\right)\\
C^{(3)} - D^{(3)} &= LE^{(e4s)}\left(A^{(1s)} - B^{(1s)}\right) + LE^{(h4s)}\left(C^{(1s)} - D^{(1s)}\right) +\\
&\quad LE^{(h4c)}\left(C^{(1c)} - D^{(1c)}\right) + LE^{(e4c)}\left(A^{(1c)} - B^{(1c)}\right)
\end{aligned}
$$

This set of equations is reduced in order to simplify the analysis and the program complexity. This reduction is achieved by summarizing all waves propagating in the same direction in one vector (Fig. 5.3):

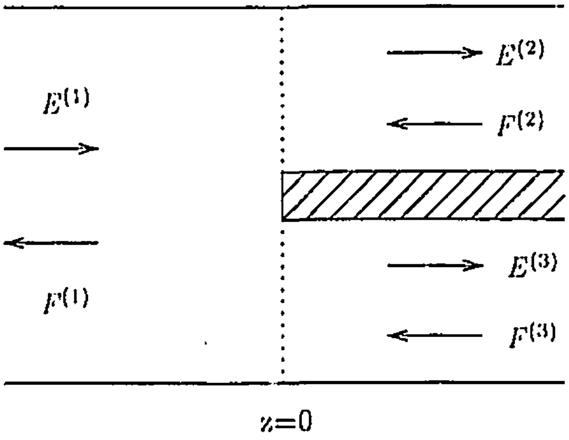

Figure 5.3: Structure of the discontinuity.

1. In the empty circular waveguide

$$E^{(1)} = \begin{pmatrix} A^{(1s)} \\ A^{(1c)} \\ C^{(1s)} \\ C^{(1c)} \end{pmatrix} \quad \text{and} \quad F^{(1)} = \begin{pmatrix} B^{(1s)} \\ B^{(1c)} \\ D^{(1s)} \\ D^{(1c)} \end{pmatrix}$$

   If each vector is of size $(N_1 \times 1)$, then $E^{(1)}$ and $F^{(1)}$ will be a $(4N_1 \times 1)$ vector.

2. In the half circular waveguide (J=2 or J=3)

$$E^{(J)} = \begin{pmatrix} A^{(J)} \\ C^{(J)} \end{pmatrix} \quad \text{and} \quad F^{(J)} = \begin{pmatrix} B^{(J)} \\ D^{(J)} \end{pmatrix}$$

   If each vector is a $(N_J \times 1)$ vector, then $E^{(J)}$ and $F^{(J)}$ will be a $(2N_J \times 1)$ vector.

For a rectangular waveguide discontinuity[3] it has been shown in [31] that certain ratios of the different modes N_J have to be satisfied to obtain fast convergence. For the bifurcated circular waveguide it is assumed that these ratios can be expressed as:

$$N_2 = N_3$$

---

[3] in particular the bifurcated waveguide

$$2N_1 = N_2$$

These ratios give square matrices and the coupling equations can be rewritten as:

$$E^{(1)} + F^{(1)} = \begin{pmatrix} LH^{(e1s)} & LH^{(e2s)} \\ LH^{(e1c)} & LH^{(e2c)} \\ 0 & LH^{(h2s)} \\ 0 & LH^{(h2c)} \end{pmatrix} \left(E^{(2)} + F^{(2)}\right) + \tag{5.25}$$

$$\begin{pmatrix} LH^{(e3s)} & LH^{(e4s)} \\ LH^{(e3c)} & LH^{(e4c)} \\ 0 & LH^{(h4s)} \\ 0 & LH^{(h4c)} \end{pmatrix} \left(E^{(3)} + F^{(3)}\right) \tag{5.26}$$

$$= LLH^{(2)} \left(E^{(2)} + F^{(2)}\right) + LLH^{(3)} \left(E^{(3)} + F^{(3)}\right) \tag{5.27}$$

The $LLH^{(J)}$ matrices are of size $(4N_1 \times 2N_J)$.

$$E^{(2)} - F^{(2)} = \begin{pmatrix} LE^{(e1s)} & LE^{(e1c)} & 0 & 0 \\ LE^{(e2s)} & LE^{(e2c)} & LE^{(h2s)} & LE^{(h2c)} \end{pmatrix} \left(E^{(1)} - F^{(1)}\right) \tag{5.28}$$

$$= LLE^{(2)} \left(E^{(1)} - F^{(1)}\right) \tag{5.29}$$

$$E^{(3)} - F^{(3)} = LLE^{(3)} \left(E^{(1)} - F^{(1)}\right) \tag{5.30}$$

The procedure to obtain $LLE^{(3)}$ is equivalent to that of $LLE^{(2)}$. The LLE matrices are of size $(2N_2 \times 4N_1)$. From equations (5.27), (5.30) and (5.30), the scattering matrix of the discontinuity can be derived:

$$S = \begin{pmatrix} S_{11} & S_{12} & S_{13} \\ S_{21} & S_{22} & S_{23} \\ S_{31} & S_{32} & S_{33} \end{pmatrix}$$

$$= \begin{pmatrix} (\xi + I)^{-1}(\xi - I) & 2(\xi + I)^{-1}LLH^{(2)} & 2(\xi + I)^{-1}LLH^{(3)} \\ LLE^{(2)}(I - S_{11}) & I - LLE^{(2)}S_{12} & -LLE^{(2)}S_{13} \\ LLE^{(3)}(I - S_{11}) & -LLE^{(3)}S_{12} & I - LLE^{(3)}S_{13} \end{pmatrix}$$

with $\xi = LLH^{(2)}LLE^{(2)} + LLH^{(3)}LLE^{(3)}$ and I the identity matrix.

To illustrate the method, the field distribution has been computed from the scattering matrix assuming a TE_{11} mode incident wave parallel to the septum. Figures 5.4

and 5.5 show the results with an septum angle of 4.0 and 19.0 deg. respectively. The number of modes is 36 in both cases (e.g. 18 TE^s, 18 TE^c, 18 TM^S and 18 TM^c in the circular waveguide and 36 TE and 36 TM in both part of bifurcated waveguide).

5.5 Convergence analysis

A convergence analysis of a $1mm$ long septum shows that a minimum of 40 TE and TM modes are necessary for acceptable convergence behavior (Fig. 5.6). For a longer septum, the convergence is reached with fewer modes since the interaction of modes in the bifurcated waveguide is less significant because they are more attenuated.

As stated in section 2.3, the convergence behavior depends on the ratio of the number of modes taken into account in each guide. A convergence analysis of a single bow-tie shaped discontinuity is shown in Figure 5.7. Relatively fast convergence is obtained with the ratio $2N_1 = N_2$. A certain instability can be noticed when the ratio is too low (e.g. a small number of modes in each sub-guide).

For small angles (less than 10 degrees), the coupling between TE and TM modes is negligible (Fig. 5.8 and 5.9). Therefore, if an incident TE mode is assumed, the analysis can be carried out with only TE modes. This assumption is not valid for angles greater than γ_c which increases with the frequency. For frequencies above the TM_{01} mode cut-off frequency, the omission of the TM modes in the analysis leads to wrong results (Fig. 5.9).

5.6 Bandpass filters

The filter structure is composed of a series of resonant cavities separated by coupling septa. The initial filter was synthesized with lumped element theory [57].

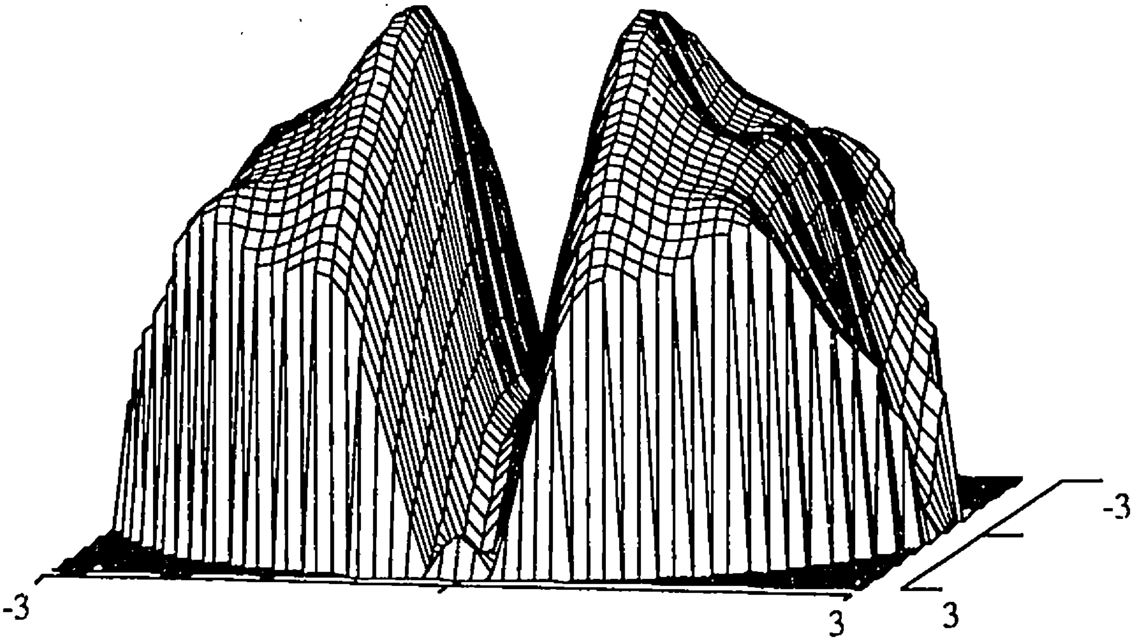

Figure 5.4: Electric field distribution with a TE_{11} incident wave parallel to the septum, $\gamma = 4$ degrees.

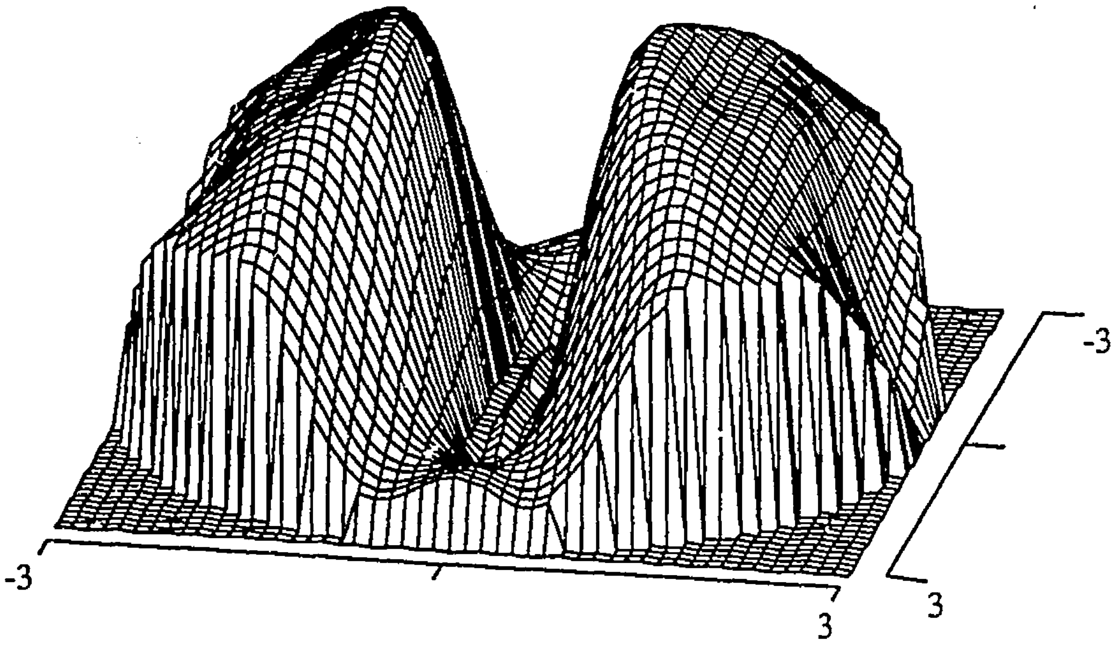

Figure 5.5: Electric field distribution with a TE_{11} incident wave parallel to the septum, $\gamma = 19$ degrees.

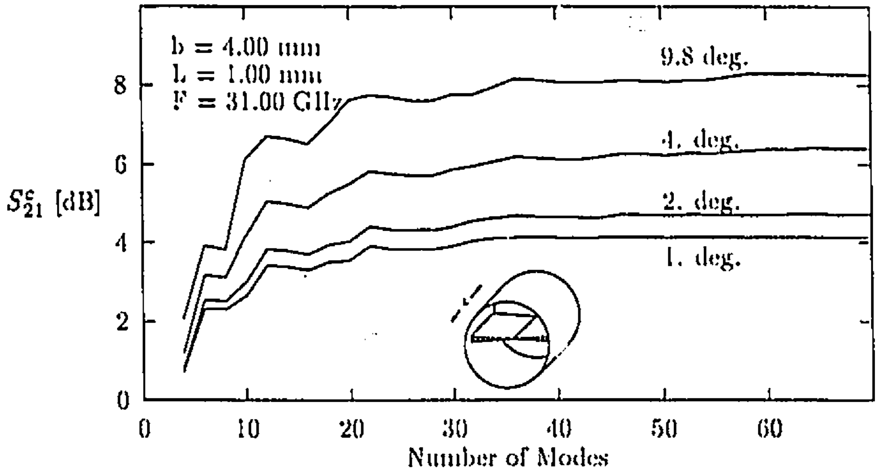

Figure 5.6: Convergence analysis for a metal septum loaded circular waveguide

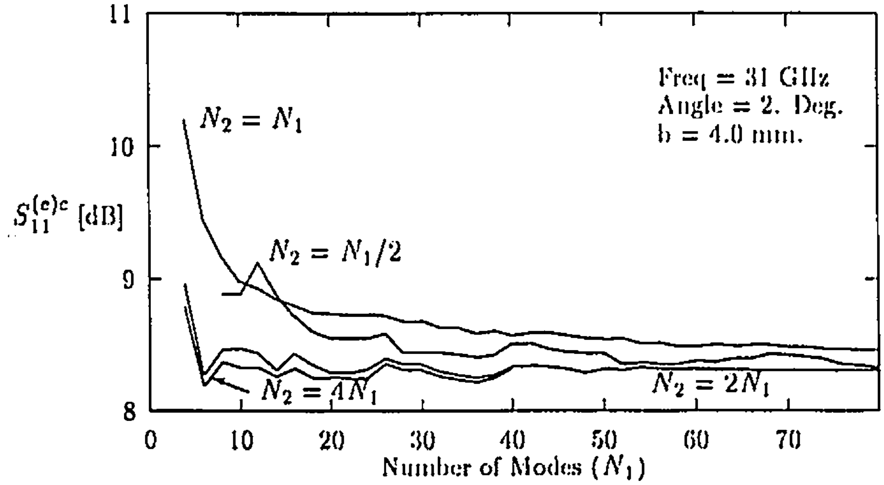

Figure 5.7: Convergence analysis for a metal septum loaded circular waveguide with different mode ratio as parameter.

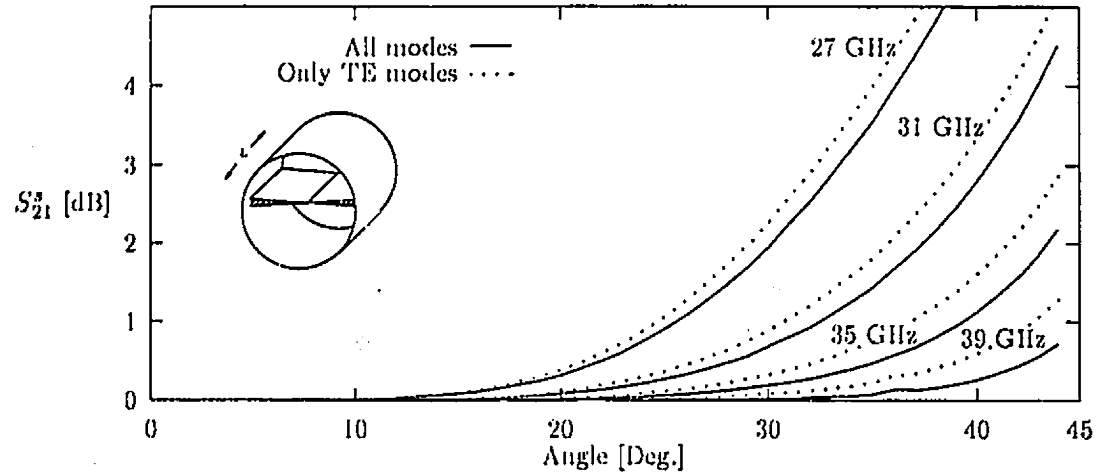

Figure 5.8: "Sine" polarized wave insertion loss versus the angle of a septum loaded circular waveguide ("Sine" polarized wave defined in section 5.2).

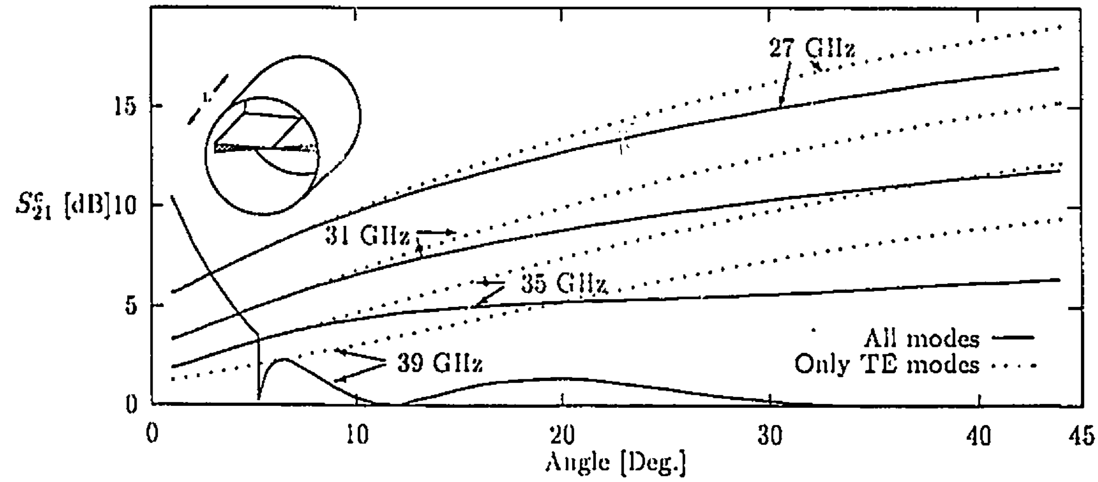

Figure 5.9: "Cosine" polarized wave insertion loss versus the angle of a septum loaded circular waveguide ("Cosine" polarized wave defined in section 5.2). The peak on the 39 GHz curve corresponds to the upper limit of the TE_{21} mode propagation in the furcated waveguide.

These lumped elements utilize K-inverters which consist of a T-network and two transmission lines with electrical length $\phi/2$ connected on both sides of the T-network. A single T-network corresponds to a single metal insert and the values of the inductances may be obtained by using charts such as the one given in Figure 5.10. From these element

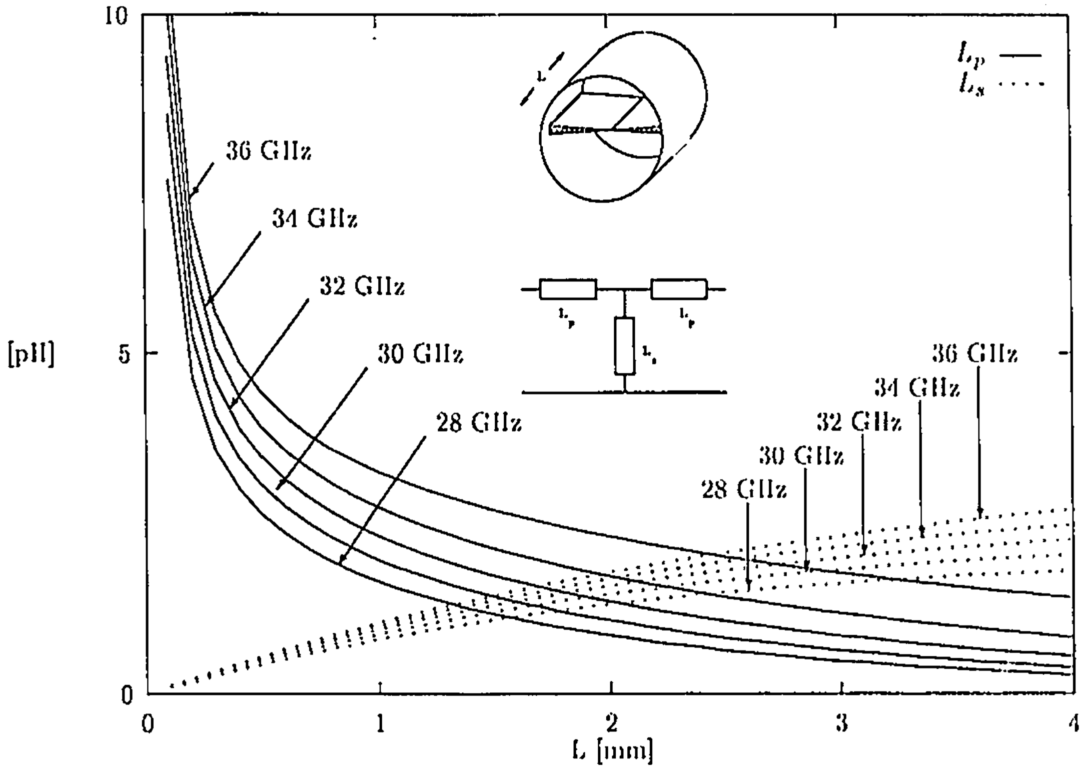

Figure 5.10: Equivalent inductances of a simple metal insert.

values, s-parameters are calculated from which the corresponding insert dimensions can be derived. However, since the higher order mode interaction between subsequent metal septa is not included in the lumped element synthesis, the initial filter response is off by 1 GHz. Nevertheless, these insert dimensions are used as starting values for the full wave analysis, and the generalized s-matrix of the entire filter is optimized using the optimization procedure in [22].

Figure 5.11 shows the theoretical and measured performance of a three-resonator Ka-band filter in a 4 mm radius circular waveguide. The measured insertion loss is less than 1.0 dB in the passband (0.08 dB computed) while the respective return loss is greater than 12 dB (18 dB computed). The reflection coefficient for the polarization perpendicular to the septum is greater than 30 dB (35 dB computed) over the operating range (28 to 38 GHz).

A 31-32 GHz five-section bandpass filter in a 4 mm radius circular waveguide has been designed using the same procedure. The theoretical and measured performance is shown in Figure 5.12. The measured insertion loss is less than 1.2 dB in the passband (0.05 dB computed) while the respective return loss is greater than 20 dB (14 dB computed).

For both filters, the comparison between theoritical analysis and measurement shows an excellent agreement. However, the small discrepancy between both curves is due to the approximation of the rectangular septum by a bow-tie shaped discontinuity, the losses which are not taken into account in the analysis and the inaccuracy of fabrication.

5.7 Coaxial bow-tie shaped discontinuity

The same filter realization applied in the last chapter, can be used for coaxial filters.

The quasi-rectangular insert is also here approximated by a bow-tie shaped discon-

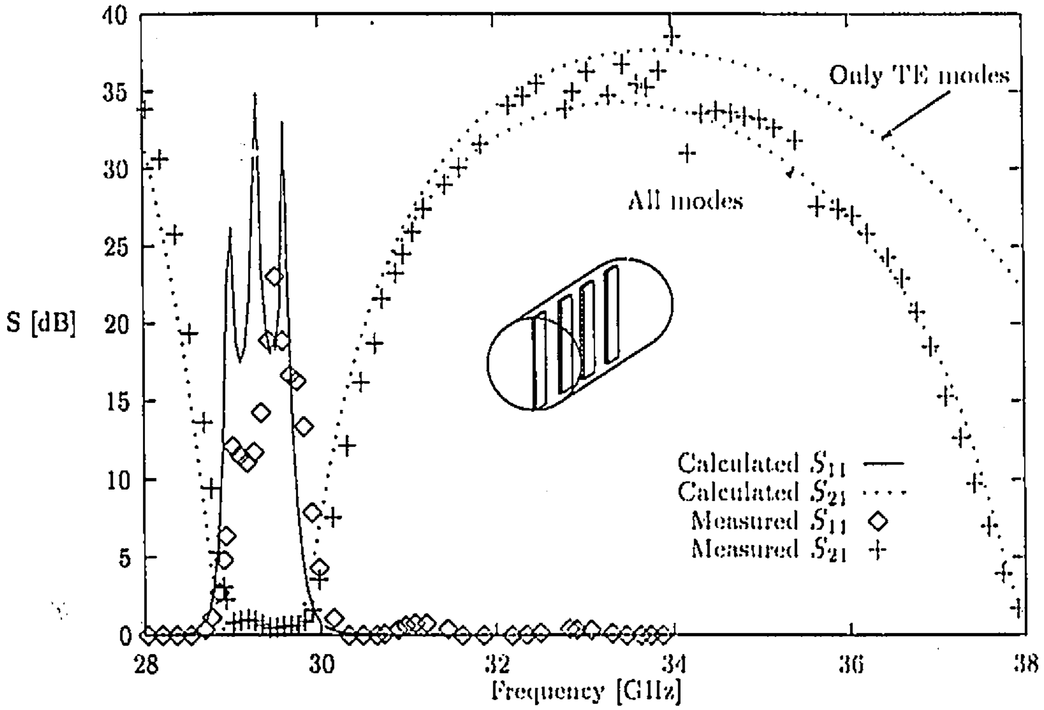

Figure 5.11: Performance versus frequency of a 3-resonator circular waveguide filter.

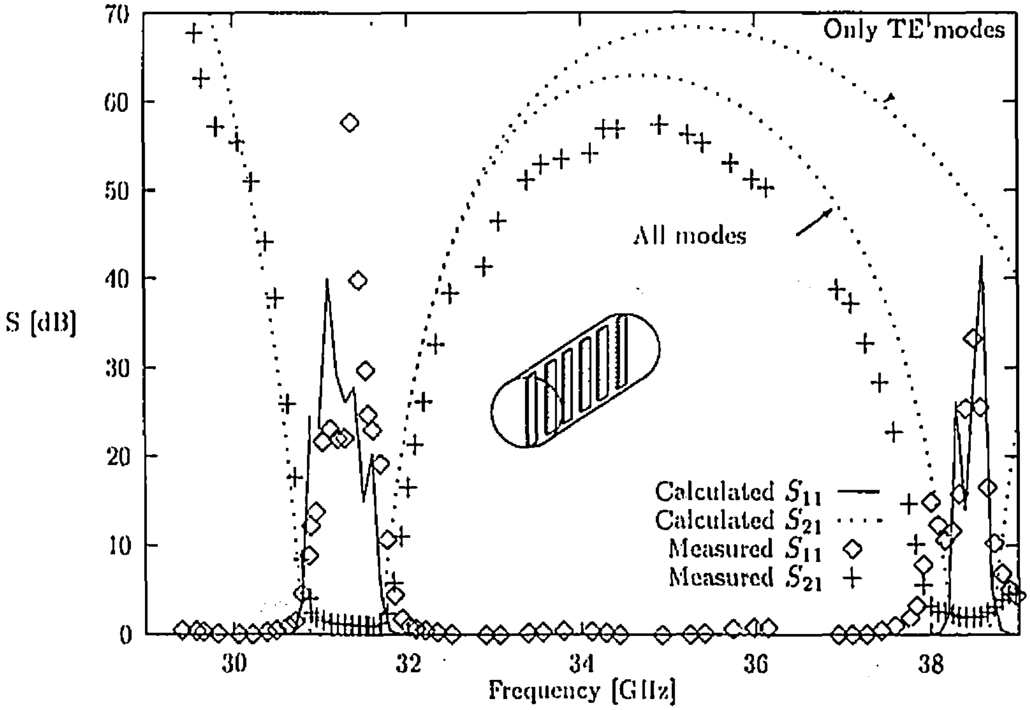

Figure 5.12: Performance versus frequency of a 5-resonator circular waveguide filter.

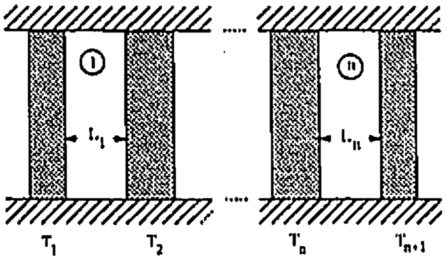

	Radius	f_0	Septum length [mm]			Resonator length [mm]		
n	[mm]	[GHz]	$T_1 = T_{n+1}$	$T_2 = T_n$	$T_3 = T_{n-1}$	$L_1 = L_n$	$L_2 = L_{n-1}$	L_3
3	4.000	29.22	0.844	2.985		5.683	5.768	
5	4.000	31.08	1.079	3.994	4.612	4.687	4.702	4.701

Table 5.1: Mechanical dimensions of the Ka-band three- and five-resonator circular waveguide filter.

tinuity (figure 5.13). The expression for the electromagnetic field in terms of normal modes and the analysis of the discontinuity follows the same steps as in the circular waveguide. Starting with the general field definition, equation (5.1)...(5.6), the E- and H-fields are expressed as functions of the potential Ψ which must satisfy the Helmholtz equation (5.7). Considering that the θ-boundary condition in the coax and in a circular waveguide are identical, the solutions of the θ-differential equation are:

$$\text{In the coaxial waveguide} \qquad \Phi^{(e,h)}(\theta) = \begin{cases} \sin(n\theta) \\ \cos(n\theta) \end{cases} \text{n integer}$$

$$\text{In the upper half waveguide} \qquad \Phi^{(e)}(\theta) = \sin(\nu(\theta - \gamma))$$

$$\Phi^{(h)}(\theta) = \cos(\nu(\theta - \gamma))$$

$$\text{In the lower half waveguide} \qquad \Phi^{(e)}(\theta) = \sin(\nu(\theta - \gamma - \pi))$$

$$\Phi^{(h)}(\theta) = \cos(\nu(\theta - \gamma - \pi))$$

with $\nu = n\pi / (\pi - 2\gamma)$.

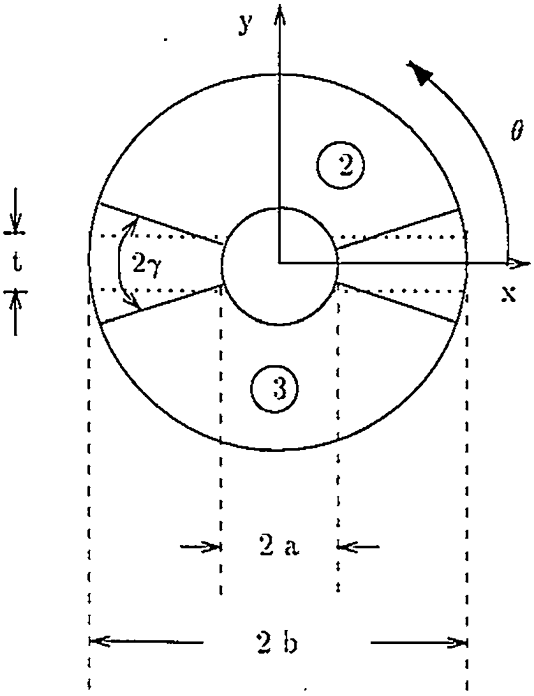

Figure 5.13: Metal insert discontinuity in a coax waveguide and its approximation by a bow-tie shaped discontinuity

The solution of the ρ-differential equation (5.9) is a sum of two Bessel functions. This is the only possibility to satisfy the boundary condition (4.8):

$$R(k\rho) = N_\nu(kb)J_\nu(k\rho) - J_\nu(kb)N_\nu(k\rho) \qquad \text{TM Modes}$$

$$R(k\rho) = N_\nu'(kb)J_\nu(k\rho) - J_\nu'(kb)N_\nu(k\rho) \qquad \text{TE Modes}$$

with $\nu = n\pi/(\pi - 2\gamma)$ in the upper or lower half waveguide and $\nu = n$ in the coaxial waveguide.

In comparison to the empty circular waveguide, the coaxial waveguide supports a TEM mode as well. The expression for the TEM wave is θ-independent and its R-function has already been described in equation (4.14).

The expression for the tangential E-field is the following:

$$\begin{aligned} \vec{E}_T \;=\; & -\frac{1}{\omega\varepsilon}\sum_{n=s}^{\infty}\sum_{m=s}^{\infty}\beta_{n,m}^{(e)}T_{n,m}^{(e)}\,(A_{n,m}+B_{n,m})\,\vec{e}_{n,m}^{(e)} \\ & -\sum_{p=0}^{\infty}\sum_{q=1}^{\infty}T_{p,q}^{(h)}\,(C_{p,q}+D_{p,q})\,\vec{e}_{p,q}^{(h)} \end{aligned} \tag{5.31}$$

where $\vec{e}^{\,(e,h)}$ denotes the orthogonal eigenfunctions. Their expression can be found in Appendix E. The parameter s is equal to 0 in the case of a coax waveguide and 1 in the case of a half coaxial waveguide to take in account the fact that the $TM_{0,m}$ mode does not exist in the latter one and to include the TEM mode (corresponding to the $TM_{0,0}$ mode).

Again the superscripts "s" and "c" in the coaxial waveguide describe the polarization of the E-field.

The tangential magnetic field is written as:

$$\vec{H}_T \;=\; \sum_{n=s}^{\infty}\sum_{m=1}^{\infty}T_{n,m}^{(e)}\,(A_{n,m}-B_{n,m})\,\vec{h}_{m,n}^{(e)}$$

$$+\frac{1}{\omega\mu}\sum_{p=0}^{\infty}\sum_{q=1}^{\infty}\beta_{p,q}^{(h)}T_{p,q}^{(h)}\left(C_{p,q}-D_{p,q}\right)\vec{h}_{p,q}^{(h)}$$

The definition of $\vec{h}_{m,n}^{(e)}$ and $\vec{h}_{p,q}^{(h)}$ are given in Appendix E.

In order to obtain the S-Matrix of the 3-port discontinuity, the tangential electric field is matched at the discontinuity, e.g. $z = 0$ (Fig. 5.13):

$$\left.\begin{array}{rcll} \vec{E}_T^{(1)} & = & \vec{E}_T^{(2)} & \theta \in [\gamma, \pi-\gamma] \\ & = & \vec{E}_T^{(3)} & \theta \in [\pi+\gamma, 2\pi-\gamma] \\ & = & 0 & \theta \in [0,\gamma], [\pi-\gamma, \pi+\gamma] \text{ and } [2\pi-\gamma, 2\pi] \end{array}\right\} \forall \rho \in [a,b] \qquad (5.32)$$

where the different $\vec{E}_T$ fields are defined in equation (5.31).

Following the same procedure defined in section 5.3 leads to the LE and LH matrices from which the three-port scattering matrix of the discontinuity can be derived.

The presence of the TEM mode makes a slight difference in the procedure which is presented here:

The first coupling equation is obtained by multiplying equation 5.32 by the TEM orthogonal function $\vec{e}_{0,0}^{(e1)}$ and by integrating over S_1:

$$\int_{S_1}\vec{E}_T^{(1)}.\vec{e}_{0,0}^{(e1)}w(\rho,\theta)dS = \int_{S_2}\vec{E}_T^{(2)}.\vec{e}_{0,0}^{(e1)}w(\rho,\theta)dS + \int_{S_3}\vec{E}_T^{(3)}.\vec{e}_{0,0}^{(e1)}w(\rho,\theta)dS$$

Using the orthogonal property of the eigenfunctions yields:

$$\begin{aligned} &\frac{1}{\omega\varepsilon_1}\beta_{0,0}^{(e1)}T_{0,0}^{(e1)}\left(A_{0,0}^{(1)}+B_{0,0}^{(1)}\right) = \\ &\quad \frac{1}{\omega\varepsilon_2}\sum_{n=1}^{\infty}\sum_{m=1}^{\infty}\beta_{n,m}^{(e2)}T_{n,m}^{(e2)}\left(A_{n,m}^{(2)}+B_{n,m}^{(2)}\right)\int_{\gamma}^{\pi-\gamma}\int_{0}^{b}\vec{e}_{n,m}^{(e2)}.\vec{e}_{0,0}^{(e1)}\rho d\rho d\theta \\ &\qquad +\sum_{p=0}^{\infty}\sum_{q=1}^{\infty}T_{p,q}^{(h2)}\left(C_{p,q}^{(2)}+D_{p,q}^{(2)}\right)\int_{\gamma}^{\pi-\gamma}\int_{0}^{b}\vec{e}_{p,q}^{(h2)}.\vec{e}_{0,0}^{(e1)}\rho d\rho d\theta \\ &+\frac{1}{\omega\varepsilon_3}\sum_{n=1}^{\infty}\sum_{m=1}^{\infty}\beta_{n,m}^{(e3)}T_{n,m}^{(e3)}\left(A_{n,m}^{(3)}+B_{n,m}^{(3)}\right)\int_{\pi+\gamma}^{2\pi-\gamma}\int_{0}^{b}\vec{e}_{n,m}^{(e3)}.\vec{e}_{0,0}^{(e1)}\rho d\rho d\theta \\ &\qquad +\sum_{p=0}^{\infty}\sum_{q=1}^{\infty}T_{p,q}^{(h3)}\left(C_{p,q}^{(3)}+D_{p,q}^{(3)}\right)\int_{\pi+\gamma}^{2\pi-\gamma}\int_{0}^{b}\vec{e}_{p,q}^{(h3)}.\vec{e}_{0,0}^{(e1)}\rho d\rho d\theta \end{aligned} \qquad (5.33)$$

The coefficients $A_{0,0}^{(1)}$ and $B_{0,0}^{(1)}$ have been expressed as a function of the sum of all eigenmodes in the upper or lower half guides. The next step is to calculate the coupling integrals:

1^{st} Coupling integral

The first coupling integral corresponds to the coupling between the TM modes in the upper half guide and the TEM modes in the coaxial waveguide. With $n : 1 \rightarrow \infty$:

$$CI_{01} = \int_{\gamma}^{\pi-\gamma} \int_{a}^{b} \vec{e}_{n,m}^{\,(e2)} . \vec{e}_{0,0}^{\,(e1)} \rho d\rho d\theta$$

This coupling integral is zero if n is even. For n odd:

$$CI_{01} = -\alpha_{n,m}^{(e2)} \alpha_{0,0}^{(e1)} \frac{2}{\nu} B_{\nu}^{(e2)}(k_{pn,m}^{(e2)} a)$$

2^{nd} Coupling integral

This coupling integral corresponds to the coupling between the TE modes in the upper half guide and the TEM modes in the coaxial waveguide. With $p : 0 \rightarrow \infty$:

$$CI_{02} = \int_{\gamma}^{\pi-\gamma} \int_{a}^{b} \vec{e}_{p,q}^{\,(h2)} . \vec{e}_{0,0}^{\,(e1)} \rho d\rho d\theta$$

this coupling integral is zero if p is even. For p odd:

$$CI_{02} = -2\alpha_{p,q}^{(h2)} \alpha_{0,0}^{(e1)} \int_{a}^{b} \frac{1}{\rho} B_{\nu}^{(h2)}(k_{pp,q}^{(h2)} \rho) d\rho$$

The third and fourth coupling integrals are computed from the integrals CI_{01} and CI_{02}. The ρ-coupling integrals do not change, contrary to the θ-integrals which are modified when $n - i$ is even and $n * i$ odd. In this case, the sign of the integral is inverted.

5.8 Bandpass filter

The filter structure is composed of a series of resonant cavities separated by coupling septa. Following the same procedure presented for the circular waveguide filter allows one to design a bandpass filter in a coaxial waveguide.

Figure 5.14 and 5.15 show the theoretical performance of a very narrow band five-resonator filter in X-band using a 4 mm radius coaxial waveguide. The corresponding data is given in Table 5.2. The computed insertion loss for the TEM mode is less than 0.1 dB in the passband (9.35-9.36 GHz) while the respective return loss is greater than 25 dB. The stopband rejection is more then 100 dB. The next passband is at 18.8 GHz which allows a stop band of 9.5 GHz between the two passbands (Fig. 5.14).

f_0 [GHz]	9.39		
Outer radius [mm]	4.000		
Inner radius [mm]	1.270		
Septum length [mm]	$L_1 = L_5$	$L_2 = L_4$	L_3
	15.870	15.920	15.99
Resonator length [mm]	$T_1 = T_6$	$T_2 = T_5$	$T_3 = T_4$
	0.110	0.210	0.285

Table 5.2: Mechanical dimensions of the five-resonator coaxial waveguide filter.

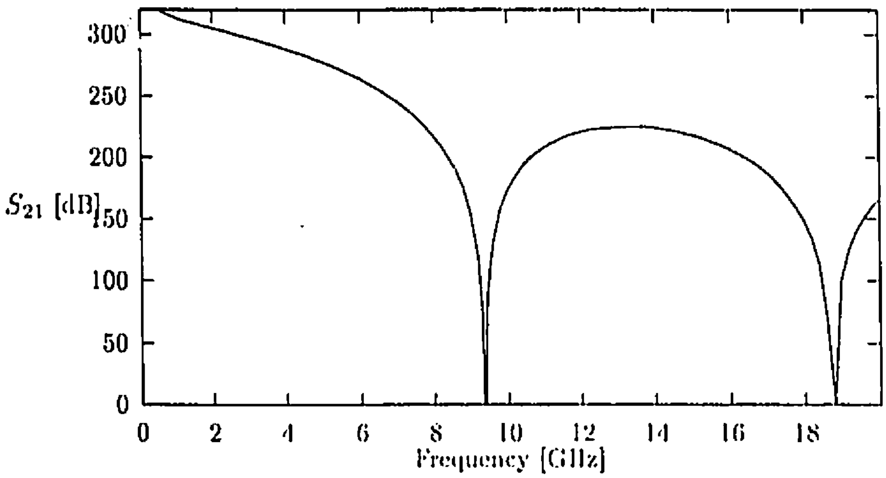

Figure 5.14: Performance versus frequency of a 5-resonator coaxial metal-insert waveguide filter.

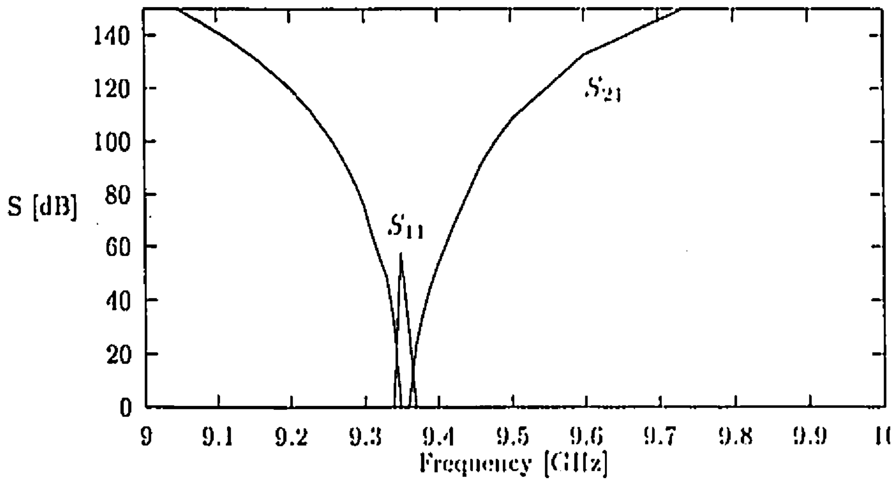

Figure 5.15: Expanded view of the 5-resonator coaxial metal-insert waveguide filter.

Chapter 6

Conclusion

The major objective of this thesis has been to develop an accurate numerical method to analyze and design filters and multiplexers for millimeter waves, in particular in a circular waveguide. This chapter completes this work by giving a conclusion and recommendation based on the experiences gained during this thesis. As well, suggestions are made regarding further work in this area of research.

6.1 Results

The major objective of this thesis has been to develop an efficient method for the analysis and design of waveguide filters and multiplexers at millimeter waves frequencies. The MMM applied to different kinds of discontinuities has shown its capability to analyze these different devices accurately without the aid of supercomputers. Furthermore, the analysis of most of the structures has been made by matching only two field components instead of four.

For example, in the parallel-connected diplexer configuration introduced in Chapter 1, the $\vec{\Psi}_x$ vector potential was sufficient to describe the electromagnetic field in the vicinity of an E-plane discontinuity, and only the matching of two field components (E_y

and H_x) is required. Therefore the numerical procedure resulting from this analysis is CPU time efficient and accurate.

The quadriplexer, introduced in Chapter 3, is an extension of the diplexer concept. Discontinuities involved in this quadriplexer require four field components to be matched. Chapter 3 has shown that, when there is no resonance at the discontinuity, the matching of two field components is sufficient to describe the discontinuity.

After characterizing selected discontinuities in rectangular waveguides, this thesis has focussed on coaxial transmission lines and transitions. The MMM has been applied to different kind of discontinuities, and results have been compared with the literature. Different bandpass filters have been designed, one using only steps in the inner conductor, the other one using gaps in the center conductors.

Chapter 5 introduced a circular waveguide metal-insert filter based on the metal-insert filter idea in rectangular waveguide. The metal insert has been approximated by a bow-tie shaped metal sheet instead of a rectangular sheet. Chapter 5 has shown that this approximation does not introduce a noticeable error in the measured frequency response. It was shown that as long as the operating frequency remains below the cut-off frequency of the TM_{01} mode, a TE mode approach is sufficient to analyze the discontinuity.

6.2 Further work

Most of the dual or multiple modes filters use a couple of resonant cavities separated by one or several irises. These irises provide the coupling between modes and allow the design of compact filters with very high Q-factor. The values of these coupling factors are obtained by approximation, and therefore tuning screws are necessary to compensate for the lack of design accuracy [58]. The rectangular irises used for the coupling in [59] and [60] (dotted lines in Fig. 6.1) could be replaced by semi-circular irises (solid lines in Fig. 6.1). In this case, the field analysis used in Chapter 5 can be applied and very accurate coupling factors can be calculated. With respect to fabrication, this semi-circular shape of the irises should not introduce any problems if etching techniques are used. However, in terms of accurate design (dual mode filters are very sensitive to the position and exact shape of the iris) the advantage is obvious.

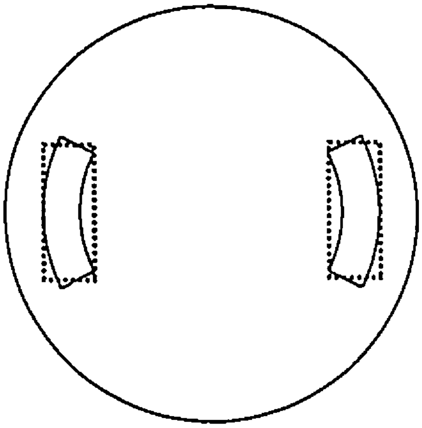

Figure 6.1: Circular waveguide iris used in multi-mode cavity filter.

The rectangular coaxial filter shown in Figure 6.2 could be an extension of the work presented in Chapter2. The analysis of such a filter should include both TE and TM modes and the TEM mode as well.

The grid-divider discontinuity presented briefly in Chapter 2 could be another possi-

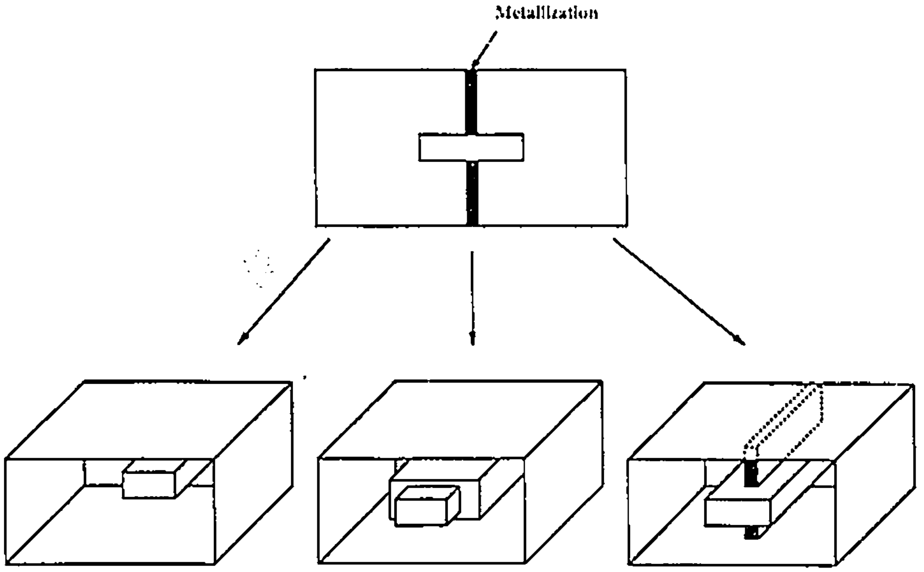

a) From rectangular waveguide to coaxial rectangular waveguide

b) Step in inner conductor in a coaxial rectangular waveguide

c) E-plane metallization in a coaxial reactangular waveguide

Figure 6.2: Metal-insert coaxial rectangular waveguide filter.

ble direction for further work by cascading it several times in order to obtain a squared waveguide filter for both polarization: an equivalence to the metal-insert filter but in two directions (Fig. 6.3.a). Following the same idea, but using a circular waveguide, a dual-polarization circular waveguide filter could be analyzed and designed (Fig. 6.3.b).

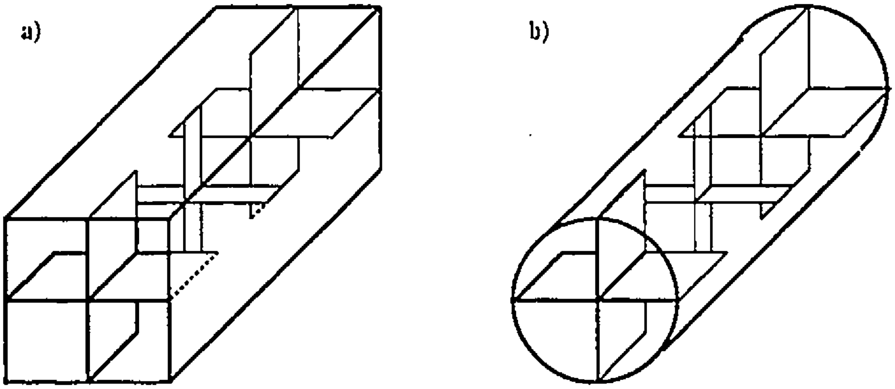

Figure 6.3: Dual-polarization metal-insert filter a) in rectangular waveguide b) in circular waveguide.

Appendix A

From the coupling matrices to the scattering matrix

This appendix describes how to obtain the S-matrices from the coupling equations which are:

$$A^{(2)} + B^{(2)} = LH\left(A^{(1)} + B^{(1)}\right)$$

and

$$A^{(1)} - B^{(1)} = LE\left(A^{(2)} - B^{(2)}\right)$$

The aim is to obtain the following two-port S-matrix :

$$\begin{pmatrix} B^{(1)} \\ A^{(2)} \end{pmatrix} = \begin{pmatrix} S_{11} & S_{12} \\ S_{21} & S_{22} \end{pmatrix} \begin{pmatrix} A^{(1)} \\ B^{(2)} \end{pmatrix}$$

The first step is to isolate $B^{(1)}$:

$$\begin{aligned} B^{(1)} &= A^{(1)} - LE.A^{(2)} + LE.B^{(2)} \\ &= A^{(1)} - LE\left(LH.A^{(1)} + LH.B^{(1)} - B^{(2)}\right) + LE.B^{(2)} \end{aligned}$$

Then

$$(I_d + LE.LH)\,B^{(1)} = (I_d - LE.LH)\,A^{(1)} + 2LE.B^{(2)}$$

where I_d represents the identity matrix. Therefore, the expression of S_{11} and S_{12} are:

$$S_{11} = (I_d + LE.LH)^{-1}(I_d - LE.LH) \tag{A.1}$$

$$S_{12} = 2(I_d + LE.LH)^{-1}LE \tag{A.2}$$

From the second coupling equation :

$$\begin{aligned} A^{(2)} &= LH.A^{(1)} + LH.B^{(1)} - B^{(2)} \\ &= LH.A^{(1)} + LH.\left(S_{11}.A^{(1)} + S_{12}.B^{(2)}\right) - B^{(2)} \\ &= LH.(I_d + S_{11})A^{(1)} + (LH.S_{12} - I_d)B^{(2)} \end{aligned}$$

Therefore, S_{21} and S_{22} are expressed in terms of LH, S_{11} and S_{12}:

$$S_{21} = LH(I_d + S_{11}) \tag{A.3}$$

$$S_{22} = LH.S_{12} - I_d \tag{A.4}$$

Appendix B

Field components in coaxial waveguides

- *TM* field

$$
\begin{aligned}
H_\rho &= \frac{1}{\rho}\frac{\partial \Psi^{(e)}}{\partial \theta} & \qquad E_\rho &= \frac{1}{j\omega\epsilon}\frac{\partial^2 \Psi^{(e)}}{\partial\rho\partial z} \\
H_\theta &= -\frac{\partial \Psi^{(e)}}{\partial \rho} & \qquad E_\theta &= \frac{1}{j\omega\epsilon\rho}\frac{\partial^2 \Psi^{(e)}}{\partial\theta\partial z} \\
H_z &= \quad 0 & \qquad E_z &= \frac{1}{j\omega\epsilon}\left(\frac{\partial^2}{\partial z^2} + k^2\right)\Psi^{(e)}
\end{aligned}
$$

- *TE* field

$$
\begin{aligned}
E_\rho &= -\frac{1}{\rho}\frac{\partial \Psi^{(h)}}{\partial \theta} & \qquad H_\rho &= \frac{1}{j\omega\mu}\frac{\partial^2 \Psi^{(h)}}{\partial\rho\partial z} \\
E_\theta &= \quad \frac{\partial \Psi^{(h)}}{\partial \rho} & \qquad H_\theta &= \frac{1}{j\omega\mu\rho}\frac{\partial^2 \Psi^{(h)}}{\partial\theta\partial z} \\
E_z &= \quad 0 & \qquad H_z &= \frac{1}{j\omega\mu}\left(\frac{\partial^2}{\partial z^2} + k^2\right)\Psi^{(h)}
\end{aligned}
$$

Appendix C

Field expressions in circular waveguides

C.1 Empty circular waveguide

The eigenfunctions related to the E-field in the empty circular waveguide are:

TM mode (at z=0) :

$$\vec{e}^{(c)}_{n,m} = \alpha^{(c)}_{n,m}\left[\left\{\begin{array}{c}\sin(n\theta)\\ \cos(n\theta)\end{array}\right\}\frac{dJ_n(k^{(c)}_{\rho n,m}\rho)}{d\rho}\vec{\rho}+\frac{n}{\rho}\left\{\begin{array}{c}\cos(n\theta)\\ -\sin(n\theta)\end{array}\right\}J_n(k^{(c)}_{\rho n,m}\rho)\vec{\theta}\right] \qquad \text{(C.1)}$$

TE mode (at z=0) :

$$\vec{e}^{(h)}_{p,q} = \alpha^{(h)}_{p,q}\left[-\frac{p}{\rho}\left\{\begin{array}{c}\sin(p\theta)\\ -\cos(p\theta)\end{array}\right\}J_p(k^{(h)}_{\rho p,q}\rho)\vec{\rho}-\left\{\begin{array}{c}\cos(p\theta)\\ \sin(p\theta)\end{array}\right\}\frac{dJ_p(k^{(h)}_{\rho p,q}\rho)}{d\rho}\vec{\theta}\right] \qquad \text{(C.2)}$$

In this waveguide, any modes can be decomposed into two orthogonal modes. The first type of mode is assigned the superscript "s" and denotes the mode with the E-field perpendicular to the septum. The second one is marked with the superscript "c" and denotes the modes with the E-field parallel to the septum. However, the TM_{0m} mode exists only in "c"-mode. On the other hand, the TE_{0q} mode exists only in "s"-mode.

C.2 Upper half circular waveguide

The eigenfunctions related to the E-field in the upper half circular waveguide are:

TM mode (at z=0) :

$$\vec{e}^{(e)}_{n,m} = \alpha^{(e)}_{n,m}\left[\sin(\nu(\theta-\gamma))\frac{dJ_\nu(k^{(e)}_{pn,m}\rho)}{d\rho}\vec{\rho} + \frac{\nu}{\rho}\cos(\nu(\theta-\gamma))J_\nu(k^{(e)}_{pn,m}\rho)\vec{\theta}\right] \qquad \text{(C.3)}$$

TE mode (at z=0) :

$$\vec{e}^{(h)}_{p,q} = \alpha^{(h)}_{p,q}\left[-\frac{\nu}{\rho}\sin(\nu(\theta-\gamma))J_\nu(k^{(h)}_{pp,q}\rho)\vec{\rho} - \cos(\nu(\theta-\gamma))\frac{dJ_\nu(k^{(h)}_{pp,q}\rho)}{d\rho}\vec{\theta}\right] \qquad \text{(C.4)}$$

The lower guide field expressions are obtained by replacing all the angular variables by $\nu(\theta-\gamma-\pi)$.

C.3 Ortho-normalization coefficients

The ortho-normalization coefficient α is computed by using the following integral over the appropriate waveguide cross-section S:

$$\alpha^{(c,h)}_{n,m} = \left[\int\int_S \vec{e}^{(c,h)}_{n,m}\vec{e}^{(c,h)}_{n,m}\rho d\rho d\theta\right]^{-0.5} \qquad \text{(C.5)}$$

This leads for the empty circular waveguide (with an integration performed over $[0,2\pi]$ for θ and $[0,b]$ for ρ) to:

$\alpha^{(c,h)-1}_{n,m}$	TM Mode	TE Mode
$n \neq 0$	$\sqrt{\pi}K_cJ'_n(K_c)/\sqrt{2}$	$\sqrt{\pi}\sqrt{K_h^2 - n^2}J_n(K_h)/\sqrt{2}$
$n = 0$	$\sqrt{\pi}K_cJ_1(K_cb)$	$\sqrt{\pi}K_hJ_0(K_hb)$

where $K_h = k^{(h)}_{pn,m}b$ and $K_c = k^{(c)}_{pn,m}b$ (valid also for the next table). For the upper half circular waveguide, the integral is computed over $[\gamma,\pi-\gamma]$ (instead of $[0,2\pi]$). Therefore, the α coefficients are slightly different.

$\alpha_{n,m}^{(e,h)-1}$	TM Mode	TE Mode
$n \neq 0$	$\sqrt{\pi - 2\gamma} K_e J'_\nu(K_e)/2$	$\sqrt{\pi - 2\gamma}\sqrt{K_h^2 - \nu^2} J_\nu(K_h)/2$
$n = 0$	Does not exist	$\sqrt{\pi - 2\gamma} K_h J_0(K_h)/\sqrt{2}$

These results do not change when considering the upper half guide or the lower half guide.

C.4 Magnetic field

The eigenfunctions related to the magnetic field in the empty circular waveguide are:

TM mode (at z=0) :

$$\vec{h}_{n,m}^{(e)} = \alpha_{n,m}^{(e)} \left[\frac{n}{\rho} \left\{ \begin{array}{c} \cos(n\theta) \\ -\sin(n\theta) \end{array} \right\} J_n(k_{\rho n,m}^{(e)}\rho)\vec{\rho} - \left\{ \begin{array}{c} \sin(n\theta) \\ \cos(n\theta) \end{array} \right\} \frac{dJ_n(k_{\rho n,m}^{(e)}\rho)}{d\rho}\vec{\theta} \right]$$

TE mode (at z=0) :

$$\vec{h}_{p,q}^{(h)} = -\alpha_{p,q}^{(h)} \left[\left\{ \begin{array}{c} \sin(p\theta) \\ \cos(p\theta) \end{array} \right\} \frac{dJ_p(k_{\rho p,q}^{(h)}\rho)}{d\rho}\vec{\rho} + \frac{p}{\rho} \left\{ \begin{array}{c} \cos(p\theta) \\ -\sin(p\theta) \end{array} \right\} J_p(k_{\rho p,q}^{(h)}\rho)\vec{\theta} \right]$$

and in the upper half guide:

TM mode (at z=0) :

$$\vec{h}_{n,m}^{(e)} = \alpha_{n,m}^{(e)} \left[\frac{\nu}{\rho} \cos(\nu(\theta - \gamma)) J_\nu(k_{\rho n,m}^{(e)}\rho)\vec{\rho} - \sin(\nu(\theta - \gamma)) \frac{dJ_\nu(k_{\rho n,m}^{(e)}\rho)}{d\rho}\vec{\theta} \right]$$

TE mode (at z=0) :

$$\vec{h}_{p,q}^{(h)} = -\alpha_{p,q}^{(h)} \left[\sin(\nu(\theta - \gamma)) \frac{dJ_\nu(k_{\rho p,q}^{(h)}\rho)}{d\rho}\vec{\rho} + \frac{\nu}{\rho} \cos(\nu(\theta - \gamma)) J_\nu(k_{\rho p,q}^{(h)}\rho)\vec{\theta} \right]$$

C.5 Normalization coefficient

This coefficient is obtained by computing the following integral:

$$P = \frac{1}{2} Re \left\{ \int_S (\vec{E} \times \vec{H}^*).\vec{dS} \right\} = \frac{1}{2} Re \left\{ \int_S E_\rho H_\theta^* - E_\theta H_\rho^*)\vec{z}.\vec{dS} \right\}$$

For any type of guide, e.g. empty, upper half or lower half waveguide, solving this integral leads to:

$$T^{(e)}_{n,m} = \sqrt{\frac{2\omega\epsilon}{\beta^{(e)}_{n,m}}} \qquad \text{for the TM modes} \tag{C.6}$$

and

$$T^{(h)}_{n,m} = \sqrt{\frac{2\omega\mu}{\beta^{(h)*}_{n,m}}} \qquad \text{for the TE modes} \tag{C.7}$$

Appendix D

Coupling integrals

D.1 Second coupling equation

The second coupling equation is the matching equation (5.12) multiplied by $\vec{e}_{i,j}^{(c1c)}$ and integrated over the empty guide section:

$$\int_{S_1} \vec{E}_T^{(1)}.\vec{e}_{i,j}^{(c1c)} w(\rho,\theta) dS = \int_{S_2} \vec{E}_T^{(2)}.\vec{e}_{i,j}^{(c1c)} w(\rho,\theta) dS + \int_{S_3} \vec{E}_T^{(3)}.\vec{e}_{i,j}^{(c1c)} w(\rho,\theta) dS$$

Expressing the tangential fields $\vec{E}_T^{(1)}$, $\vec{E}_T^{(2)}$ and $\vec{E}_T^{(3)}$:

$$\begin{aligned} \int_{S_1} \Bigg[-\frac{1}{\omega c_1} \sum_{n=1}^{\infty} \sum_{m=1}^{\infty} E_{nm}^{(c1s)} \vec{e}_{nm}^{(c1s)} \quad - \quad \frac{1}{\omega c_1} \sum_{n=0}^{\infty} \sum_{m=1}^{\infty} E_{nm}^{(c1c)} \vec{e}_{nm}^{(c1c)} \\ - \sum_{p=0}^{\infty} \sum_{q=1}^{\infty} E_{pq}^{(h1s)} \vec{e}_{pq}^{(h1s)} \quad - \quad \sum_{p=0}^{\infty} \sum_{q=1}^{\infty} E_{pq}^{(h1c)} \vec{e}_{pq}^{(h1c)} \Bigg] .\vec{e}_{ij}^{(c1c)} \rho d\rho d\theta \end{aligned}$$

$$\begin{aligned} = \int_{S_2} \Bigg[-\frac{1}{\omega c_2} \sum_{n=1}^{\infty} \sum_{m=1}^{\infty} E_{nm}^{(c2)} \vec{e}_{nm}^{(c2)} - \sum_{p=0}^{\infty} \sum_{q=1}^{\infty} E_{pq}^{(h2)} \vec{e}_{pq}^{(h2)} \Bigg] .\vec{e}_{ij}^{(c1c)} \rho d\rho d\theta \\ + \int_{S_3} \Bigg[-\frac{1}{\omega c_3} \sum_{n=1}^{\infty} \sum_{m=1}^{\infty} E_{nm}^{(c3)} \vec{e}_{nm}^{(c3)} - \sum_{p=0}^{\infty} \sum_{q=1}^{\infty} E_{pq}^{(h3)} \vec{e}_{pq}^{(h3)} \Bigg] .\vec{e}_{ij}^{(c1c)} \rho d\rho d\theta \end{aligned}$$

where $E_{mn}^{(c1s)}$, $E_{mn}^{(c1c)}$, $E_{pq}^{(h1s)}$ and $E_{pq}^{(h1c)}$ have been defined in section 5.3.1 as well as $E_{mn}^{(c2)}$, $E_{pq}^{(h2)}$, $E_{mn}^{(c3)}$ and $E_{pq}^{(h3)}$. However, by using the orthonormal property on the LHS of the equation, it is possible to write:

$$\begin{aligned}
&\frac{1}{\omega\epsilon_1}\beta^{(c1)}_{i,j}T^{(c1)}_{i,j}\left(A^{(1c)}_{i,j}+B^{(1c)}_{i,j}\right) = \\
&\quad \frac{1}{\omega\epsilon_2}\sum_{n=1}^{\infty}\sum_{m=1}^{\infty}\beta^{(c2)}_{n,m}T^{(c2)}_{n,m}\left(A^{(2)}_{n,m}+B^{(2)}_{n,m}\right)\int_{\gamma}^{\pi-\gamma}\int_0^b \vec{e}^{(c2)}_{n,m}.\vec{e}^{(c1c)}_{i,j}\rho d\rho d\theta \\
&\qquad +\sum_{p=0}^{\infty}\sum_{q=1}^{\infty}T^{(h2)}_{p,q}\left(C^{(2)}_{p,q}+D^{(2)}_{p,q}\right)\int_{\gamma}^{\pi-\gamma}\int_0^b \vec{e}^{(h2)}_{p,q}.\vec{e}^{(c1c)}_{i,j}\rho d\rho d\theta \\
&\quad +\frac{1}{\omega\epsilon_3}\sum_{n=1}^{\infty}\sum_{m=1}^{\infty}\beta^{(c3)}_{n,m}T^{(c3)}_{n,m}\left(A^{(3)}_{n,m}+B^{(3)}_{n,m}\right)\int_{\pi+\gamma}^{2\pi-\gamma}\int_0^b \vec{e}^{(c3)}_{n,m}.\vec{e}^{(c1c)}_{i,j}\rho d\rho d\theta \\
&\qquad +\sum_{p=0}^{\infty}\sum_{q=1}^{\infty}T^{(h3)}_{p,q}\left(C^{(3)}_{p,q}+D^{(3)}_{p,q}\right)\int_{\pi+\gamma}^{2\pi-\gamma}\int_0^b \vec{e}^{(h3)}_{p,q}.\vec{e}^{(c1c)}_{i,j}\rho d\rho d\theta
\end{aligned}$$

The equation can be rewritten in term of matrices:

$$\begin{aligned}
A^{(1c)}+B^{(1c)} &= LH^{(c1c)}\left(A^{(2)}+B^{(2)}\right)+LH^{(c2c)}\left(C^{(2)}+D^{(2)}\right)+ \\
&\quad LH^{(c3c)}\left(A^{(3)}+B^{(3)}\right)+LH^{(c4c)}\left(C^{(3)}+D^{(3)}\right) \qquad \text{(D.1)}
\end{aligned}$$

1st Coupling integral

The first coupling integral is, for $n : 1 — \infty$ and $i : 0 — \infty$:

$$\begin{aligned}
CI^c_1 &= \int_{\gamma}^{\pi-\gamma}\int_0^b \vec{e}^{(c2)}_{n,m}.\vec{e}^{(c1c)}_{i,j}\rho d\rho d\theta \\
&= \alpha^{(c2)}_{n,m}\alpha^{(c1c)}_{i,j}\int_{\gamma}^{\pi-\gamma}\sin(\nu(\theta-\gamma))\cos(i\theta)d\theta\int_0^b \frac{dJ_n(k^{(c2)}_{\rho n,m}\rho)}{d\rho}\frac{dJ_i(k^{(c1c)}_{\rho i,j}\rho)}{d\rho}\rho d\rho - \\
&\quad \alpha^{(c2)}_{n,m}\alpha^{(c1c)}_{i,j}\int_{\gamma}^{\pi-\gamma}\cos(\nu(\theta-\gamma))\sin(i\theta)d\theta\int_0^b \frac{\nu i}{\rho^2}J_n(k^{(c2)}_{\rho n,m}\rho)J_i(k^{(c1c)}_{\rho i,j}\rho)\rho d\rho
\end{aligned}$$

The θ-coupling integrals are expressed in Appendix E. The coupling integral CI^c_1 is 0 if $n-i$ is even. For $n-i$ odd:

$$CI^c_1 = \alpha^{(c2)}_{n,m}\alpha^{(c1c)}_{i,j}\frac{2\nu\cos(i\gamma)}{\nu^2-i^2}\int_0^b \frac{dJ_\nu(k^{(c2)}_{\rho n,m}\rho)}{d\rho}\frac{dJ_i(k^{(c1)}_{\rho i,j}\rho)}{d\rho}+\frac{i^2}{\rho^2}J_\nu(k^{(c2)}_{\rho n,m}\rho)J_i(k^{(c1)}_{\rho i,j}\rho)\rho d\rho$$

2nd Coupling integral

This coupling integral corresponds to the coupling between the TE modes in the upper half guide and the TM^c modes in the circular waveguide. With $p : 0 \rightarrow \infty$ and $i : 0 \rightarrow \infty$:

$$\begin{aligned}
CI_2^c &= \int_{\gamma}^{\pi-\gamma} \int_0^b \vec{e}_{p,q}^{\,(h2)} . \vec{e}_{i,j}^{\,(c1c)} \rho d\rho d\theta \\
&= -\alpha_{p,q}^{(h2)} \alpha_{i,j}^{(c1c)} \nu \int_{\gamma}^{\pi-\gamma} \sin(\nu(\theta-\gamma)) \cos(i\theta) d\theta \int_0^b J_\nu(k_{\rho p,q}^{(h2)} \rho \frac{dJ_i(k_{\rho i,j}^{(c1c)} \rho)}{d\rho} d\rho \; + \\
& \quad \alpha_{p,q}^{(h2)} \alpha_{i,j}^{(c1c)} i \int_{\gamma}^{\pi-\gamma} \cos \nu(\theta-\gamma)) \sin(i\theta) d\theta \int_0^b \frac{dJ_\nu(k_{\rho p,q}^{(h2)} \rho)}{d\rho} J_i(k_{\rho i,j}^{(c1c)} \rho) d\rho
\end{aligned}$$

As shown previously, the θ-integrals are equal to zero if $p - i$ even. In the $p - i$ odd case, the integral becomes:

$$\begin{aligned}
CI_2^c &= -\alpha_{p,q}^{(h2)} \alpha_{i,j}^{(c1c)} \frac{2\cos(i\gamma)}{\nu^2 - i^2} \\
& \quad \int_0^b \nu^2 J_\nu(k_{\rho p,q}^{(h2)} \rho) \frac{dJ_i(k_{\rho i,j}^{(c1c)} \rho)}{d\rho} + i^2 \frac{dJ_\nu(k_{\rho p,q}^{(h2)} \rho)}{d\rho} J_i(k_{\rho i,j}^{(c1c)} \rho) d\rho
\end{aligned}$$

The third and fourth coupling integrals are computed from the coupling integrals CI_1^c and CI_2^c. The ρ-coupling integrals do not change, contrary to the θ-ones which are computed over $[\pi + \gamma, 2\pi - \gamma]$. Their values are simply multiplied by -1 if $i - n$ is odd with n even (e.g. i odd).

D.2 Third coupling equation

After multiplying with the TE^s orthogonal function of the TE mode, the E-field matching equation becomes:

$$\int_{S_1} \vec{E}_T^{(1)} . \vec{e}_{i,j}^{\,(h1s)} w(\rho,\theta) dS = \int_{S_2} \vec{E}_T^{(2)} . \vec{e}_{i,j}^{\,(h1s)} w(\rho,\theta) dS + \int_{S_3} \vec{E}_T^{(3)} . \vec{e}_{i,j}^{\,(h1s)} w(\rho,\theta) dS$$

$$\begin{aligned}
\int_{S_1} \Bigg[-\frac{1}{\omega c_1} \sum_{n=1}^{\infty} \sum_{m=1}^{\infty} E_{nm}^{(c1s)} \vec{e}_{nm}^{\,(h1s)} \; &- \; \frac{1}{\omega c_1} \sum_{n=0}^{\infty} \sum_{m=1}^{\infty} E_{nm}^{(c1c)} \vec{e}_{nm}^{\,(c1c)} \\
- \sum_{p=0}^{\infty} \sum_{q=1}^{\infty} E_{pq}^{(h1s)} \vec{e}_{pq}^{\,(h1s)} \; &- \; \sum_{p=0}^{\infty} \sum_{q=1}^{\infty} E_{pq}^{(h1c)} \vec{e}_{pq}^{\,(h1c)} \Bigg] . \vec{e}_{ij}^{\,(c1c)} \rho d\rho d\theta
\end{aligned}$$

$$= \int_{S_2}\left[-\frac{1}{\omega c_2}\sum_{n=1}^{\infty}\sum_{m=1}^{\infty} E_{nm}^{(c2)}\vec{e}_{nm}^{(c2)} - \sum_{p=0}^{\infty}\sum_{q=1}^{\infty} E_{pq}^{(h2)}\vec{e}_{pq}^{(h2)}\right].\vec{e}_{ij}^{(h1s)}\rho d\rho d\theta$$
$$+ \int_{S_3}\left[-\frac{1}{\omega c_3}\sum_{n=1}^{\infty}\sum_{m=1}^{\infty} E_{nm}^{(c3)}\vec{e}_{nm}^{(c3)} - \sum_{p=0}^{\infty}\sum_{q=1}^{\infty} E_{pq}^{(h3)}\vec{e}_{pq}^{(h3)}\right].\vec{e}_{ij}^{(h1s)}\rho d\rho d\theta$$

where $E_{mn}^{(c1s)}$, $E_{mn}^{(c1c)}$, $E_{pq}^{(h1s)}$ and $E_{pq}^{(h1c)}$ have been defined in equations (5.14-5.19) as well as $E_{mn}^{(c2)}$, $E_{pq}^{(h2)}$, $E_{mn}^{(c3)}$ and $E_{pq}^{(h3)}$. Applying the orthogonality property of modes, this equation can be written as:

$$T_{i,j}^{(h1s)}\left(C_{i,j}^{(1s)} + D_{i,j}^{(1s)}\right) =$$
$$\frac{1}{\omega c_2}\sum_{n=1}^{\infty}\sum_{m=1}^{\infty}\beta_{n,m}^{(c2)}T_{n,m}^{(c2)}\left(A_{n,m}^{(2)} + B_{n,m}^{(2)}\right)\int_{\gamma}^{\pi-\gamma}\int_{0}^{b}\vec{e}_{n,m}^{(c2)}.\vec{e}_{i,j}^{(h1s)}\rho d\rho d\theta$$
$$+\sum_{p=0}^{\infty}\sum_{q=1}^{\infty}T_{p,q}^{(h2)}\left(C_{p,q}^{(2)} + D_{p,q}^{(2)}\right)\int_{\gamma}^{\pi-\gamma}\int_{0}^{b}\vec{e}_{p,q}^{(h2)}.\vec{e}_{i,j}^{(h1s)}\rho d\rho d\theta$$
$$+\frac{1}{\omega c_3}\sum_{n=1}^{\infty}\sum_{m=1}^{\infty}\beta_{n,m}^{(c3)}T_{n,m}^{(c3)}\left(A_{n,m}^{(3)} + B_{n,m}^{(3)}\right)\int_{\pi+\gamma}^{2\pi-\gamma}\int_{0}^{b}\vec{e}_{n,m}^{(c3)}.\vec{e}_{i,j}^{(h1s)}\rho d\rho d\theta$$
$$+\sum_{p=0}^{\infty}\sum_{q=1}^{\infty}T_{p,q}^{(h3)}\left(C_{p,q}^{(3)} + D_{p,q}^{(3)}\right)\int_{\pi+\gamma}^{2\pi-\gamma}\int_{0}^{b}\vec{e}_{p,q}^{(h3)}.\vec{e}_{i,j}^{(h1s)}\rho d\rho d\theta$$

In terms of matrices:

$$C^{(1s)} + D^{(1s)} = LH^{(h1s)}\left(A^{(2)} + B^{(2)}\right) + LH^{(h2s)}\left(C^{(2)} + D^{(2)}\right) \quad (D.2)$$
$$LH^{(h3s)}\left(A^{(3)} + B^{(3)}\right) + LH^{(h4s)}\left(C^{(3)} + D^{(3)}\right) \quad (D.3)$$

1^{st} Coupling integral

The first coupling integral is ($n : 1 \rightarrow \infty$ and $i : 0 - \infty$):

$$CI_3^s = \int_{\gamma}^{\pi-\gamma}\int_{0}^{b}\vec{e}_{n,m}^{(c2)}.\vec{e}_{i,j}^{(h1s)}\rho d\rho d\theta$$
$$= -\alpha_{n,m}^{(c2)}\alpha_{i,j}^{(h1s)} i\int_{\gamma}^{\pi-\gamma}\sin(\nu(\theta-\gamma))\sin(i\theta)d\theta\int_{0}^{b}\frac{dJ_\nu(k_{\rho n,m}^{(c2)}\rho)}{d\rho}J_i(k_{\rho i,j}^{(h1s)}\rho)d\rho$$
$$-\alpha_{n,m}^{(c2)}\alpha_{i,j}^{(h1s)}\nu\int_{\gamma}^{\pi-\gamma}\cos(\nu(\theta-\gamma))\cos(i\theta)d\theta\int_{0}^{b}J_\nu(k_{\rho n,m}^{(c2)}\rho)\frac{dJ_i(k_{\rho i,j}^{(h1s)}\rho)}{d\rho}d\rho$$

The θ-integrals are again equal to zero if $n-i$ is odd. The $n-i$ even case can be written as :

$$\begin{aligned}
CI_3^s &= -\alpha_{n,m}^{(c2)}\alpha_{i,j}^{(h1s)}\frac{2i\nu\sin(i\gamma)}{\nu^2-i^2} \\
&\quad \int_0^b \frac{dJ_\nu(k_{pn,m}^{(c2)}\rho)}{d\rho}J_i(k_{pi,j}^{(h1s)}\rho)+J_\nu(k_{pn,m}^{(c2)}\rho)\frac{dJ_i(k_{pi,j}^{(h1s)}\rho)}{d\rho}d\rho \\
&= -\alpha_{n,m}^{(c2)}\alpha_{i,j}^{(h1s)}\frac{2i\nu\sin(i\gamma)}{\nu^2-i^2}\int_0^b\frac{d}{d\rho}\left[J_\nu(k_{pn,m}^{(c2)}\rho)J_i(k_{pi,j}^{(h1s)}\rho)\right]d\rho \\
&= -\alpha_{n,m}^{(c2)}\alpha_{i,j}^{(h1s)}\frac{2i\nu\sin(i\gamma)}{\nu^2-i^2}\left[J_\nu(k_{pn,m}^{(c2)}\rho)J_i(k_{pi,j}^{(h1s)}\rho)\right]_0^b = 0
\end{aligned}$$

which means that $CI_3^s = 0, \forall\ i,\ j,\ n$ and m.

<u>2^{nd} Coupling integral</u>

The second coupling integral is (with $p : 0 - \infty$ and $i : 0 - \infty$):

$$\begin{aligned}
CI_4^s &= \int_\gamma^{\pi-\gamma}\int_0^b \vec{e}_{p,q}^{(h2)}.\vec{e}_{i,j}^{(h1s)}\rho d\rho d\theta \\
&= \alpha_{p,q}^{(h2)}\alpha_{i,j}^{(h1)}\int_\gamma^{\pi-\gamma}\sin(\nu(\theta-\gamma))\sin(i\theta)d\theta\int_0^b\frac{i\nu}{\rho^2}J_\nu(k_{pp,q}^{(h2)}\rho)J_i(k_{pi,j}^{(h1s)}\rho)\rho d\rho \ + \\
&\quad \alpha_{p,q}^{(h2)}\alpha_{i,j}^{(h1)}\int_\gamma^{\pi-\gamma}\cos(\nu(\theta-\gamma))\cos(i\theta)d\theta\int_0^b\frac{dJ_\nu(k_{pp,q}^{(h2)}\rho)}{d\rho}\frac{dJ_i(k_{pi,j}^{(h1s)}\rho)}{d\rho}\rho d\rho
\end{aligned}$$

Three cases must be distinguished:

a) $p-i$ odd:

$$CI_4^s = 0$$

b)$p-i$ even and $p^2+i^2 \neq 0$:

$$\begin{aligned}
CI_4^s &= \alpha_{p,q}^{(h2)}\alpha_{i,j}^{(h1s)}\frac{2i\sin(i\gamma)}{\nu^2-i^2} \\
&\quad \int_0^b\left(\frac{\nu^2}{\rho^2}J_\nu(k_{pp,q}^{(h2)}\rho)J_i(k_{pi,j}^{(h1s)}\rho)+\frac{dJ_\nu(k_{pp,q}^{(h2)}\rho)}{d\rho}\frac{dJ_i(k_{pi,j}^{(h1s)}\rho)}{d\rho}\right)\rho d\rho
\end{aligned}$$

c)$p = i = 0$

$$CI_4^s = \alpha_{0,q}^{(h2)}\alpha_{0,j}^{(h1s)}(\pi - 2\gamma)\int_0^b \frac{dJ_0(k_{\rho 0,q}^{(h2)}\rho)}{d\rho}\frac{dJ_0(k_{\rho 0,j}^{(h1s)}\rho)}{d\rho}\rho d\rho$$

Like CI_3^s, the third coupling integral is zero. The fourth coupling integral can be computed from the coupling integral CI_4^s. The ρ-coupling integrals do not change, like the θ-integrals, because for $i = n$, the $\theta/2$ coefficient does not vary if computed over $[\gamma, \pi - \gamma]$ or $[\pi + \gamma, 2\pi - \gamma]$. The matrix equation (Equ. D.3) can, therefore, be simplified ($LH^{(h1s)} = 0$ and $LH^{(h3s)} = 0$):

$$C^{(1s)} + D^{(1s)} = LH^{(h2s)}\left(C^{(2)} + D^{(2)}\right) + LH^{(h4s)}\left(C^{(3)} + D^{(3)}\right) \tag{D.4}$$

D.3 Fourth coupling equation

The fourth coupling equation is the matching equation (5.12) multiplied by $\vec{e}_{i,j}^{(h1c)}$ and integrated over the empty guide section:

$$\int_{S_1} \vec{E}_T^{(1)}.\vec{e}_{i,j}^{(h1c)} w(\rho,\theta)dS = \int_{S_2} \vec{E}_T^{(2)}.\vec{e}_{i,j}^{(h1c)} w(\rho,\theta)dS + \int_{S_3} \vec{E}_T^{(3)}.\vec{e}_{i,j}^{(h1c)} w(\rho,\theta)dS$$

By including the property of the orthonormal eigenfunctions in the LHS of the equation, it is possible to write:

$$\begin{aligned}
T_{i,j}^{(h1c)}&\left(C_{i,j}^{(1c)} + D_{i,j}^{(1c)}\right) = \\
&\frac{1}{\omega\epsilon_2}\sum_{n=1}^{\infty}\sum_{m=1}^{\infty}\beta_{n,m}^{(e2)}T_{n,m}^{(e2)}\left(A_{n,m}^{(2)} + B_{n,m}^{(2)}\right)\int_{\gamma}^{\pi-\gamma}\int_0^b \vec{e}_{n,m}^{(e2)}.\vec{e}_{i,j}^{(h1c)}\rho d\rho d\theta \\
&\qquad + \sum_{p=0}^{\infty}\sum_{q=1}^{\infty}T_{p,q}^{(h2)}\left(C_{p,q}^{(2)} + D_{p,q}^{(2)}\right)\int_{\gamma}^{\pi-\gamma}\int_0^b \vec{e}_{p,q}^{(h2)}.\vec{e}_{i,j}^{(h1c)}\rho d\rho d\theta \\
&+\frac{1}{\omega\epsilon_3}\sum_{n=1}^{\infty}\sum_{m=1}^{\infty}\beta_{n,m}^{(e3)}T_{n,m}^{(e3)}\left(A_{n,m}^{(3)} + B_{n,m}^{(3)}\right)\int_{\pi+\gamma}^{2\pi-\gamma}\int_0^b \vec{e}_{n,m}^{(e3)}.\vec{e}_{i,j}^{(h1c)}\rho d\rho d\theta \\
&\qquad + \sum_{p=0}^{\infty}\sum_{q=1}^{\infty}T_{p,q}^{(h3)}\left(C_{p,q}^{(3)} + D_{p,q}^{(3)}\right)\int_{\pi+\gamma}^{2\pi-\gamma}\int_0^b \vec{e}_{p,q}^{(h3)}.\vec{e}_{i,j}^{(h1c)}\rho d\rho d\theta
\end{aligned}$$

The equation can be written also in terms of matrices:

$$\begin{aligned} C^{(1c)} + D^{(1c)} &= LH^{(h1c)}\left(A^{(2)} + B^{(2)}\right) + LH^{(h2c)}\left(C^{(2)} + D^{(2)}\right) \\ & \quad LH^{(h3c)}\left(A^{(3)} + B^{(3)}\right) + LH^{(h4c)}\left(C^{(3)} + D^{(3)}\right) \end{aligned}$$

<u>1st Coupling integral</u>

E.g. $n : 1 \longrightarrow \infty$ and $i : 0 \longrightarrow \infty$

$$\begin{aligned} CI_3^c &= \int_\gamma^{\pi-\gamma} \int_0^b \vec{e}_{n,m}^{(c2)} . \vec{e}_{i,j}^{(h1c)} \rho d\rho d\theta \\ &= \alpha_{n,m}^{(c2)} \alpha_{i,j}^{(h1c)} i \int_\gamma^{\pi-\gamma} \sin(\nu(\theta-\gamma)) \cos(i\theta) d\theta \int_0^b \frac{dJ_\nu(k_{pn,m}^{(c2)}\rho)}{d\rho} J_i(k_{pi,j}^{(h1c)}\rho) d\rho \\ & \quad -\alpha_{n,m}^{(c2)} \alpha_{i,j}^{(h1c)} n \int_\gamma^{\pi-\gamma} \cos(\nu(\theta-\gamma)) \sin(i\theta) d\theta \int_0^b J_\nu(k_{pn,m}^{(c2)}\rho) \frac{dJ_i(k_{pi,j}^{(h1c)}\rho)}{d\rho} d\rho \end{aligned}$$

The θ-integrals are equal to zero if $n - i$ is even. In the $n - i$ odd case, the integral becomes:

$$\begin{aligned} CI_3^c &= \alpha_{n,m}^{(c2)} \alpha_{i,j}^{(h1c)} \frac{2\nu i}{\nu^2 - i^2} \int_0^b \frac{dJ_\nu(k_{pn,m}^{(c2)}\rho)}{d\rho} J_i(k_{pi,j}^{(h1c)}\rho) + J_\nu(k_{pn,m}^{(c2)}\rho) \frac{dJ_i(k_{pi,j}^{(h1c)}\rho)}{d\rho} d\rho \\ &= \alpha_{n,m}^{(c2)} \alpha_{i,j}^{(h1c)} \frac{2\nu i}{\nu^2 - i^2} \int_0^b \frac{d}{d\rho} \left[J_\nu(k_{pn,m}^{(c2)}\rho) J_i(k_{pi,j}^{(h1c)}\rho)\right] d\rho \\ &= \alpha_{n,m}^{(c2)} \alpha_{i,j}^{(h1)} \frac{2\nu i}{\nu^2 - i^2} \left[J_\nu(k_{pn,m}^{(c2)}\rho) J_i(k_{pi,j}^{(h1)}\rho)\right]_0^b = 0 \end{aligned}$$

This means that the coupling integral $CI_3^c = 0$, $\forall\ i, j, n$ and m.

<u>2nd Coupling integral</u>

E.g. ($p : 0 \rightarrow \infty$ and $i : 1 - \infty$)

$$\begin{aligned} CI_4^c &= \int_\gamma^{\pi-\gamma} \int_0^b \vec{e}_{p,q}^{(h2)} . \vec{e}_{i,j}^{(h1c)} \rho d\rho d\theta \\ &= -\alpha_{p,q}^{(h2)} \alpha_{i,j}^{(h1c)} \int_\gamma^{\pi-\gamma} \sin(\nu(\theta-\gamma)) \cos(i\theta) d\theta \int_0^b \frac{i\nu}{\rho^2} J_\nu(k_{pp,q}^{(h2)}\rho) J_i(k_{pi,j}^{(h1c)}\rho) \rho d\rho \\ & \quad +\alpha_{p,q}^{(h2)} \alpha_{i,j}^{(h1c)} \int_\gamma^{\pi-\gamma} \cos(\nu(\theta-\gamma)) \sin(i\theta) d\theta \int_0^b \frac{dJ_\nu(k_{pp,q}^{(h2)}\rho)}{d\rho} \frac{dJ_i(k_{pi,j}^{(h1c)}\rho)}{d\rho} \rho d\rho \end{aligned}$$

It is evident that this integral is zero if $(p-i)$ is even. In the opposite case ($(p-i)$ odd), the integral is written as:

$$\begin{aligned} CI_4^c &= -\alpha_{p,q}^{(h2)}\alpha_{i,j}^{(h1c)}\frac{2i}{p^2-i^2} \\ &\int_0^b \left[\frac{p^2}{\rho^2}J_p(k_{\rho p,q}^{(h2)}\rho)J_i(k_{pi,j}^{(h1c)}\rho)+\frac{dJ_p(k_{\rho p,q}^{(h2)}\rho)}{d\rho}\frac{dJ_i(k_{pi,j}^{(h1c)}\rho)}{d\rho}\right]\rho d\rho \end{aligned}$$

From these results, the matrix coupling equation becomes:

$$C^{(1c)}+D^{(1c)}=LH^{(h2c)}\left(C^{(2)}+D^{(2)}\right)+LH^{(h4c)}\left(C^{(3)}+D^{(3)}\right) \tag{D.5}$$

Appendix E

Full wave expressions in coaxial waveguides

E.1 Coaxial circular waveguide

The eigenfunctions related to the E-field in the coaxial waveguide are similar to those of the empty circular waveguide, equations (C.1) and (C.2). The difference comes from the ρ-function which are:

$$\begin{aligned}
B_n^{(c)}(k^{(c)}_{\rho n,m}\rho) &= N_n(k^{(c)}_{\rho n,m}b)J_n(k^{(c)}_{\rho n,m}\rho) - J_n(k^{(c)}_{\rho n,m}b)N_n(k^{(c)}_{\rho n,m}\rho) \\
B_p^{(h)}(k^{(c)}_{\rho p,q}\rho) &= N'_p(k^{(h)}_{\rho p,q}b)J_p(k^{(h)}_{\rho p,q}\rho) - J'_n(k^{(h)}_{\rho p,q}b)N_p(k^{(h)}_{\rho p,q}\rho)
\end{aligned}$$

The TEM eigenfunction can be written, at z=0, as:

$$\vec{e}^{\,(c)}_{0,0} = \alpha^{(c)}_{0,0}\frac{1}{\rho}\vec{\rho}$$

Again, any modes can be decomposed into the sum of two orthogonal modes: the first type (superscript "s") with the E-field perpendicular to the septum and the second one (superscript "c") with the E-field parallel to the septum.

E.2 Upper sectorial coaxial waveguide

The eigenfunctions related to the E-field in the upper semi-sector waveguide are similar to those of the upper half circular waveguide, equations (C.3) and (C.4). The difference comes from the ρ-function which are, in this case,:

$$\begin{aligned}
B_\nu^{(e)}(k^{(e)}_{\rho n,m}\rho) &= N_\nu(k^{(e)}_{\rho n,m}b)J_\nu(k^{(e)}_{\rho n,m}\rho) - J_\nu(k^{(e)}_{\rho n,m}b)N_\nu(k^{(e)}_{\rho n,m}\rho) \\
B_\nu^{(h)}(k^{(e)}_{\rho p,q}\rho) &= N'_\nu(k^{(h)}_{\rho p,q}b)J_\nu(k^{(h)}_{\rho p,q}\rho) - J'_\nu(k^{(h)}_{\rho p,q}b)N_\nu(k^{(h)}_{\rho p,q}\rho)
\end{aligned}$$

The lower guide field expressions are obtained by replacing all the angular variables by $\nu(\theta - \gamma - \pi)$.

E.3 Normalization coefficients

The α ortho-normalization coefficient is computed by using the integral defined in equation (C.5) over the appropriate waveguide cross-section S, yielding similar expressions as those to the circular waveguide. $B_n^{(e)}(k^{(e)}_{\rho n,m}\rho)$, $B_p^{(h)}(k^{(e)}_{\rho p,q}\rho)$, $B_\nu^{(e)}(k^{(e)}_{\rho n,m}\rho)$ and $B_\nu^{(h)}(k^{(e)}_{\rho p,q}\rho)$ replacing $J_n^{(e)}(k^{(e)}_{\rho n,m}\rho)$, $J_p^{(h)}(k^{(e)}_{\rho p,q}\rho)$, $J_\nu^{(e)}(k^{(e)}_{\rho n,m}\rho)$ and $J_\nu^{(h)}(k^{(e)}_{\rho p,q}\rho)$, respectively in the expression of the ortho-normalization coefficients is the only difference between the TE and TM modes. For the TEM mode, equation (C.5) leads to:

$$\alpha^{(e)}_{0,0} = \frac{1}{\sqrt{\pi}k^{(e)}_{\rho 0,0}bJ_1(k^{(e)}_{\rho 0,0}b)}$$

The expression for the 1 Watt-normalization coefficient does not change when considering a circular waveguide or a coaxial waveguide. Therefore, they can be found by equations (C.6) and (C.7).

Appendix F

Mathematical formulae

F.1 Bessel's equation

The Bessel functions are solutions of the Bessel differential equation:

$$x^2y'' + xy' + (x^2 - \nu^2)y = 0$$

if $B_n(x) = AJ_n(x) + BN_n(x)$, with J_n: Bessel function of the first kind, and N_n: Bessel function of the second kind, if n integer and ν real, then [37]:

$$\begin{aligned}
B_0'(x) &= -B_1(x) \\
B_{-n}(x) &= (-1)^n B_n(x) \\
\nu B_\nu(x) &= \frac{x}{2}\left[B_{\nu-1}(x) + B_{\nu+1}(x)\right] \\
\frac{dB_\nu(\alpha x)}{dx} &= \frac{\alpha}{2}(B_{\nu-1}(\alpha x) - B_{\nu+1}(\alpha x)) \\
\frac{d}{dx}B_0(\alpha x) &= -\alpha B_1(\alpha x) \\
x\frac{dB_\nu(\alpha x)}{dx} &= \alpha x B_{\nu-1}(\alpha x) - \nu B_\nu(\alpha x) \\
x\frac{dB_\nu(\alpha x)}{dx} &= \nu B_\nu(\alpha x) - \alpha x B_{\nu+1}(\alpha x) \\
\frac{d}{dx}(x^\nu B_\nu(x)) &= x^\nu B_{\nu-1}(x) \\
\frac{d}{dx}(x^{-\nu} B_\nu(x)) &= -x^{-\nu} B_{\nu+1}(x)
\end{aligned}$$

Integrals involving Bessel's function:

$$\begin{aligned}
\int x^2 B_0(x)dx &= x^2 B_1(x) + xB_0(x) - \int B_0(x)dx \\
\int B_1(x)dx &= -B_0(x) \\
\int xB_1(x)dx &= -xB_0(x) + \int B_0(x)dx \\
\int x^\nu B_{\nu-1}(x)dx &= x^\nu B_\nu(x) \\
\int xB_\nu(\alpha x)B_\nu(\beta x)dx &\dot{=} x\left(\frac{\alpha B_\nu(\beta x)B'_\nu(\alpha x) - \beta B_\nu(\alpha x)B'_\nu(\beta x)}{\beta^2 - \alpha^2}\right) \\
&= x\left(\frac{\beta B_\nu(\alpha x)B_{\nu-1}(\beta x) - \alpha B_{\nu-1}(\alpha x)B_\nu(\beta x)}{\alpha^2 - \beta^2}\right) \\
&= x\left(\frac{\beta B_\nu(\alpha x)B_{\nu+1}(\beta x) - \alpha B_{\nu+1}(\alpha x)B_\nu(\beta x)}{\beta^2 - \alpha^2}\right) \\
\int xB_\nu^2(\alpha x)dx &= \frac{x^2}{2}(B'_\nu(\alpha x))^2 + \frac{x^2}{2}(1 - \frac{\nu^2}{\alpha^2 x^2})B_\nu^2(\alpha x) \\
&= \frac{x^2}{2}\left(B_\nu^2(\alpha x) - B_{\nu-1}(\alpha x)B_{\nu+1}(\alpha x)\right)
\end{aligned}$$

Furthermore, the following relation exists:

$$\int xB_\nu^{(1)}(\alpha x)B_\nu^{(2)}(\beta x)dx = \frac{x(\alpha B_{\nu+1}^{(1)}(\alpha x)B_\nu^{(2)}(\beta x) - \beta B_\nu^{(1)}(\alpha x)B_{\nu+1}^{(2)}(\beta x)}{\alpha^2 - \beta^2}$$

F.2 Sine integrals

They correspond to the coupling integrals in θ:

1. $n - i$ odd

$$\begin{aligned}
\int_\gamma^{\pi-\gamma} \sin(\nu(\theta - \gamma))\sin(i\theta)d\theta &= 0 \\
\int_\gamma^{\pi-\gamma} \cos(\nu(\theta - \gamma))\cos(i\theta)d\theta &= 0 \\
\int_\gamma^{\pi-\gamma} \sin(\nu(\theta - \gamma))\cos(i\theta)d\theta &= \frac{2\nu\cos(i\gamma)}{\nu^2 - i^2} \\
\int_\gamma^{\pi-\gamma} \cos(\nu(\theta - \gamma))\sin(i\theta)d\theta &= -\frac{2i\cos(i\gamma)}{\nu^2 - i^2}
\end{aligned}$$

2. $n - i$ even

$$\begin{aligned}
\int_{\gamma}^{\pi-\gamma} \sin(\nu(\theta-\gamma))\sin(i\theta)d\theta &= \frac{2\nu\sin(i\gamma)}{\nu^2 - i^2} \\
\int_{\gamma}^{\pi-\gamma} \cos(\nu(\theta-\gamma))\cos(i\theta)d\theta &= \frac{2i\sin(i\gamma)}{\nu^2 - i^2} \\
\int_{\gamma}^{\pi-\gamma} \sin(\nu(\theta-\gamma))\cos(i\theta)d\theta &= 0 \\
\int_{\gamma}^{\pi-\gamma} \cos(\nu(\theta-\gamma))\sin(i\theta)d\theta &= 0
\end{aligned}$$

Bibliography

[1] V. F. Viley, '*Modern Microwave Technology*', Prentice-Hall, Englewood Cliffs, New Jersey, 1987, pp. 369-371.

[2] S. Ramo, J. R. Whinnery and T. Van Duzer, '*Fields and Waves in Communication Electronics*', Wiley, New York, 1965, Chap. 4.

[3] R. F. Harrington, '*Matrix Methods for Field Problems*', Proc. IEEE, vol. 55, Feb. 1967, pp. 136-149.

[4] W. J. R. Hoefer, '*Transmission-Line Matrix Method - Theory and Applications*', Proc. IEEE, MTT-33, Oct. 1985, pp. 882-893.

[5] U. Schulz and R. Pregla, '*A New Technique for the Analysis of the Dispersion Characteristics of Planar Waveguides*', Arch. Elek. Ubertragung., vol. 34, Apr. 1980, pp. 169-173.

[6] P. Bhartia and I. Bahl, '*Millimeter Wave Engineering and Applications*', Wiley, New York, 1984, pp. 1-8 .

[7] I. Bahl and P. Bhartia, '*Microwave Solid State Circuit Design*', Wiley, New York,1988, pp. 294-299 .

[8] R. G. Egri, A. E. Williams and A. E. Atia, '*A Contiguous-Band Multiplexer Design*', IEEE MTT-S Int. Symp. Digest, 1983. pp. 86-88.

[9] A. Wexler, '*Solution of Waveguide Discontinuities by Modal Analysis*', IEEE Trans., MTT-15, September 1967, pp. 508-517.

[10] M. H. Chen, '*A 12-Channel Contiguous Band Multiplexer at Ku-Band*', IEEE MTT-S Int. Symp. Digest, 1983, pp. 77-79.

[11] L. D. Cohen, N. Worontzoff, J. Levy and A. Harvey, '*Millimeter Wave Multiplexer with Printed Circuit Elements for the 88 to 100 GHz Frequency Range*', IEEE MTT-S Int. Symp. Digest, 1984, pp. 233-235.

[12] S. C. Holme, '*A 12 GHz 12 Channels Contiguous Multiplexer for Satellite Applications*', IEEE MTT-S Int. Symp. Digest, 1984, pp. 295-296.

[13] R. Tong and D. Smith, '*A 12 Channels Contiguous Band Multiplexer for Satellite Application*', IEEE MTT-S Int. Symp. Digest, 1984, pp. 297-298.

[14] W. C. Tang, S. Sferrazza, B. Beggs and D. Siu, '*Dielectric Resonator Output Multiplexer for C-Band Satellite Applications*', IEEE MTT-S Int. Symp. Digest, 1985, pp. 343-345.

[15] M. I. Skolnik, '*Introduction to Radar Systems*', McGraw-Hill, New York, 1980, pp. 359-366.

[16] J. E. Reed, '*The AN/FPS-85 Radar System*', Proceeding of the IEEE, vol. 57, March 1969, pp. 324-335.

[17] J. E. Brookner, '*Aspects of Modern Radar*', Artech House, Boston, 1988, pp. 29-33.

[18] J. Dittloff, J. Bornemann and F. Arndt, '*Computer Aided Design of Optimum E- or H-Plane N-Furcated Waveguide Power Divider*', Proceedings of the 17th European Microwave Conference, 1987, pp. 181-186.

[19] J. Dittloff and F. Arndt, '*Rigorous Design of Septate E-plane Multiplexers with Printed Circuit Element*', IEEE MTT-S Int. Symp. Digest,1988, pp. 431-434.

[20] L. Lewin, '*Theory of Waveguide*', Butterworth, London 1975, pp. 4-6.

[21] T. Itoh, '*Numerical Techniques for Microwave and Millimeter Wave Passives Structures*', Wiley, New York, 1989,

[22] R. Vahldieck, J. Bornemann, F. Arndt and D. Grauerholz, '*Optimized Waveguide E-Plane Metal Insert Filters for Millimeter Wave Applications*', IEEE Trans., MTT-31, Jan. 1983, pp. 65-69.

[23] A. S. Omar and K. Schunemann, '*Transmission Matrix Representation of Finline Discontinuity*', IEEE Trans., MTT-33, Sep. 1985.

[24] I.Wolff, G. Kompa and R. Mehran, '*Calculation Method for Microstrip Discontinuities and T-Junctions*', Electron. Lett., vol. 8, April 1972, pp. 177-179.

[25] R. Mehran, '*Computer-Aided design of microstrip filters considering dispersion, loss, and discontinuity effect*', IEEE Trans., MTT-27, March 1979, pp. 239-245.

[26] R. Vahldieck and W. Hoefer, '*Finline and Metal Insert Filters with Improved Passband Separation and Increased Stopband Attenuation*', IEEE Trans., MTT-33, Dec. 1985.

[27] R. Vahldieck, '*Accurate Hybrid-Mode Analysis of Various Finline Configurations Including Multilayered Dielectrics, Finite Metallization Thickness and Substrate Holding Grooves*', IEEE Trans., MTT-32, pp. 1454-1460, Nov. 1984.

[28] J. Bornemann and R. Vahldieck, '*Characterization of a Class of Waveguide Discontinuities Using a Modified TE^x_{mn} Mode Approach*', IEEE Trans., MTT-38, Dec. 1990, pp. 1816-1822.

[29] U. Tucholke, '*Feldtheoretishe Analyse und Rechnergestuetzter Entwurf von Resonanzblendenfiltern und Rillenpolarisatoren in Rechteckhohlleitern*', Fortschritt-Berichte VDI, Reihe 21, N. 25, Düsseldorf, 1988, pp. 45-46.

[30] F. Arndt, J. Bornemann, R. Vahldieck and D. Grauerholz, '*E-Plane Integrated Circuit Filters with Improved Stopband Attenuation*', IEEE Trans., MTT-32, Oct. 1984, pp. 1391-1394.

[31] R. Mittra and S. W. Lee, '*Analytical Techniques in the Theory of Guided Waves*', MacMillan, New York, 1971, pp. 207-217.

[32] R. Mittra and J. Pace, '*A New Technique for Solving a Class of Boundary Value Problems*', Rep.72, Antenna Laboratory, University of Illinois, Urbana, 1963.

[33] H. Patzelt and F. Arndt, '*Double-Plane Steps in Rectangular Waveguides and their Application for Transformers, Irises and Filters*', IEEE Trans., MTT-30, May 1982, pp. 771-776.

[34] F. Arndt and G. U. Paul, '*The Reflection Definition of the Characteristic Impedance of Microstrips*', IEEE Trans., MTT-27, Aug. 1979, pp. 724-730.

[35] N. Marcuvitz,'*Waveguide Handbook*', McGraw-Hill, New York, 1951, p. 73.

[36] P. H. Masterman and P. J. B. Clarricoats,'*Computer Field-Matching Solution of Waveguide Transverse Discontinuities*', IEE, vol. 118, Jan. 1971, pp. 51-63.

[37] G. Petiau,'*La Théorie des Fonctions de Bessel*', CNRS, Paris 1955, pp. 185-214.

[38] G. Matthaei, L. Young and E.M.T. Jones, '*Microwave Filters, Impedance-Matching Network and Coupling Structures*', McGraw-Hill, New York 1964, pp. 365-373.

[39] I. Sreenivasiah and D.C. Chang,'*A Variational Expression for the Scattering Matrix of a Double-Step Discontinuity in a Coaxial Line and its Application to a TEM Cell*', IEEE Trans., MTT-29, pp. 40-47,Jan. 1981.

[40] G.B. Gajda and S.S. Stuchly, '*Numerical Analysis of Open-Ended Coaxial Lines*', IEEE Trans., MTT-31, pp. 380-384, May 1983.

[41] J. R. Whinnery and H. W. Jamieson, '*Equivalent Circuits for Discontinuities in Transmission Lines*', IRE, vol. 32, Feb. 1944, pp. 98-114.

[42] J. R. Whinnery, H. W. Jamieson and T. E. Robbins, '*Coaxial-Line Discontinuities*', IRE, vol. 32, Nov. 1944, pp. 695-709.

[43] W.K. Gwarek, '*Analysis of Arbitrarily-Shaped Coaxial Discontinuities*', Proceeding 17^{th} European Microwave Conf., 1987.

[44] W.K. Gwarek, '*Computer-Aided Analysis of Arbitrarily Shaped Coaxial Discontinuities*', IEEE Trans., MTT-36, Feb. 1988, pp. 337-342.

[45] P. I. Somlo, '*The Computation of Coaxial Line Step Capacitance*', IEEE Trans., MTT-15, pp. 48-53, Jan. 1967.

[46] D. Wood, '*Shielded-Open-Circuit Discontinuity Capacitance of a Coaxial Line*', Proc. Inst. Elec. Eng., vol. 119, Dec. 1972, pp. 1691-1692.

[47] R. Levy and T.E. Rozzi, '*Precise Design of Coaxial Low-Pass Filters*', IEEE Trans., MTT-16, March 1968, pp. 142-147.

[48] G.R. Haack, '*Optimal Design of Coaxial Low-Pass Filters*', IEEE Trans., MTT-17, March 1969, pp. 169-170.

[49] M. Razaz and J. B. Davies, '*Capacitance of the Abrupt Transition from Coaxial-to-Circular Waveguide*', IEEE Trans., MTT-27, Feb. 1979, pp. 564-569.

[50] R. A. Waldron, '*Theory of Guided Electromagnetic Waves*', VNR, London,1969, pp. 227-238.

[51] G. L. James, '*Analysis and Design of TE_{11}-to-HE_{11} Corrugated Cylindrical Waveguide Mode Converters Capacitance*', IEEE Trans., MTT-29, Oct. 1981, pp. 1059-1066.

[52] E. W. Risley, '*Discontinuity Capacitance of a Coaxial Line Terminated in a Circular Waveguide*', IEEE Trans., MTT-17, Feb. 1969, pp. 86-92.

[53] K. Hashimoto, '*Circular TE_{0n} Mode Filters for Guided Millimeter-Wave Transmission*', IEEE Trans., MTT-24, Jan. 1976, pp. 25-31.

[54] T. Sugiura and H. Suga, '*The Susceptance of an Annular Metallic Strip in a Circular Waveguide with Incident TE_{01} Mode*', IEEE Trans., MTT-27, Feb. 1979, pp. 160-167.

[55] S. A. Kheifets, '*Electromagnetic Fields in an Axial Symmetric Waveguide with Variable Cross Section*', IEEE Trans., MTT-29, Mar. 1981, pp. 222-229.

[56] F. L. Ng and R. H. T. Bates, '*Null-Field Method for Waveguide of Arbitrary Cross Section*', IEEE Trans., MTT-20, Oct. 1972, pp. 658-662.

[57] L. Q. Bui, D. Ball and T. Itoh, '*Broadband Millimeter-Wave E-plane Bandpass Filters*', IEEE MTT-S Int. Symp. Digest, 1984, pp. 236-240.

[58] A. E. Atia and A. E. Williams, '*General TE_{011}-Mode Waveguide Bandpass Filters*', IEEE Trans., MTT-24, Oct. 1976, pp. 640-648.

[59] W. C. Tang and S. K. Chaudhuri, '*A True Elliptic-Function Filter Using Triple-Mode Degenerate Cavities*', IEEE Trans., MTT-32, Nov. 1984, pp. 1449-1454.

[60] U. Rosenberg and D. Wolk, '*Filter Design Using In-Line Triple-Mode Cavities and Novel Iris Couplings*', IEEE Trans., MTT-37, Dec. 1989, pp. 2011-2019.

[61] D. A. Pierre, '*Optimization Theory with Applications*', Wiley & Sons, New York, 1969, pp. 292-296.